System identification for robust inferential control applied to a prototype motion system

Grassens, Erik

Award date:
2010

System Identification for Robust Inferential Control Applied to a Prototype Motion System

Erik Grassens

CST 2010.013

Master's Thesis

Committee: prof. ir. O.H. Bosgra (Graduate professor)
prof. dr. ir. M. Steinbuch
dr. ir. M.F. Heertjes (D&C)
dr. ir. M.M.J. van de Wal (ASML)
ir. T.A.E. Oomen (Supervisor)
ir. R.M.A. van Herpen

Eindhoven University of Technology
Department of Mechanical Engineering
Control Systems Technology Group

Eindhoven, April 2010

Abstract

The current trend in the design of high-precision positioning systems is towards lightweight structures, which are capable of faster accelerations. Flexible dynamics play a prominent role in the behavior of such systems, resulting in the fact that performance variables cannot be measured. The aim of this research is to explicitly deal with flexible dynamical behavior in control design. The key idea is to infer the performance variables from measured variables by means of a model. System identification and model validation methods for the new control strategy are developed and applied to a prototype lightweight motion system. An accurate model of the system dynamics is obtained and used to improve the performance on the prototype setup beyond the limitations imposed by standard control techniques, thereby giving a proof of concept of this new control theory for lightweight motion systems with flexible dynamics.

Contents

Chapter 1

Introduction

1.1 Background

Improved speed and accuracy are two demanding aspects that are required for high-precision positioning systems, and advanced motion control techniques play a crucial role in achieving these performance requirements. Amongst these techniques, is the field of optimal control, which aims on optimizing the performance of positioning systems, by adjusting feedback and feed-forward control. Other research fields are, for instance learning control, which is especially suitable for repetitive tasks, and adaptive control, focusing on systems that work under changing conditions. These advanced control techniques are often model based, and rely on accurate modeling of the underlying dynamics. Therefore, research focuses on system identification, which is a fast, reliable, and often inexpensive way to obtain accurate models.

Another important aspect influencing the achievable performance of high-precision positioning systems, is the design of the structure. In order to be able to achieve high accelerations, the current developments are towards lightweight systems. One of the common consequences of this trend, is that the stiffness is reduced, and flexible dynamics are more prominent in the system behavior. This complicates the design of motion controllers, and rises the question how to control lightweight systems with flexible dynamics.

An example of a high-performance motion system is a wafer scanner, which is a machine involved in the production of integrated circuits, that are used in various components of computers and other electronic devices. These integrated circuits consist of chips of silicon, in which patterns are etched in a photolithographic process.

In the photolithographic process a silicon wafer is coated with a photoresistant material, then the desired pattern is projected on the wafer through a reduction lens. The photoresistant material is washed away depending on the amount of exposure, thus forming the pattern, and the silicon is etched away using acids.

Typically, the positioning of the wafer during this process, requires nano-scale precision, and due to the costs of these machines, a high throughput is desired. In other words, a wafer scanner is one of the most demanding high-precision positioning systems that is commercially available. The current generation of wafer scanners is not yet lightweight, and further study on the control of flexible dynamics is desired to make this possible.

1.2 Motivation

The demand for faster production, requires high-performance motion systems that are capable of high accelerations. This leads to a trend in the designs of these machines, in which the weight of the moving part is reduced. By virtue of Newton's second law, $F = ma$, reducing

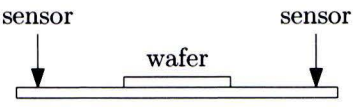

Figure 1.1: Schematic two-dimensional sketch of a wafer scanner.

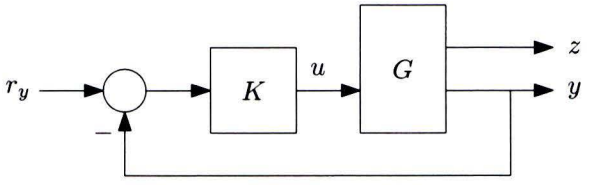

Figure 1.2: Control scheme with a flexible structure G which has input u, collocated output y and noncollocated output z.

mass leads to higher accelerations, when the same force is applied. Often, the consequences is that the stiffness of the structure also is lowered.

Depending on the design, lightweight systems often have a very low stiffness, such that the first eigenfrequency $\omega = \sqrt{k/m}$ is relatively low, compared to conventional designs. If the first eigenfrequency is in the bandwidth of the controller, this can lead to severe performance degradation. One of the problems occurs, when position measurement at the desired performance location is not possible. In wafer scanners, for example, accurate positioning of the wafer is desired. However, it is not possible to measure the position of the wafer during normal operation, because this would interfere with the production process. Therefore, the position is measured at different locations, as is sketched in Figure 1.1. When the motion of the system is dominated by rigid body dynamics this does not impose any problems, since the position of the wafer is fixed relative to the sensors. However, when flexible dynamics play a significant role, this is no longer the case. Then, it is possible that good performance is obtained at the sensor location, while there is severe performance degradation in the area where the wafer is located. This can be explained as follows.

Consider a flexible structure $G = \begin{bmatrix} G_z & G_y \end{bmatrix}^T$, with input u, collocated measurement output y and noncollocated performance output z, on which feedback control is applied by controller K, such that reference signal r_y is tracked, as is shown in Figure 1.2.

It can be easily shown that if $|G_y K| \gg 1$, then the closed-loop transfer function from r_y to y, given by $T_y = \frac{G_y K}{1+G_y K}$, is close to one, which is desirable because it assures good tracking. However, the transfer function from r_y to z, given by $T_z = \frac{G_z K}{1+G_y K}$, then becomes approximately $\frac{G_z}{G_y}$, which causes vibrations in the structure when the system is excited at frequencies where $|G_z| \gg |G_y|$, i.e., there is good tracking in y, and poor tracking in z.

As an example the flexible structure in Figure 1.3, consisting of two identical masses m connected by a spring k and a damper d, is considered. A force u can be applied to the first mass, and the displacement of the two masses are y and z. Feedback control is applied to output y, such that the flexible dynamics are in the bandwidth of the controller.

A simulated closed-loop step response of the controlled flexible structure, is shown in Figure 1.4. This figure shows a good response of the first mass y (green $-$), which is the point where the system is actuated and measured for feedback-control. The second mass z (blue $-$) shows large vibrations, caused by flexibility in the structure. For a rigid structure, the response of y and z would have been identical, and this problem would not occur. This shows that it is essential to take the flexibility of a structure in account in controller design, and that it can severely influence the achievable performance. Consequently, this motivates

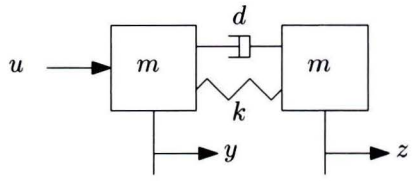

Figure 1.3: Flexible structure, consisting of two identical masses m connected by a spring k and a damper d.

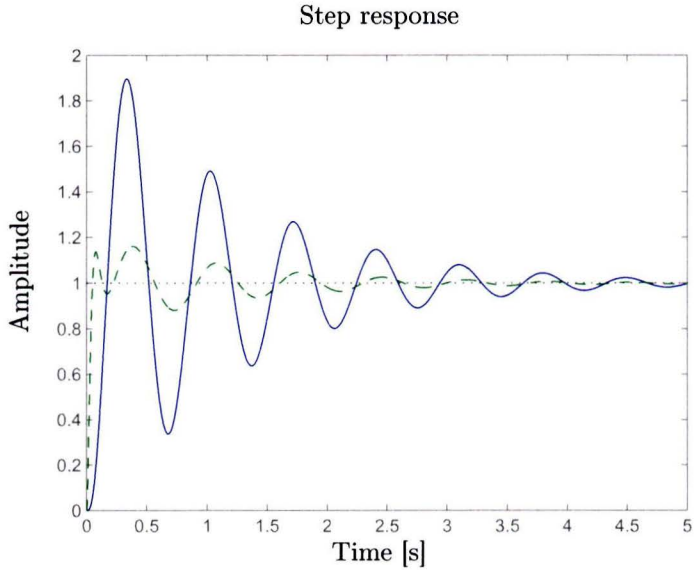

Figure 1.4: closed-loop step response, showing the vibrations caused by flexible dynamics in the bandwidth of the controller, for a two-mass-spring-damper system, with performance output z (blue $-$) and measured output y (green $--$).

the importance of accurate modeling of the relevant dynamics, needed for controller design for flexible systems.

1.3 Literature

Structures with flexible dynamics have been studied in literature extensively, especially for structures with a relatively simple geometry such as mass-spring-damper systems, beams and plates, see e.g. [30, 31]. For more complex structures, often finite element analysis methods are used, see e.g. [6].

Feedback control of structures with flexible dynamics has mainly focused on attenuation of vibrations in the structure [1, 2], and on enhancing the performance of the measured output [13]. However, in the case that the performance output cannot be measured for feedback control, theoretical limitations on the achievable performance apply [12, 22, 24]. The remaining question is: how can control be used to overcome the limitations imposed by flexible dynamics?

An initial approach towards the answer of this question is found in inferential control, which infers the performance variable from measured plant output. Many successful appli-

cations of inferential control are reported in process control, see e.g., [28, 39, 45, 47], but application to structures with flexible dynamics is not common.

Inferential control relies on accurate modeling of the system dynamics. A fast and reliable method of obtaining such models, is by means of system identification. Since the quality of a model depends on its intended use, identification of the plant dynamics are related to the control objective, see [5, 15, 34, 44]. It is essential that uncertainty and errors in the model are addressed appropriately, see [32, 33], such that robust controller designs can be obtained. The identification and validation methods in the literature assume that the performance variables are measured, and thus can not be applied directly to the inferential control structure without modifications. Furthermore, it is not straightforward to cast the inferential control problem in the generalized plant framework, which is commonly used in optimal robust control [10, 45].

The literature does not answer the question how control can deal with structures with flexible dynamics, when the performance variables are not measured, and how to obtain control-relevant models for these structures by means of system identification. In Section 1.4, is discussed how this problem is approached in this thesis.

1.4 Approach

In Section 1.2, a motivation was given for studying control of flexible structures. It was shown that flexible dynamics in the controller bandwidth, can have severe consequences for the achieved performance, when performance is desired at a location where no sensors are present. Although in the literature control of structures with flexible dynamics has been studied, the question whether it can deal with performance variables that are not measured, is still open. In order to determine whether control is able to deal with this problem and how it can be done, an experimental setup is available. This setup consists of a flexible metal beam, which represents a prototype next-generation lightweight wafer scanner. It will be used to study whether flexible dynamics are feasible in high-precision motion systems. The research question in this thesis is:

> *What is the influence of flexible dynamics in next-generation lightweight positioning systems, when the measured variables are not the performance variables, and how can motion control be used to deal with flexible dynamics?*

This question will be divided into several subquestions, that will be answered in this thesis. The first subquestion follows directly from the first half of the research question:

1. *What is the influence of flexible dynamics in lightweight positioning systems, when the measured variables are not the performance variables?*

Standard $\mathcal{H}_\infty$-optimal control is applied to a representative test case and it is shown that the standard problem, does not result in a solution with a satisfying level of performance. Therefore, another control configuration may be desirable, which leads to the following question:

2. *Which control configuration is suitable for systems with flexible dynamics, when the measured variables are not the performance variables?*

To answer this question, the possibilities of inferential control for flexible systems are investigated. Inferential control is a technique of which certain implementations are common in chemical process control, applied when a performance output is not available for feedback.

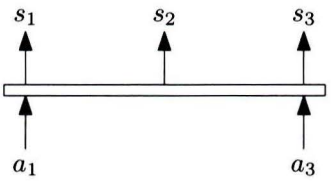

Figure 1.5: Representative scenario for control of high-precision positioning systems with flexible dynamics, with input $u = a_1 = a_3$, measured output $y = \frac{s_1+s_3}{2}$ and performance variable $z = s_2$.

This concept is cast in an $\mathcal{H}_\infty$-framework, such that performance and robustness can be assessed quantitatively.

For model based control techniques, such as $\mathcal{H}_\infty$-optimal control, it is essential that the relevant dynamics are modeled accurately. The third question therefore is:

3. *How can an accurate model of a system with flexible dynamics be obtained, that contains the dynamics that are relevant for controller design?*

System identification is a fast and reliable way to obtain an accurate model of a system. Therefore, a control-relevant system identification procedure will be studied, and applied to the inferential control configuration.

Every model inevitably contains deviations from the real system, and therefore the next subquestion concerns the validity of the obtained model. Because modeling errors are closely related to robustness, the question is stated as follows:

4. *How can modeling errors be addressed, such that robustness of the subsequent controller design can be achieved?*

To answer this question, a model validation procedure for robust control is investigated, in which the modeling errors are addressed appropriately. The model validation procedure is then applied to the inferential control configuration.

In the last subquestion, all aspects are combined in the implementation on the experimental setup, such that the achievements of the new control configuration can be evaluated:

5. *Design and implement robust optimal inferential controllers on the experimental setup, and evaluate the achieved performance.*

A proof of concept is desired before further development of lightweight wafer stages will be done. Therefore, this project focuses on the flexible beam experimental setup, which acts as a prototype for future lightweight wafer stages. The situation sketched in Figure 1.5 will be used as a representative scenario, with input $u = a_1 = a_3$ and measured output $y = \frac{s_1+s_3}{2}$. The performance z is desired in the center of the beam, i.e., $z = s_2$. This situation is closely related to the intended application that was sketched in Figure 1.1. The achieved performance on the setup, gives a good indication of the possibilities for motion control of next-generation wafer stages.

1.5 Outline

This report is organized as follows.

In Chapter 2, some relevant aspects of the flexible beam are discussed. First the details of the experimental setup will be treated, followed by frequency domain identification of the

setup. Nonparametric models will be identified, for later use in the model identification and validation procedures. Furthermore, an analytical model of the flexible beam, based on first principles, will be compared to the nonparametric model, to gain insight in the dynamics of the system.

In Chapter 3, $\mathcal{H}_\infty$-optimal inferential control is discussed. First the concept of internal stability is treated, followed by controller synthesis for optimal performance. Then, it is explained how model uncertainty is included in the $\mathcal{H}_\infty$-framework, such that robust controllers can be designed. Furthermore, the inferential control structure for flexible systems is introduced, and cast in a form that suits the $\mathcal{H}_\infty$-framework. In simulations it is compared with standard control.

In Chapter 4, control-relevant identification for the inferential control structure is treated. A criterion for control-relevance is shown, and a method to minimize the criterion is discussed. Then, an identification experiment is performed on the experimental setup, design aspects such as weighting filter design are discussed, and the results are presented.

In Chapter 5, optimal performance controllers are synthesized for the standard and inferential control structures. These controllers are compared to each other, and a factor 4.2 improvement in performance is shown for the inferential controller. Finally, the controllers are implemented on the experimental setup, and the results are validated.

Chapter 6 covers the model validation procedure. The influence of disturbances in measurement data and systematic errors in the identified model are addressed appropriately. The validity of the model is evaluated with experiments, and the results are presented and discussed.

In Chapter 7, robust performance synthesis for the standard and inferential control structures is performed, and the worst-case performance of the inferential control configuration is shown to be 4.6 times higher than for standard robust control. The synthesized controllers are implemented on the flexible beam setup, and the experiments validate the results.

In Chapter 8, the conclusions and recommendations are presented, in A controller synthesis is discussed, and in B is explained how model sets can be graphically represented in Bode diagrams.

Chapter 2

Modeling of the flexible beam experimental setup

As was motivated in the introduction, flexible dynamics in lightweight wafer stages can cause severe performance problems, when the sensors are not located at the points where performance is needed. Currently, no lightweight wafer stages are available, because it is not clear whether control can deal with flexible dynamics. Wafer stages are complex three-dimensional structures with six motion degrees of freedom, and a controller design procedure, that can deal with flexible dynamics, as well as the complex structure of the system, is desired.

In order to investigate control of flexible structures, a prototype lightweight positioning system is available for experiments. The setup consists of a flexible beam with three actuators and an equal amount of sensors, and can be used to study the representative scenario in Figure 1.5. The flexible beam can be analyzed in a two-dimensional plane, such that is has two motion degrees of freedom, i.e., translation and rotation, and has the flexible dynamics that will be characteristic for lightweight wafer stages.

This chapter is an introduction to the flexible beam experimental setup, which is used throughout this thesis to confirm the theory with experiments. The purpose of this chapter is to get familiar with the experimental setup and the dynamics of this prototype lightweight positioning system, and none of the research questions in Section 1.4 are answered yet.

First, a short description of the setup and its properties is given in Section 2.1. Then, in Section 2.2, an initial indication of the dynamics of the beam is obtained by means of an identification experiment. The experiment is arranged such that an unbiased frequency response of the setup is obtained. This gives a first indication of the locations of resonances and anti-resonances, and can be used for initial controller design. In Section 2.3, the flexible beam setup is modeled as an Euler-Bernoulli beam, which has been studied in literature extensively [30, 31, 43]. The fact that modeling of such systems is well-known, is a great advantage in understanding the underlying physical relations of the flexible dynamics. Furthermore, finite element models are available in literature, see e.g. [6], which can be used for accurately simulating the system behavior and controller synthesis. Finally, in Section 2.4 the conclusions of this chapter are presented.

2.1 Description of the experimental setup

The experimental setup consists of a flexible steel beam with dimensions 500 mm $\times$ 20 mm $\times$ 2 mm. Four degrees of freedom are fixed with leaf springs, such that only one free translation

and rotation remain, as is shown in Figure 2.1. Figure 2.1a shows a photo of the setup, and Figure 2.1b shows a schematic sketch, on which the actuator and sensor locations a_i and s_i are indicated, as well as the remaining degrees of freedom (red).

Hard real-time data acquisition is implemented using a PowerDAQ control board, and Linux RTAI with Matlab Simulink as rapid control prototyping system, see [25]. The beam is actuated by three current-driven voice-coil actuators, and the position is measured with three contactless fiber-optic displacement sensors, with a resolution in the order of magnitude of 0.25 μm, using a sampling frequency of 1000 Hz. This means there is one sensor and actuator pair more, than needed for full controllability of the rigid body motion degrees of freedom of the system. In the scenario sketched in the introduction, see Figure 1.5, the second sensor and actuator pair will not be used during normal operation of the plant. Furthermore, in this thesis only the translation of the beam is considered, such that the system can be considered being a SISO system, and there is no need to deal with the additional complexity of MIMO control. The input will be applied to the first and third actuator, i.e. $u = a_1 = a_3$, and $y = \frac{s_1+s_3}{2}$ will be measured for feedback. However, during identification of the system, performance output $z = s_2$ will be measured, such that a model that contains the relevant flexible dynamics can be obtained.

In the work of Hendriks [19], the following relevant characteristics of the setup have been determined by experiments:

- The system is dominated by linear dynamics, although some small nonlinearities occur.
- The signal to noise ratio of the plant output is around 50 dB.
- The effects of aliasing are small for the used sampling frequency.

These good properties make reliable system identification possible, and allow using linear control theory.

2.2 Frequency response function identification

nonparametric models can be obtained from data, and when identification is carried out properly, an accurate first indication of the dynamics of a system is obtained. In the approach used in this thesis, a deterministic periodic input signal is used to obtain identification data of the experimental setup. This has certain advantages over random excitation of the system, as shown in literature [27, 40, 3, 18]. Furthermore, this plays an important role in the identification and validation procedures in Chapters 4 and 6. The most important properties are discussed in this section.

2.2.1 Signal leakage

Since signal analysis is carried out numerically, the analyzed signals, as well as their spectra, need to have finite length and resolution. Choosing input signals in a clever way, can have certain advantages as is shown in literature [21, Ch. 2][40, Ch. 2]. From this literature the theory in this subsection can be extracted.

Sampling can be expressed in the continuous time domain, as a multiplication of a signal $u(t)$ with a series of Dirac impulses,

$$\tilde{u}_d(t) = \sum_{k=-\infty}^{\infty} u(t)\,\delta(t - kT_s), \tag{2.1}$$

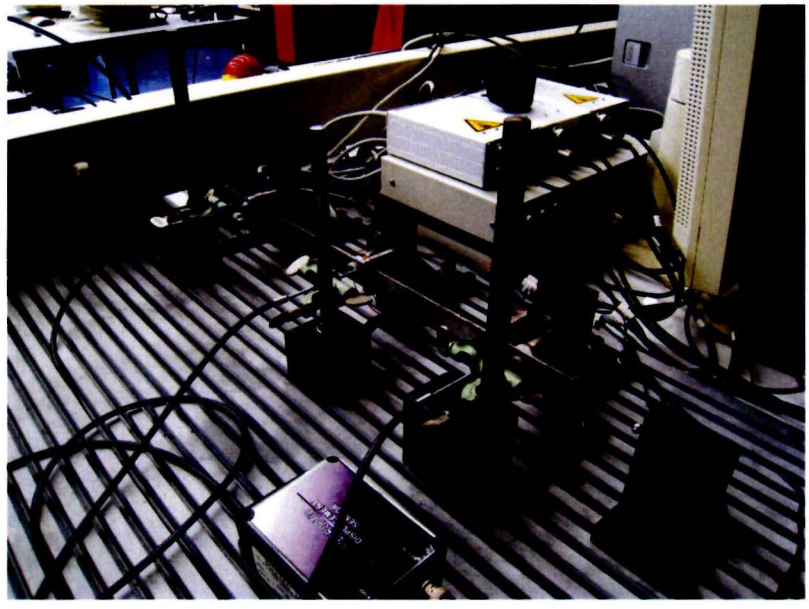

(a)

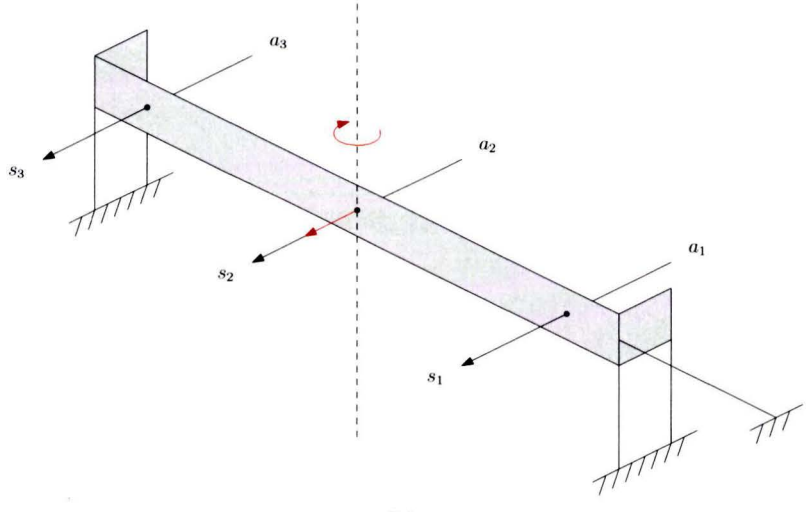

(b)

Figure 2.1: Photo of the experimental setup (a), and sketch of the setup (b) showing the two unrestricted degrees of freedom (red) and the sensor and actuator locations, s_i and a_i.

or in the discrete time domain as

$$u_d(k) = u(kT_s), \tag{2.2}$$

where, k is an integer number. The sampled signal is brought the frequency domain by the following Fourier transform:

$$U_d(\omega) = \sum_{k=-\infty}^{\infty} u_d(k) e^{-j\omega k T_s}. \tag{2.3}$$

Although the signal $u_d(k)$ evolves in discrete time, it's spectrum is defined in the continuous frequency domain. Note that because k is integer, this spectrum is periodic with period $\omega_s = \frac{2\pi}{T_s}$.

Equation (2.3) considers an infinite number of samples, i.e., $k = -\infty, \ldots, \infty$. Because measurements are performed in finite time, $\tilde{u}_d(t)$ is multiplied with a rectangular window $w(t)$, which is defined as follows

$$w(t) = \begin{cases} 1 & \text{if } 0 \leq t < T \\ 0 & \text{elsewhere.} \end{cases}$$

This selects a finite number of samples, and therefore reduces (2.3) from an infinite summation to

$$U_d(\omega) = \sum_{k=0}^{N-1} u_d(k) e^{-j\omega k T_s}, \tag{2.4}$$

where N is the number of samples in period T.

In Figure 2.2a the spectrum $W(\omega)$ of a rectangular window $w(t)$, for $T = 2$ is shown. The magnitude of $W(\omega)$ shows an oscillation that decreases in magnitude away from the origin. This spectrum has zero cross-overs at multiples of $\omega = \frac{2\pi}{T}$, which is an important property in the motivation for choosing periodic input signals, as can best be explained by discussing a sinusoidal signal.

For a sinusoidal signal $u(t) = \sin(\omega_u t)$, the Fourier transformation

$$U(j\omega) = j\pi(\delta(\omega + \omega_u) - \delta(\omega - \omega_u)) \tag{2.5}$$

consists of two Dirac impulses at $\pm\omega_u$. When the sinusoidal signal $u(t)$ is multiplied with the window $w(t)$, in the frequency domain the spectra $U(\omega)$ and $W(\omega)$ must be convoluted. Since convolution with a Dirac impulse shifts the origin of a function, $W(\omega) * U(\omega)$ is the sum of two shifted spectra $W(\omega)$, with their origins at $\pm\omega_u$.

With this knowledge, the favorable property of the rectangular window can be shown. In Figure 2.2 the spectra of two windowed sinusoidal signals are shown. The first sine has a frequency $\omega_u = 10\pi$ rad/s (blue $-$), which is a multiple of $\frac{2\pi}{T}$. Observe that by evaluating the spectrum at $\omega = n\frac{2\pi}{T}$ ($\times$), the spectrum has a value at $\pm 10\pi$, i.e., the exact frequency of the signal, and is zero elsewhere. This is a perfect frequency domain representation of the signal, since both the frequency and magnitude of the signal, can be observed from the spectrum. The second sine has a frequency $\omega_u = 12.5\pi$ rad/s (red $--$), which does not align with the zeros of the window spectrum. When the spectrum is evaluated at $\omega = n\frac{2\pi}{T}$ ($\times$), it can be seen that the content of the signal is smeared over neighboring frequencies, and the information regarding the magnitude and frequency of the signal is not clear in the spectrum. This effect is called leakage, and strongly motivates the use of multi-sine excitation signals, with frequency content at $\omega = n\frac{2\pi}{T}$ and zero elsewhere.

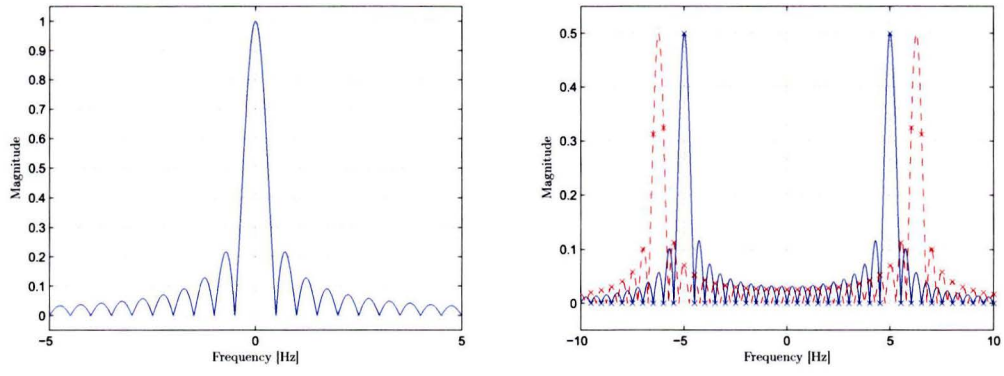

(a) (b)

Figure 2.2: (a) Spectrum $W(j\omega)$ of window $w(t)$. (b) Spectra of windowed sines, with frequency $\omega_u = 10\pi$ rad/s (blue $-$), which is a multiple of $\frac{2\pi}{T}$ ($\times$), and with frequency $\omega_u = 12.5\pi$ rad/s (red $--$), which does not match the grid.

2.2.2 Bias and variance

Although signal leakage can be completely removed by using periodic input signals, there are still other sources that can cause bias and variance in the estimated transfer function. Since this is not desirable, it is important to be aware of the maximum error that can be present in a model. These modeling errors are described in [27, 40] for periodic excitation signals and in [3, 18, 27, 40] for random excitation.

From the spectra of the measured periodic input and output signals, $U(k)$ and $Y(k)$, the frequency response is estimated as $G(j\omega_k) = \frac{Y(k)}{U(k)}$. Because of measurement and actuation noise in the measured signals, these spectra can be split up in the true spectra, $U_0(k)$ and $Y_0(k)$, and circular complex normally distributed noise [40, S. 14.16], $N_U(k)$ and $N_Y(k)$, i.e.,

$$U(k) = U_0(k) + N_U(k), \tag{2.6}$$
$$Y(k) = Y_0(k) + N_Y(k). \tag{2.7}$$

According to [40, S. 2.4], the relative bias $b(k)$ of $G(j\omega_k)$ caused by this noise, is given by

$$b(k) = \frac{\mathbb{E}\{G\} - G_0}{G_0} = -\exp\left(-\frac{|U_0|^2}{\sigma_U^2}\right)\left(1 - \frac{\sigma_{YU}^2}{\sigma_U \sigma_Y}\frac{U_0 \sigma_Y}{Y_0 \sigma_U}\right), \tag{2.8}$$

and if the signal-to-noise ratio (SNR) of the input, $\frac{|U_0|}{\sigma_U}$, and output, $\frac{|Y_0|}{\sigma_Y}$, are larger than 10 dB, the bias of $G(j\omega_k)$ is less than 0.01%. This is due to the periodicity of the input and output signals. It is also claimed that for stochastic excitation the maximum possible bias is much higher.

In the case that there is no actuation noise, $\sigma_U^2 = 0$, the estimate of the plant is unbiased, for both periodic and random excitations. However, it should be noted that noise excitation introduces leakage effects, as discussed in the previous subsection, and therefore the estimate still contains systematic errors.

In [40, S. 2.4] the variance σ_G^2 of $G(j\omega_k)$ is given by

$$\sigma_G^2 = |G_0|^2 \left(\frac{\sigma_Y^2}{|Y_0|^2} + \frac{\sigma_U^2}{|U_0|^2} - 2\Re\left(\frac{\sigma_{YU}^2}{Y_0 \bar{U}_0}\right)\right). \tag{2.9}$$

It can be seen that the variance also benefits from a high signal-to-noise ratio. The most straightforward way to accomplish a high SNR, is by increasing the power of the input signal. However, when periodic excitation is used, it can also be achieved by averaging over sequential periods. By averaging over M periods, the averaged spectrum X_M of a signal $x(t)$ is given by

$$X_M = \frac{1}{M} \sum_{m=1}^{M} \left(X_0 + N_X^{[m]} \right). \tag{2.10}$$

The expected value of the spectrum, given by

$$\mathbb{E}\left\{ \frac{1}{M} \sum_{m=1}^{M} \left(X_0 + N_X^{[m]} \right) \right\} = \frac{1}{M} \sum_{m=1}^{M} \mathbb{E}\left\{ X_0 + N_X^{[m]} \right\} = X_0, \tag{2.11}$$

is the same for every period and therefore remains constant. On the other hand, the variance, which is given by

$$\sigma_{X_M}^2 = \mathbb{E}\left\{ \left| \frac{1}{M} \sum_{m=1}^{M} \left(N_X^{[m]} \right) \right|^2 \right\}, \tag{2.12}$$

does change. By assuming that the noise of each period is uncorrelated with all other periods, the variance is

$$\sigma_{X_M}^2 = \frac{1}{M^2} \sum_{m=1}^{M} \mathbb{E}\left\{ \left| N_X^{[m]} \right|^2 \right\} = \frac{1}{M} \sigma_X^2. \tag{2.13}$$

This means that the signal-to-noise ratio of X_M is given by

$$\frac{|X_M|}{\sigma_{X_M}} = \sqrt{M} \frac{|X_0|}{\sigma_X}, \tag{2.14}$$

and thus is concluded that averaging over periods increases the SNR of the signal. Since this applies to both the input and output signal, the signal-to-noise ratios of both U and Y increase, which means that both the bias and variance decrease. In [27] it is stated that for stochastic input signals the transfer function estimation is asymptotically unbiased with increasing M, but the variance remains constant.

2.2.3 Experimental results

For estimating the frequency response of the system, a closed-loop measurement has been carried out. This has been done by exciting the system with a multi-sine on the plant input. This multi-sine contains multiples of 1 Hz, up to the Nyquist frequency, with a uniform spectrum and random phase. The period time is 1 s, which is also the width of the rectangular window. This choice assures that no signal leakage occurs, as explained in Subsection 2.2.1. A measurement of 1200 s has been carried out, which means that the signal-to-noise ratio $\frac{|Y_0|}{\sigma_Y}$ of the output, is increased by more than 30 dB relative to its actual value. The input signal is known exactly, i.e., $\sigma_U^2 = 0$, and therefore the SNR of the is ∞.

The resulting transfer function estimations shown in Figure 2.3, are obtained from closed-loop measurement data, by dividing the process sensitivity by the sensitivity. The figure shows G_z (blue $-$), the frequency response from input $u = a_1 = a_3$ to performance output $z = s_2$, and G_y (green $--$) which is the frequency response from u to measured output $y = \frac{s_1 + s_3}{2}$. It is clear that there are some similarities, as well as some differences between these two responses. First of all it can be seen that in the low frequency range both frequency

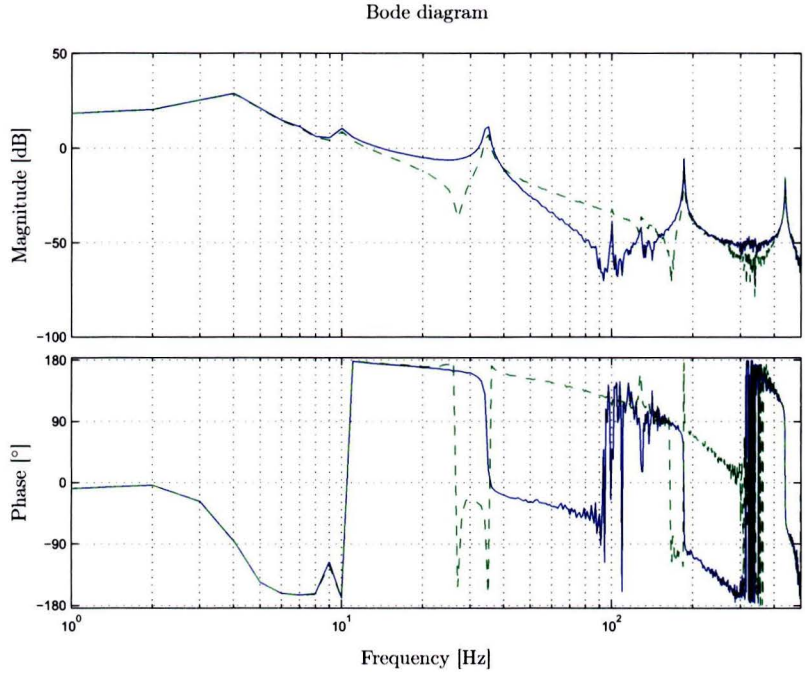

Figure 2.3: Transfer function estimation of the experimental setup, with G_z (blue $-$) the frequency response from $u = a_1 = a_3$ to $z = s_2$, and G_y (green $--$) the response from u to $y = \frac{s_1+s_2}{2}$.

responses are identical. In this region only the rigid body dynamics of the flexible beam are excited. For higher frequencies, the resonances of both responses are located at the same frequencies and the magnitudes are similar. The phase of the resonances at 35 Hz and 185 Hz are opposite for G_z and G_y, while for the resonance at 430 Hz the phase is the same. The appearance and location of the anti-resonances is different for the two outputs, and in these regions the performance problem indicated in Section 1.2 will most likely be present. The resonances at 4 Hz and 10 Hz are caused by the suspension of the beam on leaf springs, the other resonances are caused by the flexibility of the beam, which will be further discussed in the next section.

2.3 First principles modeling of a flexible beam

One of the reasons for choosing a flexible beam as experimental setup, is that first principles modeling for beams is well-studied in literature [14, 30, 43, 49]. A physical model is important in explaining the dynamical behavior of the system, and interpreting results of simulations and experiments. For more complex systems, such as a wafer stepper, analytical modeling based on first principles is often burdensome. However, in this thesis the model is used to study whether control can deal with flexible dynamics. When results are established, it may be unnecessary to derive analytical models for more complex systems.

A flexible beam (also known as Euler-Bernoulli beam) with free ends, is described by the following partial differential equation,

$$m\frac{\partial^2 w(x,t)}{\partial t^2} + EI\frac{\partial^4 w(x,t)}{\partial x^4} = p(x,t), \tag{2.15}$$

where x is position, t is time, w is the lateral deflection of the beam, m is the mass, E is the Young's modulus, I is the second moment of area, and p contains all external (lateral) forces. If the problem is assumed to be separable in time and space, i.e., $w(x,t) = W(x) f(t)$, (2.15) can be written as two ordinary differential equations,

$$EI\frac{\partial^4 W(x)}{\partial x^4} - \omega^2 m\frac{\partial^2 W(x)}{\partial t^2} = 0, \tag{2.16}$$

$$\frac{d^2 f(t)}{dt^2} + \omega^2 f(t) = 0. \tag{2.17}$$

In general, this assumption is valid for partial differential equations in the form of (2.15). By solving the eigenvalue problem, the eigenfrequencies ω_r, and mode shapes W_r, that are nontrivial solutions for (2.16) can be found. The deflection is then given by,

$$w(x,t) = \sum_{r=1}^{\infty} W_r(x)\, q_r(t), \tag{2.18}$$

where the dynamics are described by an infinite set of uncoupled ordinary differential equations,

$$\ddot{q}_r(t) + \omega_r^2 q_r(t) = \int_0^L W_r(x)\, p(x,t)\, dx. \tag{2.19}$$

In the frequency domain this gives the following summation for the transfer function,

$$G(x,s) = \sum_{r=1}^{\infty} \frac{W_r(x)\, P_r}{s^2 + \omega_r^2}. \tag{2.20}$$

Note that this is a model of the undamped dynamics of the beam. If desired, a damping term can be added to (2.15), see for instance [7], or proportional damping can be added to (2.20). For more details on this particular model, see [17, Ch. 2].

Figure 2.4 shows the mode shapes $W_r(x)$ of the translational modes ($-$), and the rotational modes ($--$), as well as the locations of the sensors and actuators, at 50 mm, 250 mm and 450 mm. It can be seen that the rotational modes are unobservable by the average of s_1 and s_3, due to their rotational symmetry, and by s_2 which is located in the nodes of these mode shapes. This means that these modes do not influence the input-output behavior of the system, the specific choice of sensor and actuator locations. The difference in the dynamics of G_y and G_z is explained by analyzing the translational mode shapes as in the following paragraphs.

The eigenfrequencies of the system are independent of the locations of actuators and sensors, which means that the poles of G_y and G_z are identical. The pole at 35 Hz is caused by mode 3, the pole at 185 Hz is caused by mode 5, and the pole at 430 Hz is caused by mode 7. The poles at 5 Hz and 10 Hz are not caused by the flexibility of the beam, but by the leave springs on which the beam is suspended. These poles can be linked to the rigid body modes, mode 1 and 2.

Although the poles are identical for both transfer functions, the zeros are not. Because the transfer function is a summation of modes, see (2.20), the sign of the phase of two neighboring modes will determine whether or not there will occur a zero between these poles, as shown in [31]. When the sensors and actuators are collocated, as is the case for G_y, the sign of the mode shape is the same at both the sensor and the actuator location. This means that actuation in positive direction, will cause a displacement in positive direction for all translational modes. Therefore, a zero will occur between any two neighboring poles. When sensors and actuators are noncollocated, as for G_z, it is also possible that actuation

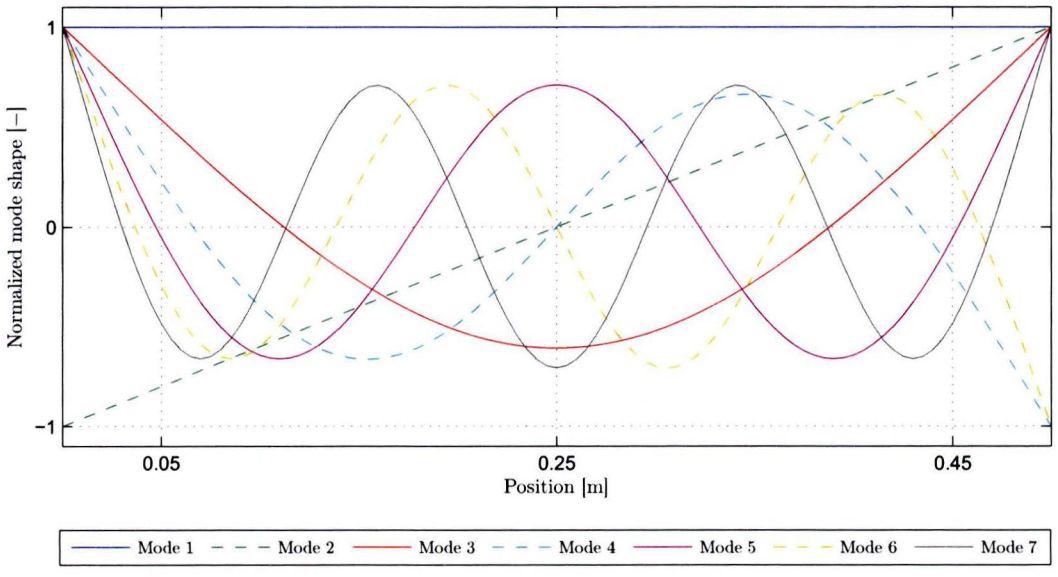

Figure 2.4: First seven analytical mode shapes of a flexible beam with the same parameters as the experimental setup. The translational modes are solid lines, the rotational modes are dashed lines. Actuator a_1 and sensor s_1 are positioned at 0.05 m, sensor s_2 at 0.25 m, and actuator a_3 and sensor s_3 are at 0.45 m.

in a positive direction, will cause a displacement in negative direction at the sensor location. This is the case for modes 3 and 5. Therefore, between mode 1 and mode 3 no zero occurs, since they have opposite phase, but between modes 3 and 5 there is a zero, because they have the same phase. The fact that a zero occurs between modes 1 and 3 indicates a performance problem if $|G_y K| \gg 1$ at this frequency, as explained in Section 1.2. Note that if the actuators had been positioned at the ends of the beam, there would not have been any zeros in G_z, because this guarantees an alternating sign for neighboring modes.

Although this analytical model explains the dynamics of the flexible beam, it is unpractical to work with since it describes the deflection of the beam with an infinite number of modes. Therefore, the finite element method, see e.g. [6], has been used to derive the state-space model in Figure 2.5, as described in [14]. This figure also shows the nonparametric model and it can be seen that, although there is a very close match between the finite element model model and frequency response function, at some frequencies there are small differences in the dynamics. First of all the rotational modes 4 and 6 are not observed in the finite element model, but are present in the frequency response of the setup, at respectively 100 Hz and around 330 Hz. Furthermore, in the nonparametric model the effects of aliasing are visible, at approximately 170 Hz and 330 Hz. This is caused by resonances lying beyond the Nyquist frequency, and can be linked to higher order modes that have been excluded from the analytical model. The last difference between the frequency response function and the physical model, occurs at approximately 130 Hz, and is caused by a nonlinear phenomenon in the setup.

2.4 Conclusions

In this chapter, an introduction to the flexible beam experimental setup has been given. A nonparametric model of the plant dynamics has been identified and analytical modeling of

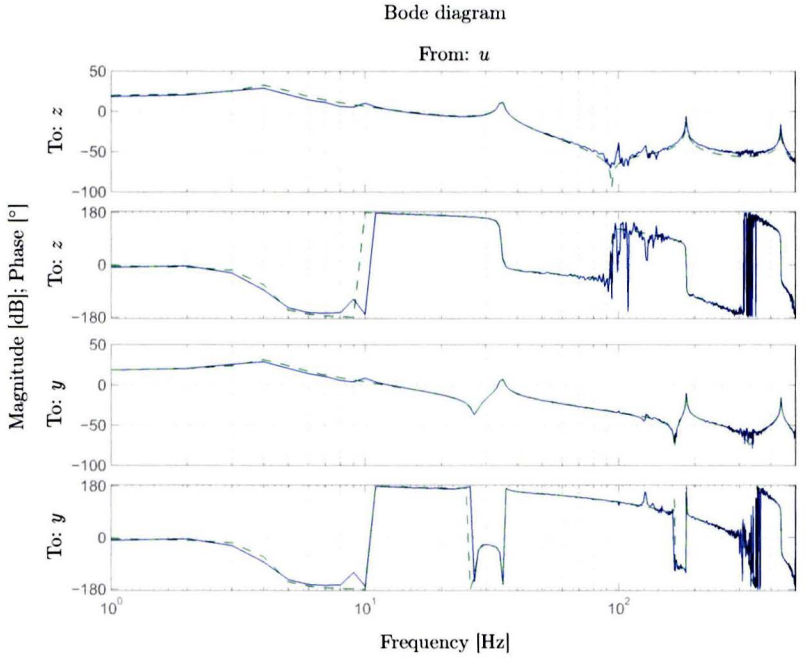

Figure 2.5: FEM model of the flexible beam (green −−) compared with the frequency response function of the setup (blue −).

the flexible beam has been discussed, leading to the following conclusions.

- The nonparametric model of the flexible beam setup, obtained by means of system identification, provides a first indication of the true plant dynamics, and can therefore be used for manual controller design. During the identification experiment periodic multi-sine excitation signals have been used, which results in a frequency response function that is unbiased. By using large measurement times and averaging over periods, the obtained model has a low variance. These are valuable properties for the parametric identification method in Chapter 4 as well, since it relies on an accurate frequency response function of the true plant dynamics.
- The obtained finite element model can be used for simulation of the open-loop or closed-loop system response, and to predict the outcome of controller synthesis, prior to parametric identification of the plant. This is helpful during weighting filter design for the parametric identification procedure in Chapter 4.
- The analytical model of the flexible beam provides insight in the dynamics of the system, which is helpful in understanding the problems occurring in control of structures with flexible dynamics. It shows that the representative scenario in Figure 1.5 will indeed cause performance problems on the flexible beam, and therefore it can be concluded that the setup is a suitable prototype to study control of light-weight positioning systems.

Chapter 3

$\mathcal{H}_\infty$-optimal inferential control

For the development of next generation wafer stages with flexible dynamics, developments in new control theory will play an important role. In Section 1.2, it was shown that standard control techniques do not guarantee good performance for structures with flexible dynamics, and therefore a new approach is proposed in this chapter.

Because wafer stages are complex MIMO structures, $\mathcal{H}_\infty$-optimal control will be used. This control technique is well studied in literature, see for instance [10, 16, 45], and is able to deal with such complex systems. Furthermore, it is able to deal with model uncertainty, in contrast to $\mathcal{H}_2$-optimal control, see e.g. [45].

To deal with the flexible dynamics in lightweight structures, inferential control will be used. This control technique is used in chemical process control, see [4, 28, 45, 47], when a performance output is not available for feedback. This is similar to the scenario in Section 1.4, that represents the difficulties in control of structures with flexible dynamics. In order to obtain $\mathcal{H}_\infty$-optimal inferential control, the control problem must be formulated such that it can be used with standard controller synthesis algorithms, that it can provide internal stability, and that it is able to deal with model uncertainty.

Since $\mathcal{H}_\infty$-optimal inferential control will be an extension of the standard robust control techniques, in Section 3.1 some important aspects of $\mathcal{H}_\infty$-optimal control are discussed. Then, in Section 3.2 inferential control is introduced, and cast in the generalized plant formulation. In Section 3.3, the conclusions of this chapter are presented.

3.1 $\mathcal{H}_\infty$-optimal control

Controller design for complex MIMO structures is often cumbersome, and not straightforward to understand. Therefore, $\mathcal{H}_2$ and $\mathcal{H}_\infty$-optimal control are often used to design controllers that stabilize the plant and optimize its performance, since they are able to deal with MIMO problems appropriately. In contrast to the $\mathcal{H}_2$-optimal control $\mathcal{H}_\infty$-optimal control can be used to synthesize controller designs, that are robust against model uncertainties. This makes $\mathcal{H}_\infty$-optimal control, a suitable choice for complex structures such as wafer stages.

In this section, standard $\mathcal{H}_\infty$-optimal control will be discussed, as it is known in literature, see e.g. [45]. The goal of $\mathcal{H}_\infty$-optimal control is to minimize the $\mathcal{H}_\infty$-norm of a (weighted) closed-loop system, which is useful in perspective of optimizing performance objectives and robustness against uncertainties. The following relevant aspects are discussed in this section.

Internal stability of the closed-loop system is a general objective in control engineering, because this is a requirement for meaningful controller design. This subject is discussed in Subsection 3.1.1. Then, in Subsection 3.1.2 the synthesis of optimal and suboptimal

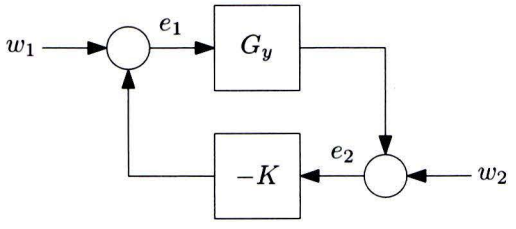

Figure 3.1: closed-loop feedback structure with plant G_y and controller K.

controllers is discussed, and Subsection 3.1.3 is about the presence of model uncertainties in the context of $\mathcal{H}_\infty$-control.

3.1.1 Internal stability

In order to keep all signals in a closed-loop system finite, it is a requirement that the plant G is internally stabilized by controller K. In the scenario introduced in Section 1.4, G_z does not influence the dynamics of the feedback loop, and therefore it is not included in the following definition of internal stability, but is should be noted that $G_z \in \mathcal{RH}_\infty$ is sufficient for the result to hold.

Definition 3.1 (Internal stability [50, Ch. 5]). Consider the closed-loop system in Figure 3.1 which is well posed and has no hidden unstable modes. Then, this system is internally stable if and only if all states of K and G_y go to zero from all initial states, when $w_1 = 0$ and $w_2 = 0$.

This is the case when e_1 and e_2 are bounded signals for any bounded inputs w_1 and w_2. This requirement is satisfied if all four closed-loop transfer functions from $w = \begin{bmatrix} w_2 & w_1 \end{bmatrix}^T$ to $e = \begin{bmatrix} e_2 & e_1 \end{bmatrix}^T$ are stable, i.e.,

$$\begin{bmatrix} I - G_y S K & G_y S \\ -SK & S \end{bmatrix} \in \mathcal{RH}_\infty, \tag{3.1}$$

with $S = (I + KG_y)^{-1}$, hence this is called the four-block problem. If $G_y \in \mathcal{RH}_\infty$ and $K \in \mathcal{RH}_\infty$ the closed-loop system is internally stable if and only if $S \in \mathcal{RH}_\infty$.

Equation (3.1) is equivalent to

$$\begin{bmatrix} G_y \\ I \end{bmatrix} S \begin{bmatrix} K & I \end{bmatrix} \in \mathcal{RH}_\infty, \tag{3.2}$$

which has the same poles and is commonly used instead.

3.1.2 Controller synthesis

The $\mathcal{H}_\infty$-norm is equal to the maximum singular value of a transfer function. By weighting the closed-loop transfer functions of a system, such as the sensitivity or complementary sensitivity, it can therefore be used as a measure for the achieved performance. It is also equal to the induced 2-norm or induced power-norm [45]. The $\mathcal{H}_\infty$-norm can be computed according to the following theorem.

Theorem 3.1 ($\mathcal{H}_\infty$-norm computation [9, Ch. 2]). *The $\mathcal{H}_\infty$-norm can be computed by iteratively finding the smallest γ, such that*

$$\begin{bmatrix} A + BR^{-1}D^T C & BR^{-1}B^T \\ -C^T\left(I + DR^{-1}D^T\right)C & -\left(A + BR^{-1}D^T C\right)^T \end{bmatrix}, \tag{3.3}$$

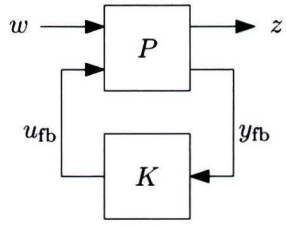

Figure 3.2: General control configuration.

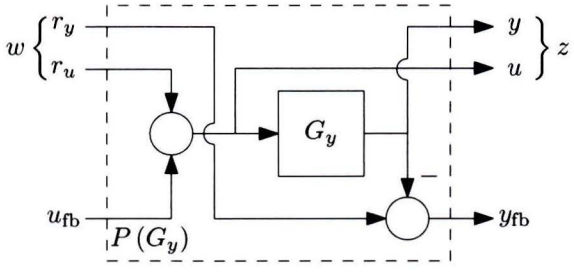

Figure 3.3: Plant G_y and the interconnection structure form the generalized plant P.

where $R = \gamma I - D^T D$, and (A, B, C, D) is the state-space realization of the system, has no eigenvalues on the imaginary axis.

The controller problem is often cast in the general control configuration in Figure 3.2, which was introduced by Doyle [8], because problems in this form can be solved with the available controller synthesis algorithms. In Figure 3.2 configuration the generalized plant contains the plant G and the four-block interconnection structure, where $w = \begin{bmatrix} r_y & r_u \end{bmatrix}^T$ are the external inputs and disturbances, and $z = \begin{bmatrix} y & u \end{bmatrix}^T$ the outputs. The control objective then becomes: compute the controller that minimizes the transfer function from w to z, i.e., minimize the closed-loop transfer function. The general control configuration can be extended with an uncertainty model in a straightforward fashion, as shown in Subsection 3.1.3. Here, this control configuration is used to analyze the four-block problem (3.2), and in Section 3.2 also the new control theory will be cast in this form.

The internal structure of P for the four-block problem (3.2) is shown in Figure 3.3, and is given by

$$P = \left[\begin{array}{cc|c} 0 & G_y & G_y \\ 0 & I & I \\ \hline I & -G_y & -G_y \end{array}\right]. \tag{3.4}$$

Using the general control configuration, the control problem can be solved by finding sub-optimal controller $K(\gamma)$, such that

$$\mathcal{J}(P, K) = \|W \mathcal{F}_l(P, K) V\|_\infty < \gamma, \tag{3.5}$$

where W and V are weighting filters, and iteratively searching for the minimal value of γ. Suboptimal controller synthesis is explained more detailed in Appendix A.

The four-block optimization problem (3.5) can be formulated as a normalized left coprime factor robust stabilization problem, and therefore it is possible to find an exact solution for the optimal value of γ, as proved in [29, Ch. 4]. The solution for the optimal value of γ is given by

$$\gamma_{\text{opt}} = \inf_{K \text{ stabilizing}} \|\mathcal{F}_l(P, K)\|_\infty = \left(1 - \left\|\begin{bmatrix} \tilde{N} & \tilde{D} \end{bmatrix}\right\|_H^2\right)^{-\frac{1}{2}}, \tag{3.6}$$

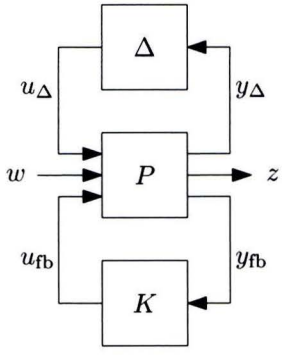

Figure 3.4: General control figuration with model uncertainty.

where $\left\{\tilde{N}, \tilde{D}\right\}$ is a left coprime factorization[1] of G_y. This eliminates the iteration step required for computing the optimal controller.

3.1.3 Model uncertainty

An accurate and exact model of the plant is available for controller synthesis as described above. However, in practice there are differences between the model and the plant, due to modeling errors, or because the system dynamics are too complex to be described by one model. In order to address these differences, model uncertainty can be used to analyze the stability properties of a controller for a set of plants, i.e., the robustness of the controller can be analyzed. This motivates the use of the $\mathcal{H}_\infty$-norm in a control context, because it provides an upper bound for all transfer functions in a matrix, over all frequencies. In the four-block problem (3.2), consequently an upper bound for the sensitivity is found, and thus a minimum for the stability margins is provided. In contrast, the $\mathcal{H}_2$-norm bounds the area under the transfer functions, and does not guarantee any robustness.

Uncertainty in the dynamics of the plant can be modeled with a stable perturbation Δ, $\|\Delta\|_\infty < \gamma$ on the nominal model. The general control figuration in Figure 3.2 can be extended with this Δ-block as shown in Figure 3.4.

By applying the lower fractional transformation $M = \mathcal{F}_l(P, K)$ the so-called $M\Delta$-structure in Figure 3.5 is obtained, which can be used to analyze the stability of a closed-loop system with uncertainties, using the well known *small gain theorem.*

Theorem 3.2 (Small gain theorem). *Suppose $M \in \mathcal{RH}_\infty$. Then the interconnected system shown in Figure 3.5 is well-posed and internally stable for all $\Delta \in \mathcal{RH}_\infty$ if and only if*

$$\|M_{11}\Delta\|_\infty < 1. \tag{3.7}$$

The proof of this theorem can be found in, for instance, [50, Ch. 9].

The essence of the small gain theorem is, that if both M and Δ are stable, the only possible source of instability is the feedback loop, and it is proved that the closed-loop system is internally stable if and only if $\|M_{11}\Delta\|_\infty < 1$, which is called robust stability. Similarly, it can be evaluated whether (normalized) performance criteria are met, with $\|M_{22}\Delta_P\|_\infty < 1$. In this case $\|\Delta_P\|_\infty$ is an artificial perturbation, i.e., it is not a model uncertainty but only an expression which is equivalent to the performance criterion.

For a system with uncertainties, the solution for the optimal controller as given in the previous subsection can no longer be used. However, in literature [10] a controller synthesis algorithm is available, of which numerical implementations exist.

[1] See Definition 4.2.

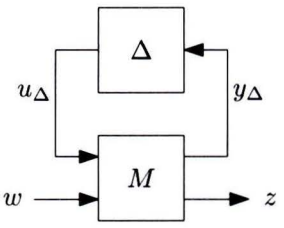

Figure 3.5: The $M\Delta$-structure can be used to analyze stability of an closed-loop system with uncertainties.

When there are multiple uncertainties, i.e., the Δ-block is MIMO, the perturbations can possess a certain structure, in which case the structured singular value μ_Δ [37] should be used to analyze stability and performance instead of the $\mathcal{H}_\infty$-norm, which can substantially reduce the conservatism of the solution.

Definition 3.2 (Structured singular value [37]). The structured singular value is defined as

$$\mu_\Delta(M) = \left(\min_{\Delta} \{\bar{\sigma}(\Delta) | \Delta \in \mathbf{\Delta}, \det(I - \Delta M) = 0\}\right)^{-1}, \tag{3.8}$$

unless $\det(I - \Delta M) \neq 0 \; \forall \Delta \in \mathbf{\Delta}$, in which case $\mu_\Delta(M) = 0$.

In this definition the structure of Δ is given by

$$\mathbf{\Delta} = \{\operatorname{diag}(\delta_1 I_{r_1}, \ldots, \delta_S I_{r_S}, \Delta_{S+1}, \ldots, \Delta_{S+F}) \\ \left| \delta_i \in \mathbb{C}, \; \Delta_{S+j} \in \mathbb{C}^{m_j \times m_j}, \; 1 \leq i \leq S, \; 1 \leq j \leq F \right\}. \tag{3.9}$$

Structures where Δ_{S+j} is not square are also possible, although in the literature this assumption is often made, see for instance [37, 45].

Note that when both robustness and performance are evaluated, the problem is always structured, i.e.,

$$\hat{\Delta} = \begin{bmatrix} \Delta & 0 \\ 0 & \Delta_P \end{bmatrix}, \tag{3.10}$$

and thus $\mu_{\hat{\Delta}}(M)$ should be used.

3.2 Optimal inferential control

3.2.1 Motivation

In the previous section, the four-block problem (3.2) was introduced. By minimizing γ in (3.5), the optimal controller for plant G_y can be found, i.e., the performance at measured output y is optimized. However, for the representative scenario on the flexible beam setup, as introduced in Section 1.4, performance is required at output z. So far, this requirement has not been included in the control problem, and good performance of output z is therefore not guaranteed.

To illustrate that optimal performance at measured output y does not imply good performance at z, an optimal controller for G_y has been computed, using the finite element model from Section 2.3. Figure 3.6 shows the simulated step response of the closed-loop system, for both outputs. Although the response of measured output y is optimal, the response of performance output z shows a large vibration. From this example, it can be concluded that optimal control for G_y is insufficient to guarantee good performance for the

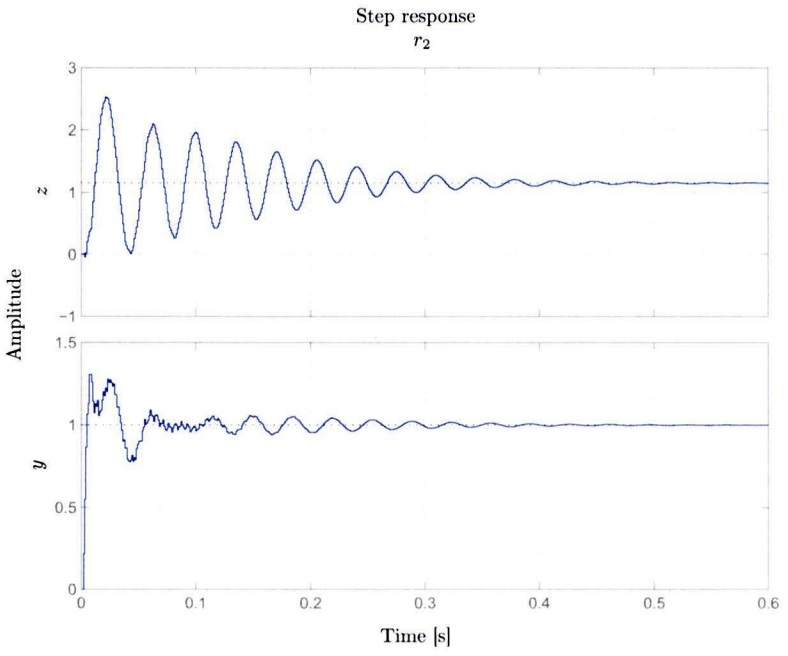

Figure 3.6: Step response simulation for the standard optimal controller on the physical model.

whole system. This is in contrast with optimal control of rigid structures, and once more motivates a different approach for systems with flexible dynamics.

3.2.2 Inferential control

For structures with flexible dynamics, where performance output z is not equal to the measured output y, standard control theory is insufficient and new methods must be explored. A solution can be found in the literature on chemical process control [28, 39, 45, 47]. In chemical plants, often the performance variable is not available during normal operation. To solve this problem, a secondary measurement is used to control the performance variable indirectly, which is called *inferential* or *indirect* control.

The two control configurations that are commonly used, are shown in Figure 3.7. In control configuration (a), measured output y is used for feedback control. The reference signal r_z for the performance output, is filtered by F to obtain a reference signal $r_y = Fr_z$ that is needed in the control loop. Control configuration (b) estimates z by $\hat{z} = Ey$, and uses the estimate for feedback control.

The intended use of this control theory is $\mathcal{H}_\infty$-optimal control, and therefore the control configuration in Figure 3.8 is introduced. In this control configuration, the controller takes the reference signal r_z and measured output y as inputs, i.e., in contrast to standard feedback controllers, the inferential controller has two degrees of freedom, $K = \begin{bmatrix} K_1 & K_2 \end{bmatrix}$. The filter F and estimator E are absorbed in the controller, and maximum freedom in the controller design is allowed. This freedom will be left to the controller synthesis algorithm, such that an optimal result can be achieved.

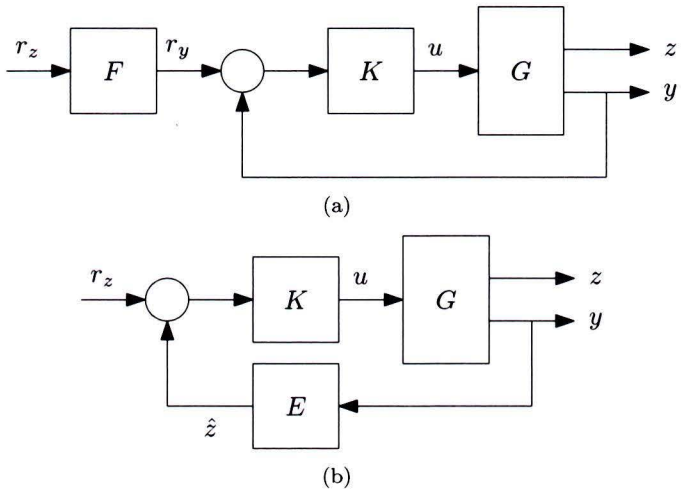

Figure 3.7: Two control configurations for inferential or indirect control, as used in process control.

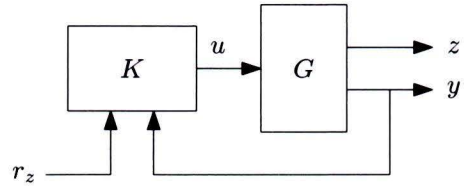

Figure 3.8: Inferential control configuration for motion systems with flexible dynamics.

3.2.3 $\mathcal{H}_\infty$-optimal inferential control

In Section 3.1 the use of $\mathcal{H}_\infty$-optimal control for complex structures, such as wafer stages, was motivated. In Subsection 3.2.1, it was shown that for structures with flexible dynamics standard optimal control is not sufficient, and therefore in Subsection 3.2.2, the inferential control structure was introduced.

In this subsection, the inferential control structure is cast in a form that is suitable for $\mathcal{H}_\infty$-optimal controller design. It is desired that standard robust control techniques can be used, and internal stability must be provided for this control structure. Furthermore it should be possible to extend the structure with an uncertainty model, and that performance for both the measured variable and the performance variable is part of the optimization criterion.

In order to provide internal stability for the inferential control configuration, inputs and outputs are added to the control scheme in Figure 3.8. These inputs and outputs are chosen such that the four-block problem (3.2) is contained in the closed-loop transfer function. This closed-loop transfer function is given by

$$\left[\begin{array}{c} G_z \\ \hline G_y \\ I \end{array}\right] S \left[\begin{array}{c|cc} K_1 & K_2 & I \end{array}\right]. \tag{3.11}$$

Observe that the lower right part is the four-block problem (3.2). Since the closed-loop system (3.11) consists of nine blocks, it will be called the nine-block problem.

When z would be chosen as performance output, the optimal solution for the controller synthesis problem would be $\left[\begin{array}{cc} 0 & K_2 \end{array}\right]$, i.e., tracking the reference signal would not be possible. Therefore, a reference filter T_r is introduced, as shown in Figure 3.9, and consequently $e_z = z - T_r r_z$ is the performance output, instead of z. The reference filter $T_r \in \mathcal{RH}_\infty$ should be chosen such that it resembles the desired closed-loop behavior, in order to obtain a meaningful problem formulation. It is important to choose T_r carefully, because it influences the optimal controller design. Note that r_y in this structure is not the reference signal for y, but represents measuring noise instead.

Now, the control structure in Figure 3.8 can be cast in the general control structure in Figure 3.2 as described in [36]. The resulting generalized plant P is shown in Figure 3.10, and is given by

$$P = \left[\begin{array}{ccc|c} -T_r & 0 & G_z & G_z \\ 0 & 0 & G_y & G_y \\ 0 & 0 & I & I \\ \hline 0 & I & -G_y & -G_y \\ I & 0 & 0 & 0 \end{array}\right]. \tag{3.12}$$

The closed-loop transfer function is given by

$$\mathcal{F}_l(P,K) = \left[\begin{array}{c} G_z \\ \hline G_y \\ I \end{array}\right] S \left[\begin{array}{c|cc} K_1 & K_2 & I \end{array}\right] - \left[\begin{array}{c|cc} T_r & 0 & 0 \\ \hline 0 & 0 & 0 \\ 0 & 0 & 0 \end{array}\right]. \tag{3.13}$$

Since the structure of the problem is now defined, it can be verified whether it provides internal stability.

Proposition 3.1 (Internal stability [36]). *Consider the closed-loop system in Figure 3.9 which is well posed and has no hidden unstable modes. Then, this system is internally stable, i.e., for $r_u = r_y = r_z = 0$ all states of K, G and T_r tend to zero from all initial states, if and only if $\mathcal{F}_l(P,K) \in \mathcal{RH}_\infty$.*

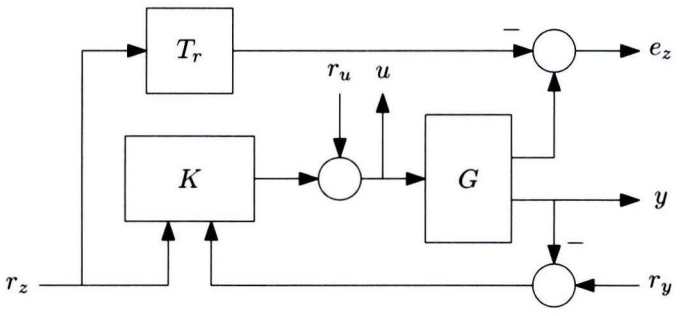

Figure 3.9: Inferential control structure suitable for the generalized plant formulation.

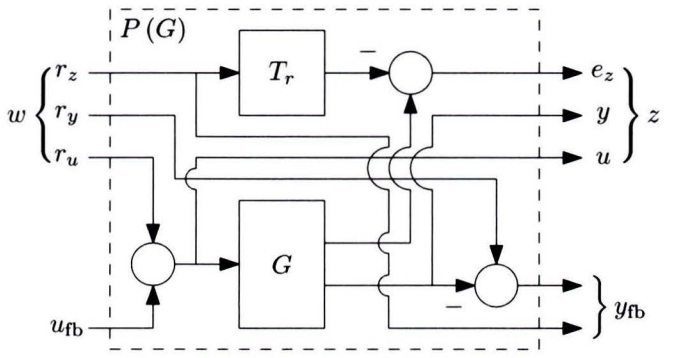

Figure 3.10: Plant G, reference filter T_r, and interconnection structure form the generalized plant P.

The proof of 3.1 is similar as in [50, Lemma 5.3], using that $T_r \in \mathcal{RH}_\infty$.
Using (3.13), the optimization criterion for the inferential control configuration becomes

$$\mathcal{J}(P,K) = \|W\mathcal{F}_l(P,K)V\|_\infty . \tag{3.14}$$

This optimization criterion has two degrees of freedom, i.e., $K = \begin{bmatrix} K_1 & K_2 \end{bmatrix}$ and shows certain similarities to the two-degree-of-freedom controllers in [23]. However, here the extra degree of freedom is used to infer the performance variables, instead of enhancing the performance of the measured variables.

The optimization problem can be solved using the standard suboptimal controller synthesis algorithm as described in Appendix A. Similar to the standard four-block problem (3.2), the inferential control structure can be extended with perturbations in the form of Δ-blocks.

3.3 Conclusions

In this chapter, $\mathcal{H}_\infty$-optimal inferential control has been discussed, and the following conclusions are drawn.

- The standard optimal control problem formulation does not deal adequately with structures with flexible dynamics, because it considers the measured variables to be the performance variables. The new inferential control configuration allows the use of performance variables that are not used for feedback, and has a two degree of freedom controller design that is used to improve the performance.

- In the inferential control configuration, the performance variables are inferred from the measured output of the system. This requires accurate knowledge of the system dynamics, and thus relies on the availability of high quality models.
- The inferential control configuration can be cast to fit the general control configuration (Figure 3.4). Therefore, standard robust control techniques can be used for controller synthesis, and model uncertainty can be added as usual. Stability of the closed-loop transfer function provides internal stability of the system.

Hereby, it can be concluded that the new inferential control structure is successfully combined with $\mathcal{H}_\infty$-optimal control, maintaining the advantages of both methods. Since the new control theory relies on accurate modeling of the plant dynamics, a control-relevant identification procedure is proposed in Chapter 4.

Chapter 4

Control-relevant identification

Inferential control, as introduced in Section 3.2, infers the performance output z from the measured output y. Since the relations between these two outputs are determined by the dynamics of the plant, it is crucial that an accurate model of these dynamics is available for controller synthesis. The intended use of inferential control is on the next-generation lightweight wafer stages, which are complex MIMO structures that are not straightforward to model accurately. Therefore, here will be focused on system identification, which is a reliable and fast method to obtain an accurate model of the system dynamics. Because the model is needed for controller synthesis, the goal of the identification procedure is to obtain a parametric model of the dynamics that are relevant for $\mathcal{H}_\infty$-optimal control, i.e., accurate modeling of the closed-loop dynamics is desired.

To identify the dynamics of a system, the difference between model and plant dynamics has to be minimized. In this chapter, a control-relevant identification criterion is used for this purpose. The optimal control-relevant model is then obtained by minimization of the identification criterion. In Section 4.1, coprime factorizations are discussed, since they play an important role in the identification procedure as proposed in this chapter. Section 4.2 is about the control-relevant identification criterion, which is related to the controller optimization criterion. Then, in Section 4.3, coprime factorization of the identification criterion is discussed, which reduces the size of the optimization problem such that the computational costs of the identification algorithm are reduced. Section 4.4 is about the algorithm for minimization of the identification criterion. In Section 4.5 the control-relevant system identification procedure is confronted with the flexible beam experimental setup, in order to verify the results on a real system. Finally, in Section 4.6, the conclusions of this chapter are presented.

4.1 Coprime factorization

The motivation for using coprime factors in the control-relevant identification procedure is based on two aspects. The first aspect is that it reduces the size of the identification criteria from four and nine blocks, to two and three blocks, for the standard and inferential control problem respectively, as is shown in Section 4.3. Generally, this reduces the computational costs of the identification algorithm. Furthermore, using coprime factors in the parametrization of model sets, has the advantage that it guarantees the plant is contained in the model set, if it is stabilized by the controller used during experiments. In this section, coprime factorization will be defined and a motivating example for using coprime factor uncertainty will be given.

Definition 4.1 (Coprime [29]). Suppose $\tilde{D}, \tilde{N} \in \mathcal{RH}_\infty$ have the same number of rows. Then $\tilde{D}$ and $\tilde{N}$ are *left coprime* if and only if there exist $U, V \in \mathcal{RH}_\infty$ such that the Bézout identity

$$\tilde{D}V + \tilde{N}U = I, \tag{4.1}$$

is satisfied.

Similarly, if D and N have the same number of columns, they are right coprime if there exist U and V such that $VD + UN = I$. Using this definition, the coprime factorization of a system is defined as follows.

Definition 4.2 (Coprime factorization [29]). The pair $\left\{\tilde{D}, \tilde{N}\right\}$ constitutes a *left coprime factorization* (LCF) of $G \in \mathcal{R}$ if and only if

1. $\tilde{D}$ is square and invertible,
2. $G = \tilde{D}^{-1}\tilde{N}$,
3. $\tilde{D}$ and $\tilde{N}$ are left coprime.

Similarly, the pair $\{D, N\}$ is a right coprime factorization (RCF) of G, if they are right coprime and $G = ND^{-1}$. A useful property of this definition is that $\tilde{D}$ and $\tilde{N}$ cannot have identical right half-plane zeros, because (4.1) then will not hold. Therefore, $\tilde{D}^{-1}\tilde{N}$ cannot have an unstable pole-zero cancellation, i.e., it has no hidden unstable modes.

Example 4.1 (Motivation for coprime factor uncertainty). Consider an unstable plant $G_0 = \frac{1}{s-2}$, which is stabilized by proportional feedback controller $K = 200$. The plant is modeled by $\hat{G} = \frac{1}{s+2}$, that is stable in contrast to the plant. This difference is illustrated in Figure 4.1(a), that shows the step responses of the open-loop plant $(-)$ and model $(--)$. The closed-loop step responses in Figure 4.1(b), on the other hand, show a remarkable similarity between the unstable plant and the stable model.

When robust control is pursued, it is a stringent requirement that the plant is included in the model set. With most common uncertainty structures, such as additive or multiplicative uncertainty, it is not possible to achieve this because Δ would be required to be unstable. However, the coprime factor uncertainty structure shown in Figure 4.2, is able to include unstable plants in the model set. The model set of this uncertainty structure is given by [29]

$$\mathcal{G} = \left(\hat{N} + \Delta_N\right)\left(\hat{D} - \Delta_D\right)^{-1},$$

where $\left\{\hat{N}, \hat{D}\right\}$ is a RCF of $\hat{G}$, and Δ_N, Δ_D are uncertainty models. The plant G_0 corresponds with $\Delta_N = 0$ and $\Delta_D = 4$, i.e., $\Delta_N, \Delta_D \in \mathcal{RH}_\infty$. The unstable plant is thus modeled solely by stable transfer functions.

4.2 Control-relevant identification criterion

To be able to use the proposed inferential control method, which is model based, it is important to have an accurate model of the dynamics of the system, such that the performance output z can be inferred from the measured output y. In order to obtain a model that contains the dynamics that are relevant for this purpose, and also for subsequent controller design, further analysis of the control objective is needed.

The aim of $\mathcal{H}_\infty$-optimal control is to minimize the control criterion, given by

$$\mathcal{J}(P_0, K) = \left\| W\mathcal{F}_l(P_0, K)V \right\|_\infty. \tag{4.2}$$

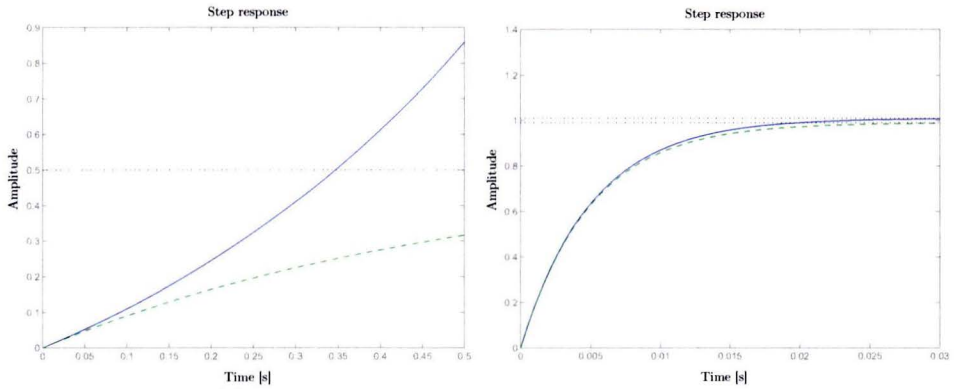

Figure 4.1: open-loop step response of the plant G_0 $(-)$ and model $\hat{G}$ $(--)$ (a), and closed-loop step response (b).

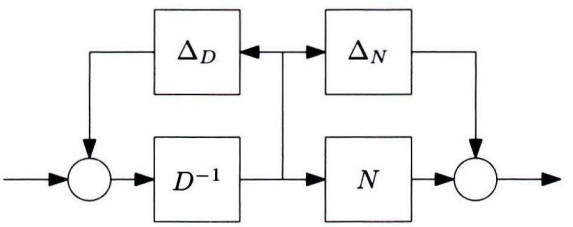

Figure 4.2: Coprime factor uncertainty structure of model set $\mathcal{G}$

This norm depends on the closed-loop transfer function of generalized plant P_0 and controller K. Since the exact dynamics of the real system are not given by an analytical expression, a model $\hat{P}$ needs to be used for controller synthesis. In [44], the triangle equation for norms is used to obtain an upper bound for (4.2), and then interpreted as follows.

The upper bound for (4.2) is given by

$$\mathcal{J}(P_0, K) \leq \mathcal{J}\left(\hat{P}, K\right) + \left\| W\left(\mathcal{F}_l(P_0, K) - \mathcal{F}_l\left(\hat{P}, K\right)\right) V \right\|_\infty . \tag{4.3}$$

Minimizing the first term of the right-hand side of this equation, is interpreted as finding the optimal controller for the model $\hat{P}$. The second term is interpreted as the worst-case performance degradation due to designing a optimal controller for the model $\hat{P}$, rather than for the plant P_0. This second term, therefore is a measure for the control-relevance of a model, and is used as identification criterion. The control-relevant model identification problem is therefore stated as

$$\hat{P}^{\mathrm{CR}} = \arg\min_{\hat{P}} \left\| W\left(\mathcal{F}_l(P_0, K) - \mathcal{F}_l\left(\hat{P}, K\right)\right) V \right\|_\infty . \tag{4.4}$$

Ideally, this norm should be minimized for the optimal controller, i.e., $K = K^{\mathrm{opt}}$. However, because the optimal controller is unknown, in the identification procedure an experimental controller K^{exp} is used. By iterating optimization of the model and controller, both the controller design and model improve. However, because in (4.4) always a controller is used that is designed for the previous model, convergence to the minimum of (4.2) is not guaranteed.

4.3 Coprime factorization of the identification criterion

The identification problem (4.4) will not be solved in this formulation. Instead, it will be expressed in coprime factors, as motivated in Example 4.1. By using coprime factorization as in the following approach, the optimization problem can be reduced in size. For standard optimal control, this leads to reduction of the four-block problem (3.2) to a two-block problem, and for the inferential control structure, the nine-block problem (3.13) reduces to a three-block problem. Generally, this reduces the computational cost of the identification algorithm.

The coprime factorization of the plant that is used to reduce the size of the identification criterion, is based on a left coprime factorization $\left\{\tilde{D}_e, \tilde{N}_e\right\}$ of the experimental controller K^{exp}, and diagonal weighting matrix V, i.e., the pair $\left\{\tilde{D}_e, \tilde{N}_e\right\}$ denotes an LCF of $\left[\begin{array}{c|cc} K_1^{\mathrm{exp}} V_3 & K_2^{\mathrm{exp}} V_2 & V_1 \end{array}\right]$. This coprime factorization is chosen such, that $\tilde{N}_e = \left[\begin{array}{c|cc} \tilde{N}_{e,3} & \tilde{N}_{e,2} & \tilde{N}_{e,1} \end{array}\right]$ is co-inner, which is defined as follows.

Definition 4.3 (Co-inner [29, Ch. 2]). A stable $p \times m$ transfer function $X(s)$, with $p \leq m$ is *co-inner* if

$$XX^* = I$$

for all $s \in j\mathbb{R}$.

A property of co-inner transfer functions, is that they do not influence the $\mathcal{H}_\infty$-norm in a right multiplication, i.e., if X is co-inner, $\|Y\|_\infty = \|YX\|_\infty$. Here, this property will be used to reduce the size of the identification problem for the inferential control configuration as in [36], but this method is applicable to other control configurations as well.

Substituting the closed-loop transfer function (3.13) in the identification criterion (4.4), gives

$$\mathcal{J}\left(\hat{P}, K^{\text{exp}}\right) = \left\| W \left(\left[\begin{array}{c} G_{0,z} \\ \hline G_{0,y} \\ I \end{array} \right] (I + K_2^{\text{exp}} G_{0,y})^{-1} - \left[\begin{array}{c} \hat{G}_z \\ \hline \hat{G}_y \\ I \end{array} \right] \left(I + K_2^{\text{exp}} \hat{G}_y\right)^{-1} \right) \left[\begin{array}{c|cc} K_1^{\text{exp}} & K_2^{\text{exp}} & I \end{array} \right] V \right\|_\infty . \quad (4.5)$$

Using the pair $\left\{\tilde{D}_e, \tilde{N}_e\right\}$, (4.5) can be written as

$$\mathcal{J}\left(\hat{P}, K^{\text{exp}}\right) = \left\| W \left(\left[\begin{array}{c} G_{0,z} \\ \hline G_{0,y} \\ I \end{array} \right] \left(\tilde{D}_e + \tilde{N}_{e,2} V_2^{-1} G_{0,y}\right)^{-1} - \left[\begin{array}{c} \hat{G}_z \\ \hline \hat{G}_y \\ I \end{array} \right] \left(\tilde{D}_e + \tilde{N}_{e,2} V_2^{-1} \hat{G}_y\right)^{-1} \right) \left[\begin{array}{c|cc} \tilde{N}_{e,3} & \tilde{N}_{e,2} & \tilde{N}_{e,1} \end{array} \right] \right\|_\infty . \quad (4.6)$$

Exploiting the fact that $\tilde{N}_e$ is co-inner, an important step can be taken, (4.6) can be reduced to

$$\mathcal{J}\left(\hat{P}, K^{\text{exp}}\right) = \left\| W \left(\left[\begin{array}{c} G_{0,z} \\ \hline G_{0,y} \\ I \end{array} \right] \left(\tilde{D}_e + \tilde{N}_{e,2} V_2^{-1} G_{0,y}\right)^{-1} - \left[\begin{array}{c} \hat{G}_z \\ \hline \hat{G}_y \\ I \end{array} \right] \left(\tilde{D}_e + \tilde{N}_{e,2} V_2^{-1} \hat{G}_y\right)^{-1} \right) \right\|_\infty . \quad (4.7)$$

This reduces the number of columns of the transfer function matrices in the identification criterion from three to one, which consequently will reduce the computational cost for finding the optimal model. In [36, Sec. IV] it is shown that the pair $\{N, D\}$, with $N = \left[\begin{array}{c|c} N_z & N_y \end{array} \right]^T$, defined by

$$\left[\begin{array}{c} N_z \\ \hline N_y \\ D \end{array} \right] = \left[\begin{array}{c} G_z \\ \hline G_y \\ I \end{array} \right] \left(\tilde{D}_e + \tilde{N}_{e,2} V_2^{-1} G_y\right)^{-1}, \quad (4.8)$$

is a right coprime factorization of G. First, it is shown that $\{N, D\}$ is a stable factorization of G, and then that there exist $U, V \in \mathcal{RH}_\infty$ such that the Bézout identity is satisfied, which makes $\{N, D\}$ a RCF of G. Using this definition, the control-relevant identification criterion can be written as

$$\min_{\hat{N}_z, \hat{N}_y, \hat{D}} \left\| W \left(\left[\begin{array}{c} N_{0,z} \\ \hline N_{0,y} \\ D_0 \end{array} \right] - \left[\begin{array}{c} \hat{N}_z \\ \hline \hat{N}_y \\ \hat{D} \end{array} \right] \right) \right\|_\infty , \quad (4.9)$$

which clearly shows that the identification problem can be solved by obtaining the optimal control-relevant coprime factors. The algorithm used to minimize (4.9) is discussed in the next section.

4.4 Minimizing the control-relevant identification criterion

The control-relevant identification criterion (4.9) depends on the coprime factorization of the model $\hat{G}$ and the plant G_0. Since the dynamics of the plant are not known in advance, they are acquired from experiments. Then, the measurement data is used to obtain the parameters of the model $\hat{G}$. Therefore, the identification procedure consists of the following three steps:

1. Obtain $\mathcal{F}_l\left(P_0, K^{\text{exp}}\right)$ from a closed-loop experiment,
2. Determine the control-relevant coprime factors $\{N_{0,z}, N_{0,y}, D_0\}$ of the plant as in (4.8),
3. Minimize the control-relevant identification criterion (4.9) over $\left\{\hat{N}_z, \hat{N}_y, \hat{D}\right\}$.

Note that for the inferential control structure, the closed-loop transfer function $\mathcal{F}_l\left(P_0, K^{\text{exp}}\right)$ has nine blocks, and thus also includes measurement data from z, that is not used for feedback.

The procedure is carried out in the discrete frequency domain, for two reasons. Identification of the model requires minimization of an $\mathcal{H}_\infty$-norm, which is relatively straightforward in the frequency domain, in contrast to the time domain. Furthermore, this allows for nonparametric validation, as discussed in Chapter 6.

The minimization of the control-relevant identification criterion Section 4.2 is performed using the reliable, well-conditioned algorithm in [34], which consists of Lawson's algorithm in conjunction with Sanathanan-Koerner [42] and Gauss-Newton iterations, to minimize (4.9) over the frequency grid. In this algorithm the coprime factors are parametrized as canonical right matrix fraction descriptions,

$$\begin{bmatrix} \hat{N}_z(\theta) \\ \hat{N}_y(\theta) \\ \hat{D}(\theta) \end{bmatrix} = \begin{bmatrix} C(\theta) \\ B(\theta) \\ A(\theta) \end{bmatrix} \left(\tilde{D}_e A(\theta) + \tilde{N}_{e,2} V_2^{-1} B(\theta)\right)^{-1},$$

where θ is a real-valued parameter vector. The optimal parameters are found by iteratively solving the following weighted nonlinear least squares problem

$$\theta^{\langle k \rangle} = \arg\min_{\theta} \sum_i w_i^{\langle k \rangle} \left\| \epsilon_i(\theta) \right\|_F^2, \tag{4.10}$$

using Sanathanan-Koerner iterations on a linear problem, such that a solution close to the optimum is found. The solution is then further refined, using Gauss-Newton iterations on the nonlinear problem. The weighting is determined using Lawson's algorithm,

$$w_i^{\langle k \rangle} = \frac{\bar{\sigma}\left(\epsilon_i\left(\theta^{\langle k \rangle}\right)\right) w_i^{\langle k-1 \rangle}}{\sum_i \left(\bar{\sigma}\left(\epsilon_i\left(\theta^{\langle k \rangle}\right)\right) w_i^{\langle k-1 \rangle}\right)}.$$

This type of weighting ensures the $\mathcal{H}_\infty$ minimization of the norm in (4.9), after convergence of the iteration. The next section will show the results for an experiment, carried out on the flexible beam setup.

4.5 Identification of the experimental setup

As can be seen in the triangle equation (4.3), during the fitting procedure the same weighting filters need to be used as for controller synthesis. This section discusses the choice of

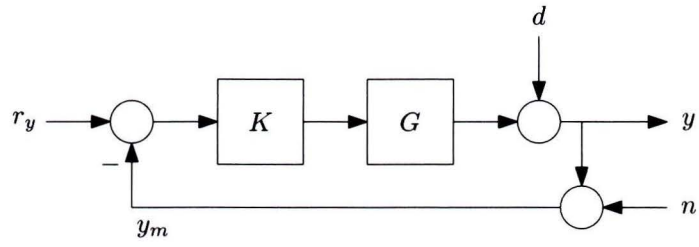

Figure 4.3: closed-loop control structure.

weighting filters for identification and controller design of the flexible beam experimental setup. First, weighting filters will be designed using $\mathcal{H}_\infty$ loop-shaping techniques. Then, the designed weighting filters are verified using the finite element model of 2.3, before the dynamics of the experimental setup are identified.

4.5.1 $\mathcal{H}_\infty$ loop-shaping

Loop-shaping is a method that is commonly used in control engineering, since it is a straightforward way to design a controller, that satisfies some common performances objectives and has sufficient robustness margins. This method is extended for $\mathcal{H}_\infty$-optimal control in [29], such that it can be used to design controllers for complex MIMO systems. Alternatively, the closed-loop transfer functions can be shaped, which is also common in optimal control, or signal-based approaches or numerical optimization can be used, see [45, Ch. 2]. An advantage of loop-shaping is that it allows specification of integrators and roll-off in a straightforward fashion.

Loop-shaping

Common objectives for motion control are adequate tracking of a reference signal, disturbance rejection, robustness against uncertainties and low noise transmission. These objectives can be expressed as requirements on the closed-loop transfer functions, which are related to the open-loop transfer functions. Therefore, by shaping the open-loop transfer functions, the performance objectives can be satisfied.

For the system in Figure 4.3, the error $e = r_y - y$ is given by

$$e = Sr_y - Sd + Tn, \tag{4.11}$$

where $S = (I + GK)^{-1}$ is the sensitivity, and $T = I - S$ is the complementary sensitivity. Note that in this control configuration, all outputs of G are used for feedback, i.e., performance output z is not included in this configuration.

Effective tracking and disturbance rejection, are obtained when $\|e\|_2$ is small compared to $\|r_y\|_2$ and $\|d\|_2$. Therefore, it is desirable that the maximum singular values of the sensitivity is small, i.e.,

$$\bar{\sigma}(S) \ll 1. \tag{4.12}$$

Similarly,

$$\bar{\sigma}(SG) \ll 1, \tag{4.13}$$

guarantees adequate rejection of disturbances on the plant input. These closed-loop objectives are achieved by shaping the open-loop transfer functions such that

$$\underline{\sigma}(GK) \gg 1 \text{ and } \underline{\sigma}(K) \gg 1. \tag{4.14}$$

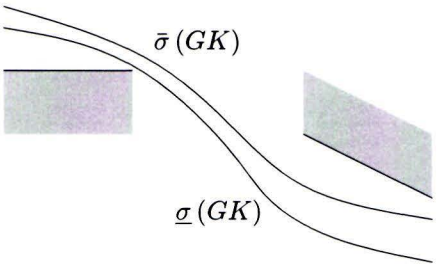

Figure 4.4: loop-shaping objectives.

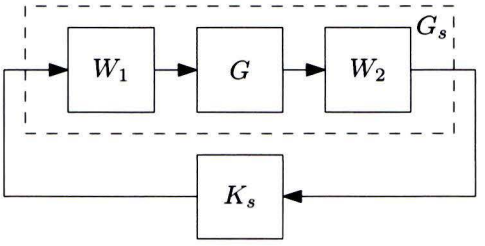

Figure 4.5: Shaped plant G_s.

In similar fashion, closed-loop and open-loop criteria, for robustness and low noise transmission are found. It is desirable that

$$\bar{\sigma}(KS) \ll 1, \tag{4.15}$$

because this guarantees robustness against additive uncertainties, and that

$$\bar{\sigma}(T) \ll 1 \tag{4.16}$$

for robustness against multiplicative uncertainties on the plant output, and low noise transmission. These closed-loop objectives are satisfied when

$$\bar{\sigma}(GK) \ll 1 \text{ and } \bar{\sigma}(K) \ll 1. \tag{4.17}$$

The conflicting requirements on the open-loop and controller gains in (4.14) and (4.17), clearly show the presence of a trade-off between performance and robustness. Generally, adequate tracking and disturbance rejection are selected as objectives in the low frequency region, while low noise transmission and robustness are selected at high frequencies. This is graphically shown in Figure 4.4.

Shaped plant

According to [29], the performance (4.14) and robustness (4.17) objectives of the loop-shaping method, can be included in the optimal control problem, by adding weighting filters W_1 and W_2 as shown in Figure 4.5. These weighting filters shape the singular values of

$$G_s = W_2 G W_1 \tag{4.18}$$

according to the loop-shaping method, such that the design requirements are met, i.e., $\sigma(G_s)$ is shaped instead of $\sigma(GK)$. Because W_1 and W_2 are weighting filters, they do not need to stabilize the plant, and therefore no information regarding the phase of G_s is needed. The

Gain margin:	11 dB at 184 Hz
Phase margin:	22.9 ° at 37.2 Hz
Modulus margin:	8.64 dB at 38 Hz

Table 4.1: Minimum stability margins for K^{exp}.

stability of the closed-loop system is left to the optimal controller synthesis. However, W_1 and W_2 need to be chosen such that G_s does not have any hidden unstable modes.

Once the optimal controller K_s for the shaped plant has been synthesized, it can be transformed back to the final controller $K = W_1 K_s W_2$. Since this does not change the actual loop in Figure 4.5, if K_s is a stabilizing controller for G_s, then G is stabilized by K. The advantage of this method, is that the control engineer has great insight and influence on the resulting controller, by specifying roll-off and integrating action in the weighting filters, i.e., the desired loop shape. If needed, it is still possible to extend the optimization problem with an uncertainty model, as discussed in Subsection 3.1.3, and synthesizing an suboptimal controller using the method in [10].

4.5.2 Weighting filter selection

The optimal control criterion (3.14) and control-relevant identification criterion in Section 4.2, depend on the dynamics of the model and plant, but also on the experimental controller K^{exp} and weighting filters. The design of the experimental controller and weighting filters will be discussed in this subsection.

First the experimental controller K^{exp} is designed, using standard loop-shaping techniques. Then, weighting filters W_1 and W_2 as in (4.18), are designed for $\mathcal{H}_\infty$ loop-shaping of the four-block problem (3.2). Then, this approach is extended to the inferential control configuration.

Experimental controller

As shown in (4.5), the identification criterion depends on the controller during the experiment, K^{exp}. This controller is designed by loop-shaping, using the frequency response function obtained from experiments on the setup. It was chosen to use a relatively low order controller, which does not contribute to a unnecessary high model order. The controller consists of a lead-lag compensator, integrator and high frequency roll-off, and is given by

$$K^{\text{exp}} = k \frac{1/(2\pi f_z)s + 1}{1/(2\pi f_p)s + 1} \frac{1}{1/(2\pi f_i)s + 1} \frac{1/(2\pi f_r)s + 1}{s}, \tag{4.19}$$

where

$$\begin{aligned} f_z &= 3.67\,\text{Hz}, \\ f_p &= 77\,\text{Hz}, \\ f_i &= 2.75\,\text{Hz}, \\ f_r &= 121\,\text{Hz}, \end{aligned}$$

and k is chosen such that a first cross-over frequency of 11 Hz is achieved. The resulting loop shape and sensitivity are shown in Figure 4.6, and in Table 4.1 the stability margins are shown.

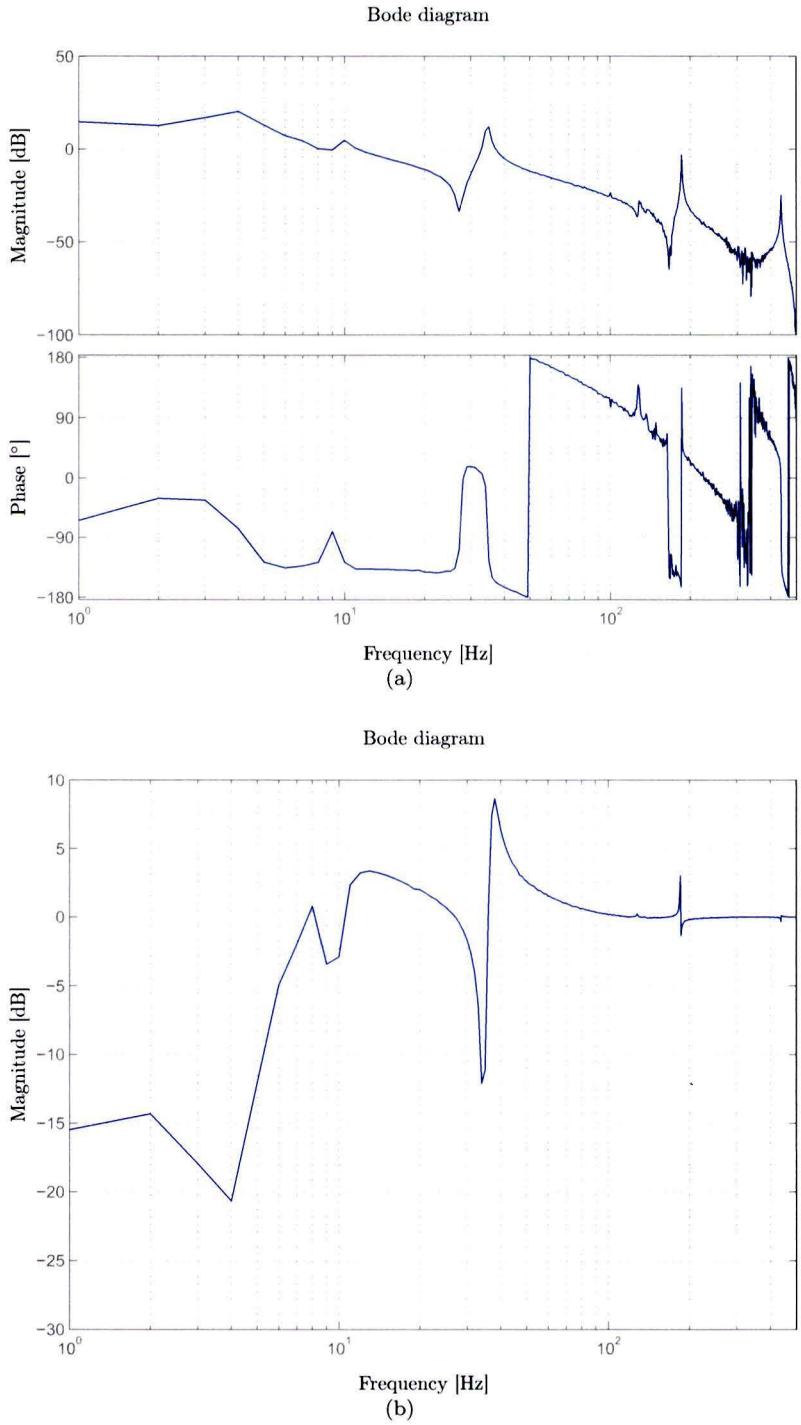

Figure 4.6: Designed loop shape (a) and sensitivity (b) for the frequency response function of G_y and experimental controller K^{exp}.

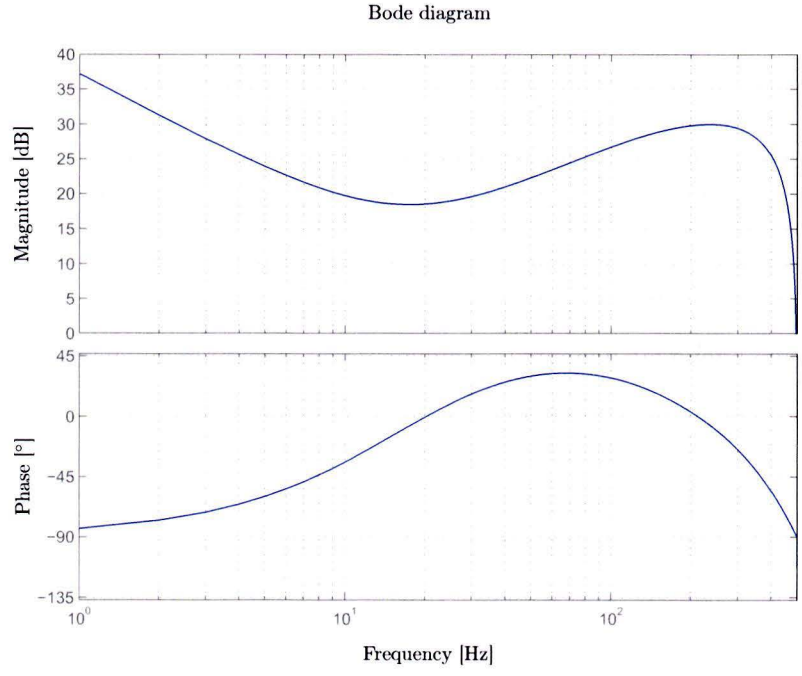

Figure 4.7: Fourth order weighting filter W_1, designed for $\mathcal{H}_\infty$ loop-shaping.

Weighting filters for the standard control structure

For optimal control of the four-block problem (3.2), $\mathcal{H}_\infty$ loop-shaping is applied. The weighting filters that form the shaped plant (4.18), are designed as follows.

The input weighting filter W_1 is designed similar to the experimental controller, and is given by (4.19), with parameters

$$\begin{aligned} f_z &= 20\,\text{Hz}, \\ f_p &= 180\,\text{Hz}, \\ f_i &= 15\,\text{Hz}, \\ f_r &= 480\,\text{Hz}, \end{aligned}$$

and a bandwidth of 60 Hz. The output weighting filter for G_y is $W_2 = 1$. This choice of weighting filters is possible because G_y is a SISO system, for complex MIMO systems the design of W_2 and W_1 generally is more cumbersome. Note that although the structure of W_1 is similar to K^{exp}, it is not a stabilizing controller. This weighting filter shapes the singular values of $W_2 G_y W_1$, and does not consider the phase of the open-loop transfer function, that is left to the controller synthesis algorithm. The bandwidth of 60 Hz is well beyond the first resonance of the setup at 35 Hz, which means that the flexible dynamics of the beam can be excited.

Weighting filters for the inferential control structure

The weighting filters for the inferential control structure, are based on the approach used for the four-block problem. Weighting filter W_1 remains identical, because the input of the plant has not changed, but W_2 becomes a diagonal weighting matrix, since the plant has

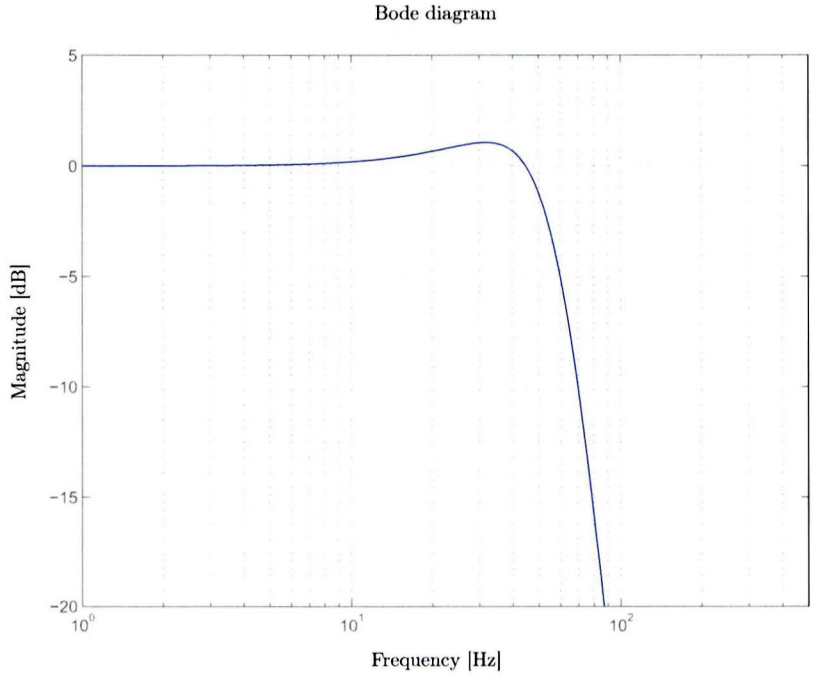

Figure 4.8: Reference filter T_r.

both y and z as output. Then, the shaped plant is

$$G_s = \begin{bmatrix} \alpha & 0 \\ 0 & 1 \end{bmatrix} \begin{bmatrix} G_z \\ G_y \end{bmatrix} W_1, \tag{4.20}$$

where α is a scaling factor that can be used to scale G_z, such that it is the same order of magnitude as G_y. For the flexible beam setup $\alpha = 1$ is a suitable choice, since G_z already is of comparable order of magnitude as G_y, as can be observed from the frequency response function in Figure 2.3.

The reference filter T_r is chosen as the desired closed-loop transfer function from r_z to z, such that the upper-left part of (3.13) is optimal when it is minimized. Below the desired bandwidth T_r is one, since this assures good tracking of the reference signal. Above 60 Hz it has a 6^{th} order roll-off, in order to minimize the influence of resonances at higher frequencies. The reference filter is given by

$$T_r = \frac{1}{\left({}^1\!/_{(2\pi f_b)^2} s^2 + {}^1\!/_{(2\pi f_b)} s + 1\right)^3},$$

where $f_b = 60\,\text{Hz}$, and is shown in Figure 4.8. When the plant is shaped as in (4.20), T_r should be multiplied by α.

The weighting filters W and V are appended to $\mathcal{F}_l(P, K)$ according to the identification criterion 4.5, and weigh the inputs and outputs of the closed-loop transfer functions. They are chosen in a similar way, as for the two degree of freedom controller design in [23], such that the upper-left or lower-right blocks can be emphasized. The used weighting is

$$W = \begin{bmatrix} \beta_2 & 0 & 0 \\ 0 & 1 & 0 \\ 0 & 0 & 1 \end{bmatrix} \text{ and } V = \begin{bmatrix} \beta_1 & 0 & 0 \\ 0 & 1 & 0 \\ 0 & 0 & 1 \end{bmatrix},$$

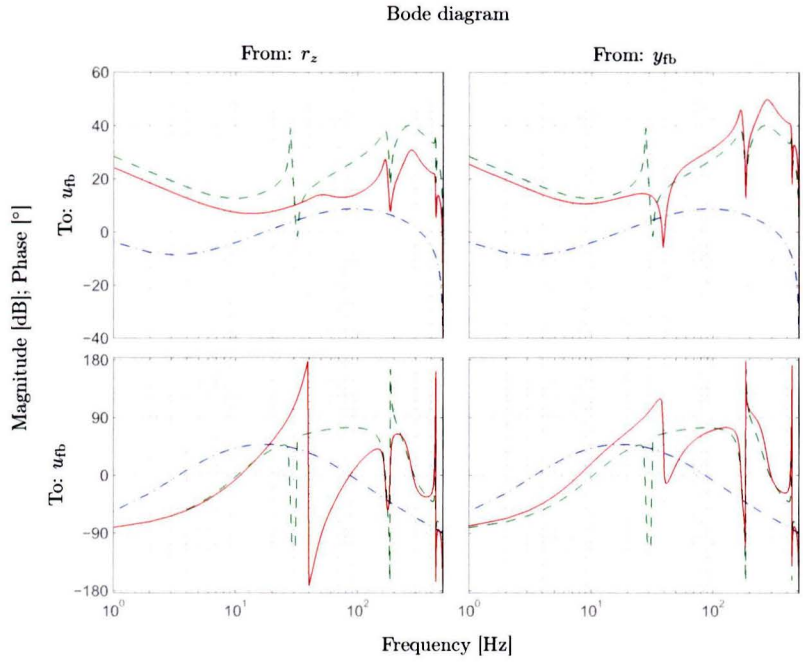

Figure 4.9: Experimental controller K^{exp} (blue $-\cdot$), standard optimal controller K_4^{NP} (green $--$) and optimal inferential controller K_9^{NP} (red $-$) for the first principles model.

with $\beta_1 = \beta_2 = 1.25$. This increases the influence of the upper-left block, which is the transfer function from r_z to z, i.e., it increases the importance of tracking in the optimization problem.

Controller synthesis simulation

In order to verify whether the selected weighting filters result in a satisfying controller design, prior to identifying a model of the dynamics of the plant, controller synthesis is simulated on the finite element model of Section 2.3. This step is optional, but is of great aid in rapidly selecting and testing weighting filters for the optimal controller synthesis algorithm. When the weighting filters are selected, the time consuming identification procedure only has to be performed once, i.e., with the selected weighting filters. The controller for the identified model is then assumed to be close to the controller based on the finite element model, i.e., an indication of the final result is available beforehand. Note once more that this step is not necessary to obtain satisfying results.

The optimal controllers for the finite element model of the flexible beam are shown in Figure 4.9. A clear difference between the standard optimal controller K_4^{NP}, and the optimal inferential controller K_9^{NP}, can be seen in the region around the first resonance of the system. The standard optimal controller has a large gain around 28 Hz, which improves the closed-loop transfer function for measured variable y, but causes also high gain in the transfer function from reference signal r_z to performance variable z, as is shown in Figure 4.10. This is the main cause of the large, lightly damped vibrations in z, that are present in the simulated step response of the closed-loop system in Figure 4.11. The optimal inferential controller has a much smaller gain in this frequency range, and therefore the performance of z is improved with inferential control, i.e., overshoot and settling time are substantially improved, while the performance of y is still acceptable.

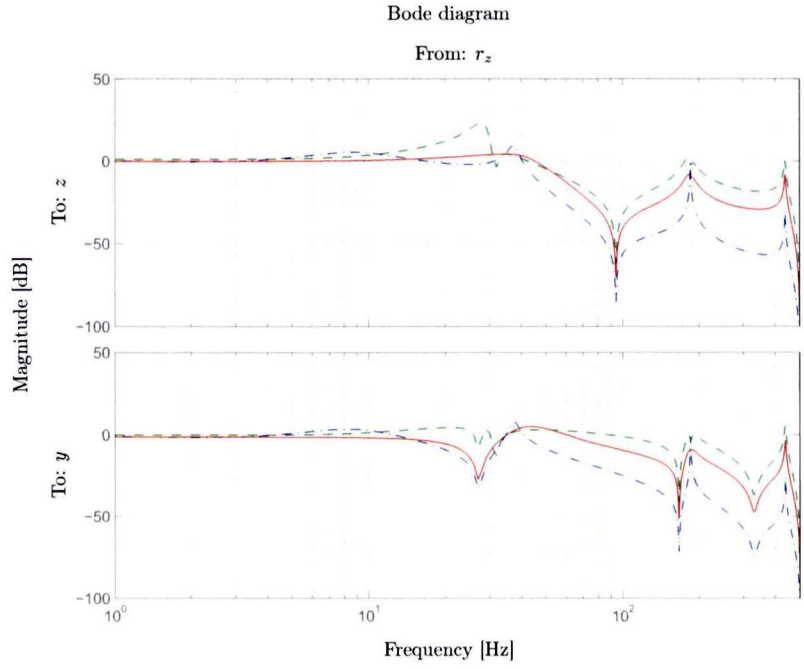

Figure 4.10: Closed-loop transfer functions of the finite element model with the controllers in Figure 4.9, K^{exp} (blue $-\cdot$), K_4^{NP} (green $--$) and K_9^{NP} (red $-$).

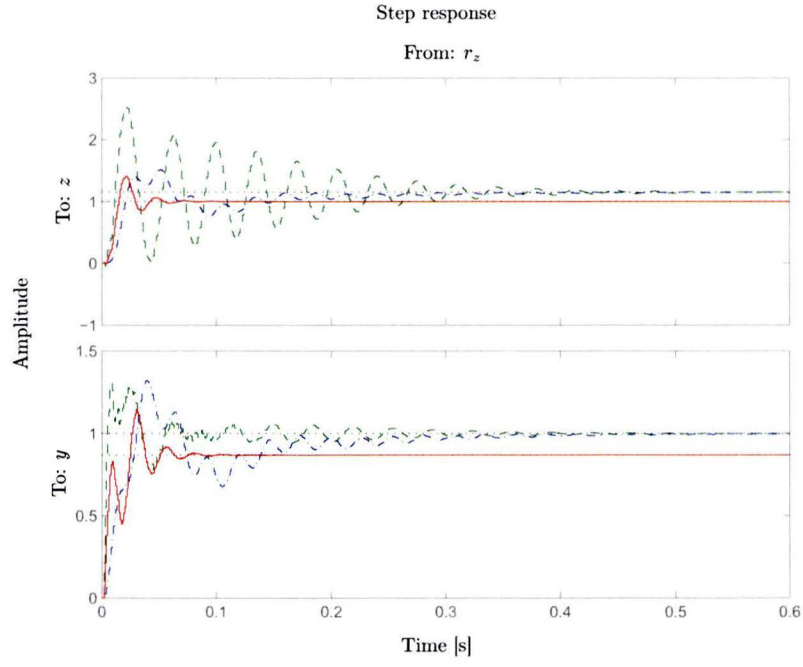

Figure 4.11: Simulated closed-loop step responses of the finite element model with the controllers in Figure 4.9, K^{exp} (blue $-\cdot$), K_4^{NP} (green $--$) and K_9^{NP} (red $-$).

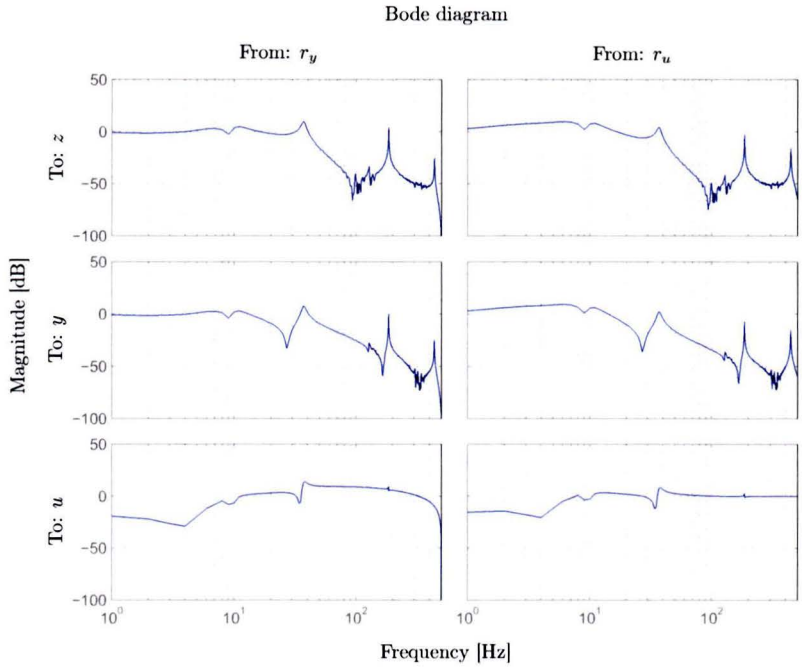

Figure 4.12: Closed-loop nonparametric identification of the experimental setup.

4.5.3 Experimental results on the flexible beam setup

In order to validate the proposed identification procedure, it is examined on the flexible beam experimental setup. First, a closed-loop nonparametric identification experiment is carried out, following the procedure described in Subsection 2.2.3. The obtained closed-loop frequency response function is shown in Figure 4.12. Note that input r_z is not shown in this figure, because the experimental controller K^{exp} is SISO. In the inferential control structure this implies $K_1 = K_2$, and thus the response of the system to r_z and r_y is identical, i.e., the first column can be duplicated. The frequency response function is used to determine the control-relevant coprime factorization of the plant (4.8), which is shown in Figure 4.13 (blue $-$).

This figure also shows a 9^{th} order fit model (green $--$). It can be clearly seen that the fit is relatively accurate at frequencies where the magnitude of the coprime factors is large. These are the control-relevant dynamics of the plant. On the other hand, in the low magnitude regions a relatively large bias appears, because the dynamics in these regions are less relevant for control.

This model is obtained by the iterative procedure described in Section 4.4, using 50 Lawson iterations. Figure 4.14 shows the convergence of (4.10). It can be seen that after an initial fast decrease, this criterion slowly converges to a constant value. Figure 4.15 shows the Lawson weighting w_i after 4, 5, 15, and 50 iterations. It can be seen that between 15 and 50 iterations the Lawson weighting does not change significantly.

Figure 4.16 shows the maximum singular values of the modeling error ϵ_i, after 4, 5, 15, and 50 iterations. Observe that the 11 points with the largest magnitude, are approximately of identical height. This is a result of the order of the model, which allows the identification algorithm to use 10 parameters to minimize the error. Consequently, the error cannot be reduced any further when 11 points are of equal magnitude, and the algorithm stops converging.

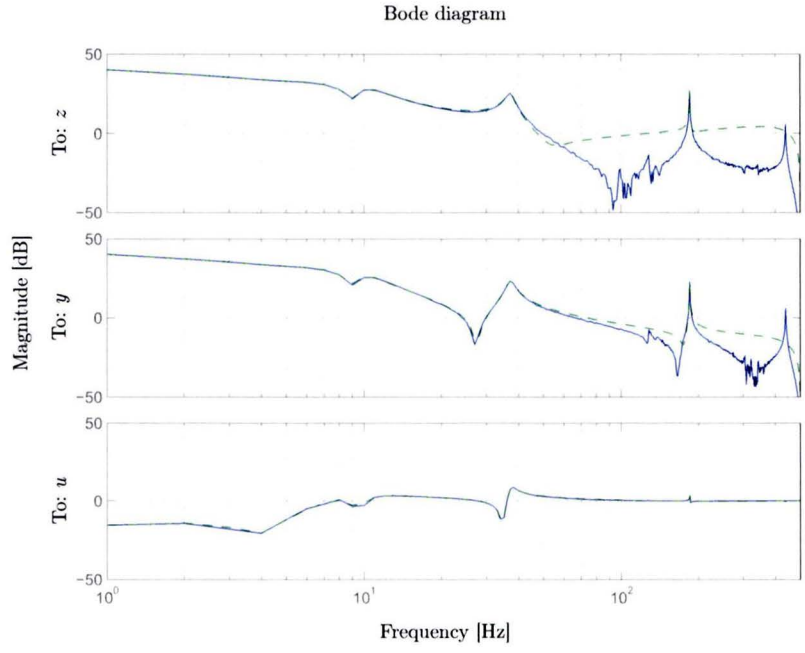

Figure 4.13: The control-relevant coprime factorization of the measurement data (blue $-$), and the identified model (green $--$).

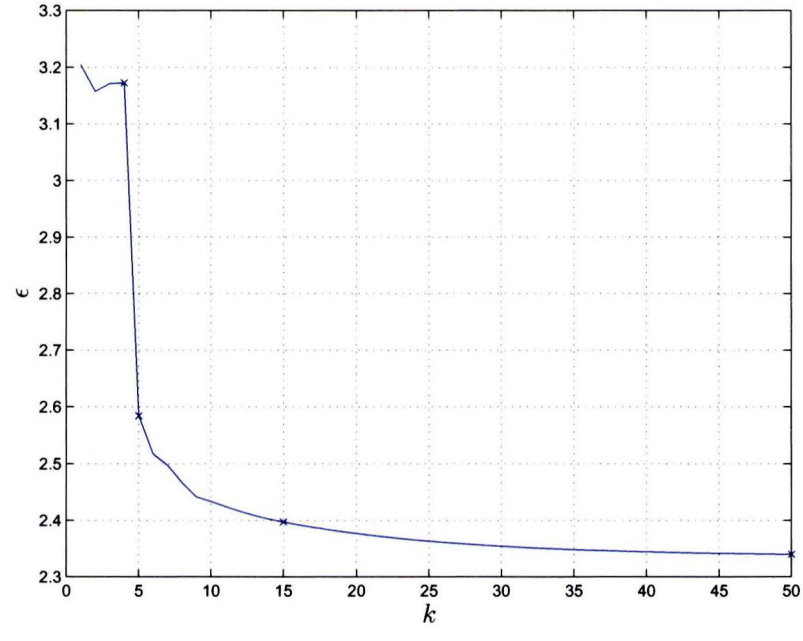

Figure 4.14: Convergence of the Lawson iterations.

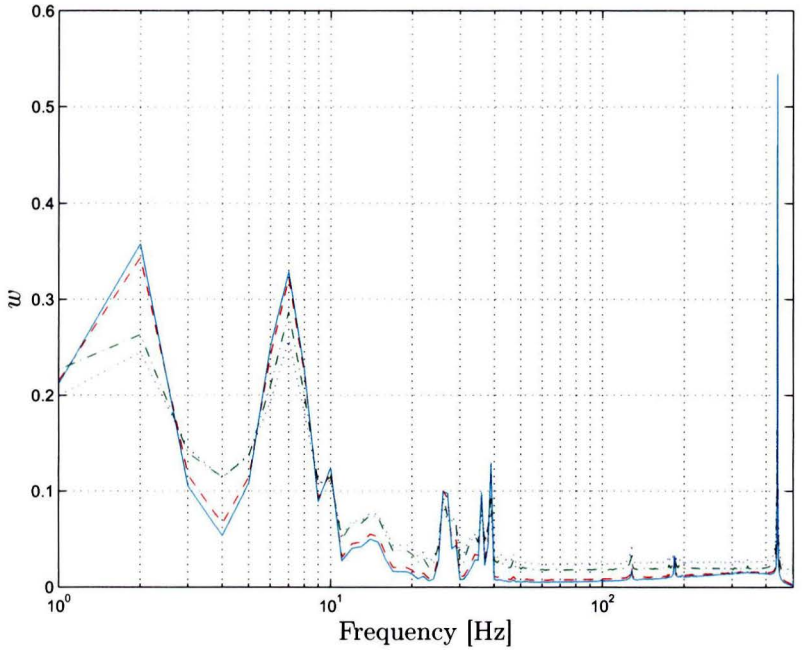

Figure 4.15: Lawson weighting w after 4 (blue $\cdots$), 5 (green $-\cdot$), 15 (red $--$), and 50 (cyan $-$) iterations.

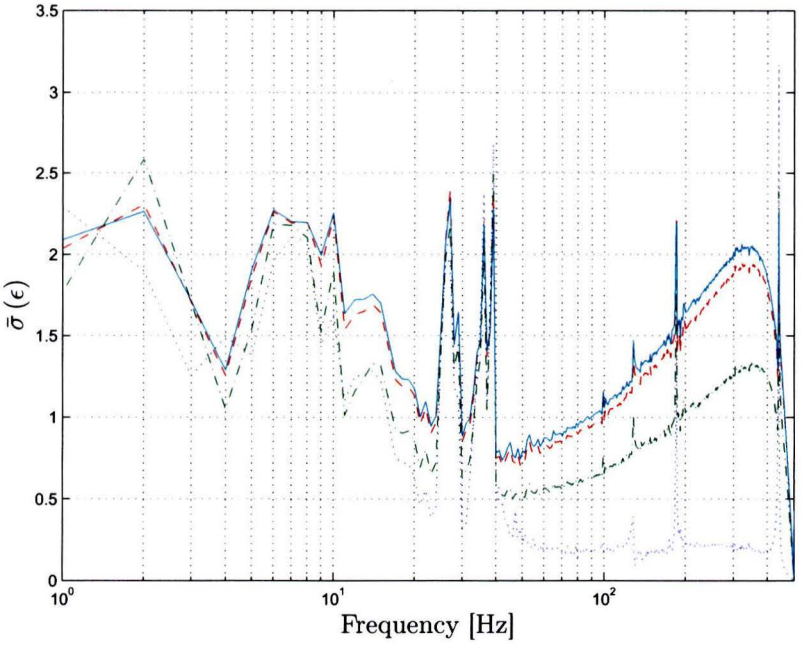

Figure 4.16: Maximum singular values of ϵ, after 4 (blue $\cdots$), 5 (green $-\cdot$), 15 (red $--$), and 50 (cyan $-$) iterations.

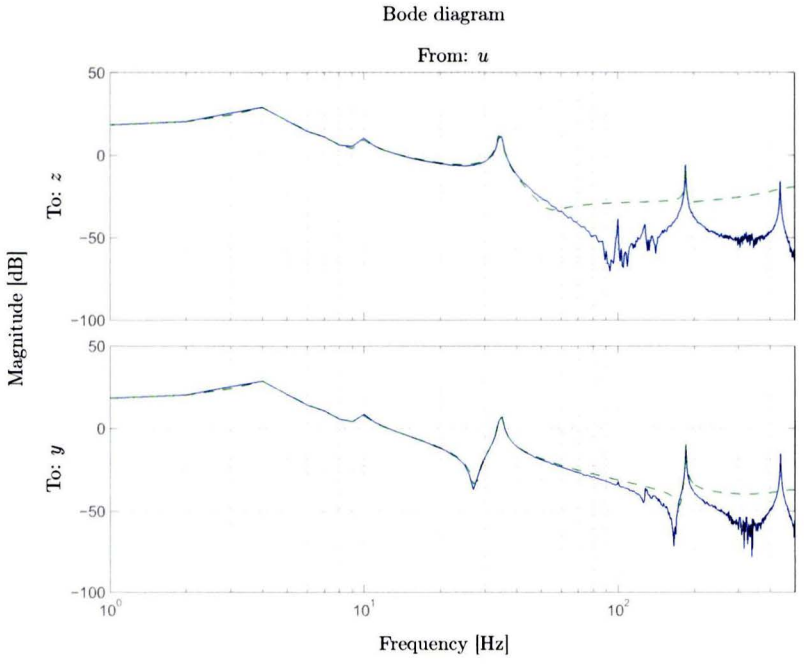

Figure 4.17: The frequency response function (blue $-$) and identified plant (green $--$).

Figure 4.17 shows the resulting control-relevant fitted plant. The dynamics below the desired bandwidth, as well as the resonances at 185 Hz and 430 Hz, are fitted accurately, which means that they have a large influence on the controller optimization criterion.

4.6 Conclusions

Optimal control, and especially optimal inferential control, relies on accurate modeling of the control-relevant dynamics. Therefore, in this chapter a control-relevant identification procedure has been proposed, and the following conclusions are drawn.

- An optimal control-relevant identification criterion for inferential control has been obtained. This is a direct consequence of the new inferential control structure, and the corresponding control objective.

- The control-relevant identification criterion for the inferential control structure, can be minimized using the numerically reliable algorithm in [34]. It is possible to obtain accurate models of systems in which the performance variables are not used for feedback. The algorithm requires data from the performance output of the plant, this implies that it has to be measured in the identification experiments.

- During the identification experiments it is possible to use a standard feedback controller, designed by rules of thumb commonly used by engineers. There is no need to use an initial inferential controller during the experiments.

- The theory is confirmed by experiments, resulting in an accurate model of the plant dynamics that can be used for synthesis of an optimal controller.

- The finite element model of the flexible beam is of great aid in designing weighting filters for the identification procedure and controller synthesis. However, it is not necessary to use such a model to obtain similar results.

It can be concluded that the proposed identification procedure can be successfully applied to structures with flexible dynamics, and that a model of the control-relevant dynamics can be obtained in this fashion. Since the purpose of a control-relevant model is subsequent optimal controller synthesis, this will be discussed in Chapter 5.

Chapter 5

Controller synthesis for nominal performance

In Chapter 3, an $\mathcal{H}_\infty$-optimal inferential control method for motion control of high-performance positioning systems with flexible dynamics, has been introduced. Because an accurate model of the plant is essential for model-based controller synthesis, in Chapter 4 a control-relevant identification procedure was proposed, and a model of the flexible beam experimental setup has been obtained using this procedure. The obtained model is relatively accurate in the frequency ranges that are relevant for (inferential) controller design, but relatively inaccurate in other frequency ranges.

The theoretical results of these chapters are promising, but need to be verified. Therefore, in this chapter the theory is confronted with a true system, the flexible beam experimental setup. First, in Section 5.1 standard and inferential controllers are synthesized using the control-relevant model. By inspecting the optimized values of the control criteria, inferential control is compared to standard optimal control.

Then, in Section 5.2 simulations of the closed-loop behavior of the control-relevant model are compared to the response of the true system. If the response of the model closely approaches the true system behavior, this indicates that the control-relevant dynamics have been modeled accurately. Furthermore, these experiments will confirm the improved performance of the inferential control configuration. Finally, in Section 5.3 the conclusions of this chapter are presented.

5.1 Controller synthesis

With the obtained control-relevant model, optimal controllers are synthesized for the four-block problem (3.2) and nine-block problem (3.13). Figure 5.1 shows the obtained standard optimal and optimal inferential controllers, along with the experimental controller. Observe that these controllers are very similar to the controllers that have been obtained for the first principles model, in Figure 4.9. Especially in the frequency ranges between the poles of the plant, i.e., between 35 Hz and 185 Hz and between 185 Hz and 430 Hz, the controller gains are smaller. This is connected to the magnitude of the control-relevant model in these frequency ranges, that is larger than for the first principles model.

Table 5.1 shows the obtained values for the various performance criteria. From these values some conclusions can be drawn:

- The values for the experimental controller K^{exp} are significantly larger than for the optimal controllers K_4^{NP} and K_9^{NP}. This indicates that the experimental controller

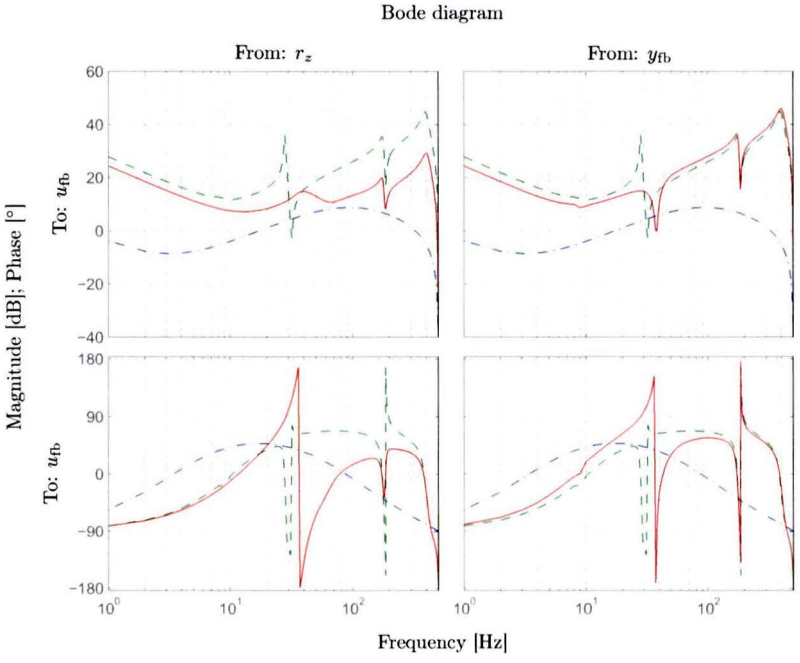

Figure 5.1: Experimental controller K^{exp} $(-\cdot)$, standard optimal controller K_4^{NP} $(--)$, and optimal inferential controller K_9^{NP} $(-)$.

$\mathcal{J}(P,K)$	P_4^{CR}	P_9^{CR}
K^{exp}	123.01	196.82
K_4^{NP}	3.12	32.44
K_9^{NP}	-	7.80

Table 5.1: Obtained values of the performance criteria for the controllers shown in 5.1, evaluated for the control-relevant four-block P_4^{CR} and inferential block structure P_9^{CR}.

has a low performance compared to the $\mathcal{H}_\infty$-optimal controllers. For the control-relevant identification procedure, it is desirable that the performance of K^{exp} is close the performance of the optimal controllers. Therefore, the results may be improved by iterating identification and controller synthesis, as discussed in [44].

- The performance criterion for the optimal inferential controller $\mathcal{J}\left(P_9^{\text{CR}}, K_9^{\text{NP}}\right)$, is 4.16 times smaller than $\mathcal{J}\left(P_9^{\text{CR}}, K_4^{\text{NP}}\right)$ for the standard optimal controller. This indicates a significant increase in performance using inferential control.
- From the same criteria, it follows that the standard optimal controller K_4^{NP} is not optimal for the inferential control configuration. Therefore, it can be concluded that the four-block problem (3.2) is not sufficient to design controllers for systems with flexible dynamics.

In Figure 5.2 the closed-loop transfer functions from reference r_z to outputs z and y, are shown for , K^{exp} (blue $-\cdot$), K_4^{NP} (green $--$) and K_9^{NP} (red $-$). Although a common measure for the performance of a system is the bandwidth of the control loop, this figure shows that for flexible structures this is not necessarily true. From the closed-loop transfer function from r_z to y, it can be observed that the optimal four-block controller (green $--$) has a bandwidth of approximately 25 Hz, but for output z this controller causes a peak value

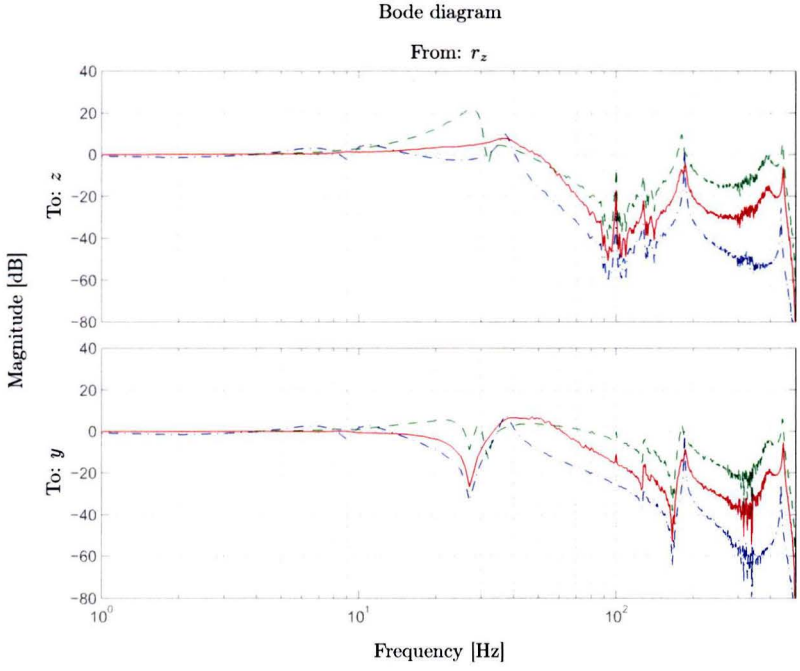

Figure 5.2: closed-loop transfer functions, corresponding to the controllers in Figure 5.1, K^{exp} (blue $-\cdot$), K_4^{NP} (green $--$) and K_9^{NP} (red $-$).

of more than 20 dB in the closed-loop transfer function, which decreases the performance of the system significantly. Furthermore, beyond the bandwidth frequency the magnitude of the closed-loop transfer function is relatively large around the poles of the plant, which indicates high noise transmission at these frequencies.

Figure 5.2 also shows that for the optimal inferential controller (red $-$) the closed-loop transfer function for output z is substantially improved. The magnitude is larger than 0 dB for frequencies up to approximately 44 Hz, but in contrast to the result of the standard optimal controller it is relatively flat. However, based on the transfer function from r_z to y, one might conclude that this system has a much lower bandwidth.

5.2 Confirming theory with experiments

In Section 5.1, optimal controllers have been synthesized using the model of the flexible beam setup, that was obtained by means of control-relevant identification in Chapter 4. One controller is synthesized using standard control techniques, and considers only the measured variable, the second controller is synthesized using the inferential control configuration that includes the performance variable in the problem. These controllers are used to confirm the new control theory by means of simulations and experiments, as follows.

Simulations and experiments on the flexible beam will be performed using the representative scenario sketched in Section 1.4. The design of the experiments is shown in Figure 5.3. The beam is actuated with input u near both ends of the beam. At the same locations, the displacement of the beam is measured, and these two measurements are averaged to calculate the displacement of the point y, which is used as feedback variable to control the displacement of the center of the beam. This approach assumes that the beam is rigid, i.e., the beam does not bend. The real displacement in the center of the beam is given by

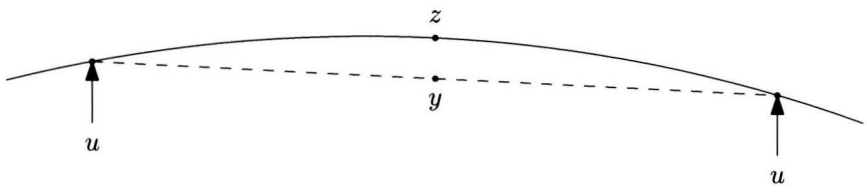

Figure 5.3: Design of experiments on the flexible beam setup. The beam is actuated with input u near both ends of the beam. The position of measured variable y is used for feedback control, and performance variable z is recorded to confirm the new control theory.

the performance variable z. Generally, the displacement in the center of the beam is not equal to the measured displacement, i.e., $z \neq y$. During the experiments the closed-loop step response of the measured variable y and performance variable z are both recorded to confirm the improved performance of the new inferential control configuration.

First, simulations are performed using the control-relevant model from Subsection 4.5.3. The simulations give an indication of the improved performance of the new inferential control configuration, compared to the standard control theory. Figure 5.4 shows the simulated closed-loop step response, of the experimental controller K^{exp} (blue $-\cdot$), the standard optimal controller K_4^{NP} (green $--$) and the optimal inferential controller K_9^{NP} (red $-$), on the control-relevant model. The performance of K_9^{NP} shows substantial improvement compared to K_4^{NP}, as also is indicated by the values for the performance criteria in Table 5.1.

The standard optimal controller K_4^{NP} (green $--$) excites the flexible dynamics of the beam, causing lightly damped vibrations in the structure. These vibrations can be observed in the response of the performance variable z, which is obviously undesirable. The optimal inferential controller K_9^{NP} (red $-$) shows a remarkable improvement on this point, the vibrations have a substantially smaller maximum amplitude and are more damped. This results in less overshoot and a faster settling time for the performance variable z.

The measured output y also seems to benefit from the reduced internal vibrations of the structure. The initial response to the step is slower, but it remains faster than the experimental controller. The overshoot is of similar magnitude as for the other two controllers, and the settling time improves. It can be concluded that the new control theory is improves the performance on the model substantially.

Next, a similar experiment is performed on the experimental flexible beam setup. Figure 5.5 shows the implementation of the experimental controller K^{exp} (blue $-\cdot$), the standard optimal controller K_4^{NP} (green $--$) and the optimal inferential controller K_9^{NP} (red $-$) on the experimental setup. The reference signal r_z makes a step of 0.05 mm after 0.1 s. If this figure is compared to Figure 5.4, it is obvious that the response of the true plant is exceptionally close to the simulations, and thus the following two conclusions can be drawn:

- The closed-loop step responses of the control-relevant model, and experimental setup show similar results. This is a strong indication that the control-relevant model contains the dynamics of the plant that dominate the closed-loop behavior of the setup, i.e., the plant dynamics have been identified successfully.

- The new inferential controller design is implemented on the true system and improves the performance substantially. Hence, the new control theory is confirmed by experimental results.

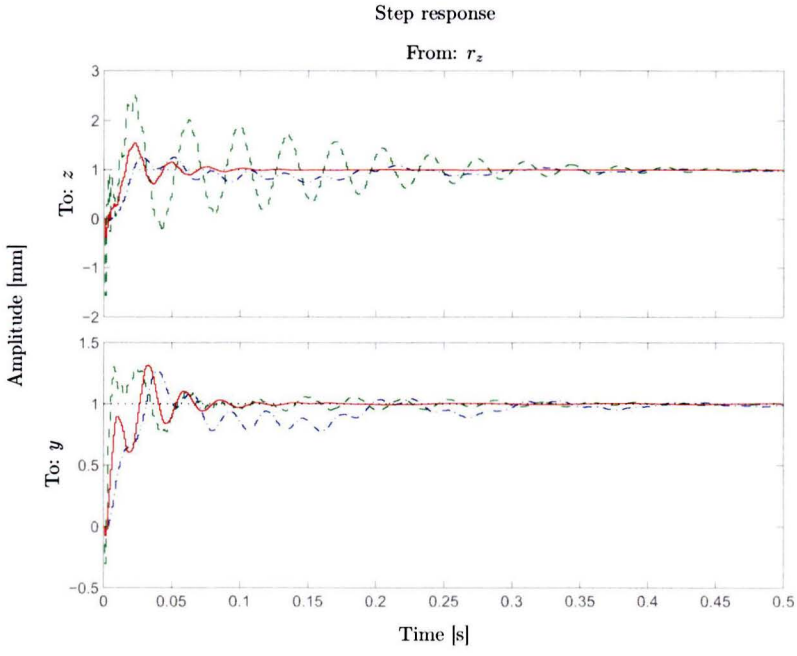

Figure 5.4: Simulated closed-loop step responses, corresponding to the controllers in Figure 5.1, K^{exp} (blue $-\cdot$), K_4^{NP} (green $--$) and K_9^{NP} (red $-$).

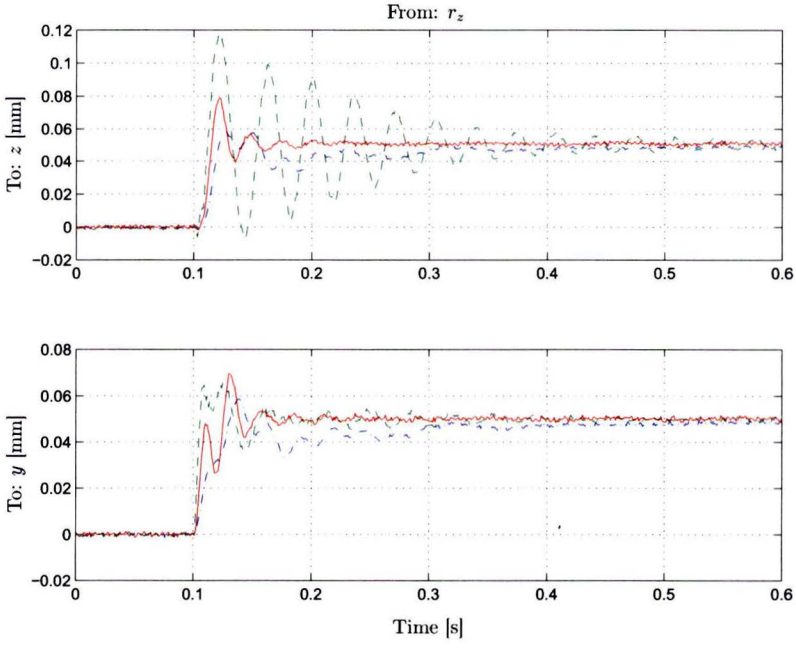

Figure 5.5: closed-loop step responses, obtained by implementing the controllers in Figure 5.1, K^{exp} (blue $-\cdot$), K_4^{NP} (green $--$) and K_9^{NP} (red $-$), on the flexible beam experimental setup.

5.3 Conclusions

The results that have been shown in this chapter, are promising for control of the next-generation lightweight wafer stages with flexible dynamics. The following conclusions are drawn.

- A proof of principle is delivered for the inferential control configuration, and the performance is improved substantially compared to standard optimal control.
- There is a strong indication that the dynamics of the experimental setup are identified accurately, i.e., the control-relevant identification procedure has been applied successfully to a structure with flexible dynamics.

The control-relevant model that was obtained in Subsection 4.5.3, has been used synthesize controllers achieving nominal performance on the model. These controllers have been successfully applied to the experimental setup, but in general this cannot be guaranteed. Because of differences in the dynamics of the true plant and identified model, internal stability on the experimental setup is not necessarily provided.

By addressing these differences in an uncertainty model, the step towards robust stabilization of the plant can be taken. In Chapter 6, a model validation procedure is proposed, in which the model errors are addressed such that robust controllers that provide internal stability for the true plant, can be synthesized.

Chapter 6

Model validation for robust control

In Chapter 4, it was shown how a control-relevant model can be identified. Although the difference between the model and measurement data is minimized in this procedure, it is inevitably that modeling errors are present. Furthermore, the experimental data contains noise and disturbances.

In order to confirm that the model accurately describes the dynamics of the plant, it needs to be validated by comparison to measurement data. Common validation methods attribute modeling errors completely to disturbances or noise, and consequently models with systematical errors are invalidated [27]. However, these validation methods solely consider the nominal model. Robust control is able to deal with model sets, and can be used to address systematical model errors, such that the true plant dynamics are encompassed by the model set. This motivates a different approach towards model validation for robust control.

For models with a given uncertainty model, (in)validation methods can be found in literature, see e.g. [41, 46]. In order to obtain a meaningful validation problem, such an uncertainty model should be chosen with care. The model error consists of systematical errors, noise and disturbances. Systematical errors influence the stability properties of the model, and should therefore be encompassed by the model set. However, noise and disturbance can not influence stability and should be treated differently, and it is therefore essential that they are correctly separated from the systematical errors.

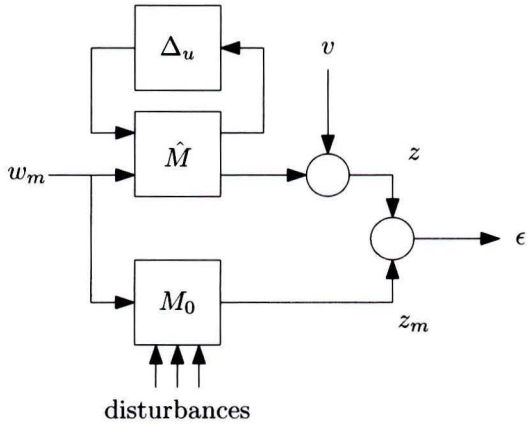

Figure 6.1: Structure of the model validation problem.

The model validation method that is proposed in [33] makes a suitable trade-off for the contributions of systematical errors, noise and disturbances to the model error, as follows. It compares the plant and the model in a structure as shown in Figure 6.1. In this figure, $\hat{M}$ is the nominal model with a perturbation Δ_u and a noise term v. The model is compared with the plant M_0, which has the same input as the model and additionally some external disturbances. The model is not invalidated if there exists a model in the model set that produces the same data as the plant, i.e., there exists $\|\Delta_u\|_\infty < \gamma_u$ such that $\epsilon = 0$. The key problem is to separate the true plant dynamics in the output of M_0, from noise and disturbances. The solution lies in the use of periodic excitation signals. The repetitive part of the output can then be contributed to the system dynamics, while variation over the periods is caused by noise and disturbances. Therefore, the steps in the model validation procedure are:

1. Estimate a disturbance model from measurement data,
2. Determine the smallest perturbation that validates the model,
3. Design an overbound for the perturbation to obtain a parametric uncertainty model.

This procedure relies on the underlying structure of $\hat{M}$, that is used to parametrize the perturbations. In Section 4.1, it was already motivated that coprime factorizations should be used, this is discussed in more detail in Section 6.1. In Section 6.2, the model validation procedure is explained in more detail, regarding the disturbance model and parametrization of the uncertainty model. The theory in these two sections is mainly based on the work of Oomen [33]. In Section 6.3, the theory is confronted with a true system, i.e., the flexible beam experimental setup. The chapter ends with some conclusions in Section 6.4.

6.1 Dual-Youla parametrization

The parametrization of the uncertainty model is essential in the model validation procedure. In order to be able to validate a model, it is required that the plant dynamics are encompassed by the model set, otherwise it is impossible to match the experimental data. Therefore, the dual-Youla parametrization is used.

Definition 6.1 (Dual-Youla parametrization)**.** The dual-Youla parametrization for the four-block problem (3.2) is given by

$$\mathcal{G} = \left\{ G = \left(\hat{N} + D_k \Delta_u\right)\left(\hat{D} - N_k \Delta_u\right)^{-1} \middle| \Delta_u \in \mathcal{RH}_\infty \right\}, \tag{6.1}$$

where $\left\{\hat{N}, \hat{D}\right\}$ is a right coprime factorization of $\hat{G}$, and $\{N_k, D_k\}$ is a RCF of K.

The dual-Youla parametrization is graphically shown in the block scheme in Figure 6.2. The parametrization has the following property: *Given that K stabilizes $\hat{G}$, all models stabilized by K are given by $\mathcal{G}$.* This property has two important consequences:

1. The true system is encompassed by the model set, i.e., $G_0 \in \mathcal{G}$,
2. All models G in model set $\mathcal{G}$ are stabilized by K.

This parametrization plays a key role in the model validation procedure, since it provides the necessary conditions for validation of the control-relevant model.

In order to explain the special properties of the dual-Youla parametrization, first in Subsection 6.1.1 the control interpretation of the Bézout identity will be discussed, then in

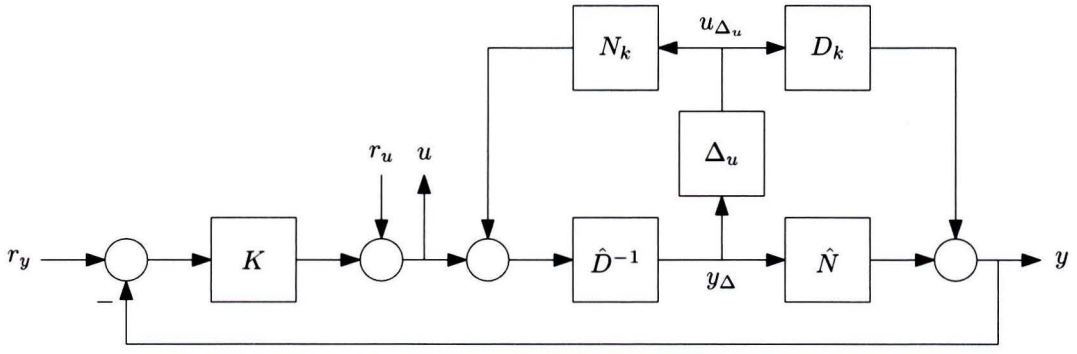

Figure 6.2: Dual-Youla parametrization for the standard four-block problem.

Subsection 6.1.2 the stability property of the dual-Youla parametrization is discussed. It should be noted that feedback from all outputs of the plant is assumed, and therefore below the parametrization of the four-block problem (3.2) will be discussed, i.e., G should be read as G_y and K as K_2. Since internal stability of the four-block problem is sufficient for internal stability of the inferential control configuration (3.13), this still gives valuable results. In Subsection 6.1.3 the uncertainty structure will be extended to include perturbations on z, i.e., a dual-Youla parametrization for the inferential control structure is given.

6.1.1 Control interpretation of the Bézout identity

It can be shown that the Bézout identity has an important interpretation in control theory. Consider a plant G with RCF $\{N, D\}$, and controller K with LCF $\left\{\tilde{N}_k, \tilde{D}_k\right\}$. Then, it can be shown that internal stability can be evaluated by a Bézout identity as follows [48].

The closed-loop transfer function is

$$T(G,K) = \begin{bmatrix} G \\ I \end{bmatrix} (I + KG)^{-1} \begin{bmatrix} K & I \end{bmatrix}, \tag{6.2}$$

and by substituting the coprime factorizations this becomes

$$T(G,K) = \begin{bmatrix} N \\ D \end{bmatrix} \left(\tilde{D}_k D + \tilde{N}_k N\right)^{-1} \begin{bmatrix} \tilde{N}_k & \tilde{D}_k \end{bmatrix}. \tag{6.3}$$

The coprime factors are stable by definition, and therefore

$$T(G,K) \in \mathcal{RH}_\infty \iff \left(\tilde{D}_k D + \tilde{N}_k N\right)^{-1} \in \mathcal{RH}_\infty. \tag{6.4}$$

By defining a second right coprime factorization of the plant, $G = N_z D_z^{-1} = (NZ)(DZ)^{-1}$ with $Z = \left(\tilde{D}_k D + \tilde{N}_k N\right)^{-1}$, it can be shown that $\tilde{D}_k D_z + \tilde{N}_k N_z$ satisfies the Bézout identity as follows. Note that Z must be stable in the definition of the coprime factors, and thus $T(G,K) \in \mathcal{RH}_\infty$.

$$\left(\tilde{D}_k D_z + \tilde{N}_k N_z\right)^{-1} = \left(\tilde{D}_k DZ + \tilde{N}_k NZ\right)^{-1} \tag{6.5}$$

$$= Z^{-1}\left(\tilde{D}_k D + \tilde{N}_k N\right)^{-1} \tag{6.6}$$

$$= I. \tag{6.7}$$

And therefore,

$$T(G,K) \in \mathcal{RH}_\infty \iff \tilde{D}_k D_z + \tilde{N}_k N_z = I. \tag{6.8}$$

This means that for any RCF of G, and LCF of K, a Bézout identity is satisfied if and only if the closed-loop system is internally stable. Similarly, this can be shown for a LCF of the plant, and RCF of the controller.

6.1.2 Stability properties of the model set

The favorable properties of the dual-Youla parametrization are combined in the following theorem, which is dual to [50, Thm. 12.17] in the sense that controller K and plant G have been exchanged, such as in [48].

Theorem 6.1 (dual-Youla). *Let $K = N_k D_k^{-1} = \tilde{D}_k^{-1}\tilde{N}_k$ be RCF and LCF of K over $\mathcal{RH}_\infty$, and let $\hat{G} = \hat{N}\hat{D}^{-1} = \tilde{\hat{D}}^{-1}\tilde{\hat{N}}$ be RCF and LCF of $\hat{G}$ over $\mathcal{RH}_\infty$. Then, the set of all proper plants that are internally stabilized by K, are parametrized by*

$$G = \left(\hat{N} + D_k\Delta_u\right)\left(\hat{D} + N_k\Delta_u\right)^{-1},\ \Delta_u \in \mathcal{RH}_\infty, \tag{6.9}$$

or

$$G = \left(\tilde{\hat{D}} + \Delta_l\tilde{N}_k\right)^{-1}\left(\tilde{\hat{N}} + \Delta_l\tilde{D}_k\right),\ \Delta_l \in \mathcal{RH}_\infty, \tag{6.10}$$

such that

$$Z = \left(\tilde{D}_k D + \tilde{N}_k N\right)^{-1} \in \mathcal{RH}_\infty. \tag{6.11}$$

Using the parametrization (6.9), it can be shown that the corresponding Bézout identity is satisfied for any $\Delta_u \in \mathcal{RH}_\infty$, as follows:

$$\begin{aligned}
\tilde{D}_k D - \tilde{N}_k N &= \tilde{D}_k\left(\hat{D} + N_k\Delta_u\right) - \tilde{N}_k\left(\hat{N} + D_k\Delta_u\right) && (6.12)\\
&= \tilde{D}_k\hat{D} - \tilde{N}_k\hat{N} + \left(\tilde{D}_k N_k - \tilde{N}_k D_k\right)\Delta_u && (6.13)\\
&= I.
\end{aligned}$$

This proves that if the nominal model $\hat{G}$ is internally stabilized by K, then all plants G in the model set are also internally stabilized by K.

The converse is also true, this can be shown as follows. Suppose a proper plant G is stabilized by controller K, i.e., $Z = \left(\tilde{D}_k D + \tilde{N}_k N\right)^{-1} \in \mathcal{RH}_\infty$, and define the perturbation Δ_u by

$$\begin{aligned}
\hat{N} + D_k\Delta_u &= NZ, && (6.14)\\
\Delta_u &= D_k^{-1}\left(NZ - \hat{N}\right). && (6.15)
\end{aligned}$$

Then

$$\begin{aligned}
\hat{D} + N_k\Delta_u &= \hat{D} + N_k D_k^{-1}\left(NZ - \hat{N}\right) && (6.16)\\
&= \hat{D} + \tilde{D}_k^{-1}\tilde{N}_k\left(NZ - \hat{N}\right) && (6.17)\\
&= \tilde{D}_k^{-1}\left(\tilde{D}_k\hat{D} - \tilde{N}_k\hat{N} + \tilde{N}_k NZ\right). && (6.18)
\end{aligned}$$

If the Bézout identity is satisfied for the RCF of $\hat{G}$, this is equal to

$$\begin{aligned}
\hat{D} + N_k \Delta_u &= \tilde{D}_k^{-1} \left(I + \tilde{N}_k N Z \right) && (6.19)\\
&= \tilde{D}_k^{-1} \left(Z^{-1} + \tilde{N}_k N \right) Z && (6.20)\\
&= \tilde{D}_k^{-1} \tilde{D}_k D Z && (6.21)\\
&= DZ. && (6.22)
\end{aligned}$$

By using that $D_k \Delta_u \in \mathcal{RH}_\infty$ by definition (6.14), and $N_k \Delta_u \in \mathcal{RH}_\infty$ which follows from (6.22), together with the Bézout identity that is satisfied for the LCF of $\hat{G}$, it follows that

$$\begin{aligned}
I &= \tilde{\hat{D}} D_k - \tilde{\hat{N}} N_k && (6.23)\\
\Delta_u &= \tilde{\hat{D}} \left(D_k \Delta_u \right) - \tilde{\hat{N}} \left(N_k \Delta_u \right) \in \mathcal{RH}_\infty. && (6.24)
\end{aligned}$$

This means that if $\hat{G}$ is internally stabilized by a controller K, then all stabilized plants are parametrized by (6.9). With this important result it is shown that $G_{0,y}$ can be parametrized as part of the model set. However, the performance output of the plant is not taken into account yet. The next subsection explains how G_z can be included in the parametrization.

6.1.3 Uncertainty in the inferential control structure

In order to ensure that $G_{0,z}$ can be parametrized by the model set, a second Δ-block is introduced. The structure of the dual-Youla parametrization for inferential control, is shown in Figure 6.3, where the four-block problem (gray) is extended (black) with the inferential part of the controller K_1, the performance output of the plant $\hat{N}_z$, and the second perturbation Δ_z. The parametrization of the plant then becomes

$$\mathcal{G} = \left\{ \begin{bmatrix} G_z \\ G_y \end{bmatrix} = \begin{bmatrix} \hat{N}_z + \Delta_z \\ \hat{N}_y + D_k \Delta_u \end{bmatrix} \left(\hat{D} - N_k \Delta_u \right)^{-1} \middle| \Delta_u, \Delta_z \in \mathcal{RH}_\infty \right\}. \tag{6.25}$$

It can be observed that, provided that $K_1, \Delta_z \in \mathcal{RH}_\infty$, the uncertain plant is still internally stabilized by K_2. The block scheme in Figure 6.3 can be rearranged to form an $\hat{M}\Delta$-structure as in the validation setup in Figure 6.1. After addition of the weights that were used in the identification procedure, $\hat{M}$ with input $w_m = \left[\begin{array}{cc|ccc} u_{\Delta_z} & u_{\Delta_u} & r_3 & r_2 & r_1 \end{array} \right]^T$ and output $z = \left[\begin{array}{cc|ccc} y_\Delta & y_\Delta & z & y & u \end{array} \right]^T$, is then given by

$$\hat{M} = \left[\begin{array}{cc|c} 0 & 0 & \left(\hat{D} + K_2 \hat{N}_y \right)^{-1} \begin{bmatrix} K_1 & K_2 & I \end{bmatrix} V \\ 0 & 0 & \left(\hat{D} + K_2 \hat{N}_y \right)^{-1} \begin{bmatrix} K_1 & K_2 & I \end{bmatrix} V \\ \hline W_e & 0 & \\ 0 & W_y D_k & W \begin{bmatrix} \hat{G}_z \\ \hat{G}_y \\ I \end{bmatrix} \left(I + K_2 \hat{G}_y \right)^{-1} \begin{bmatrix} K_1 & K_2 & I \end{bmatrix} V \\ 0 & -W_u N_k & \end{array} \right]. \tag{6.26}$$

The Δ-block that matches $\hat{M}$ has a block diagonal structure

$$\Delta = \begin{bmatrix} \Delta_z & \\ & \Delta_u \end{bmatrix}. \tag{6.27}$$

Note that it is also possible to make the Δ-block 2×1, since the first two rows of $\hat{M}$ are identical. Here is chosen not to do so, because in the diagonal structure Δ_z and Δ_u can be identified separately. Note also that in contrast to G_z in (6.25) does depend on Δ_u. The

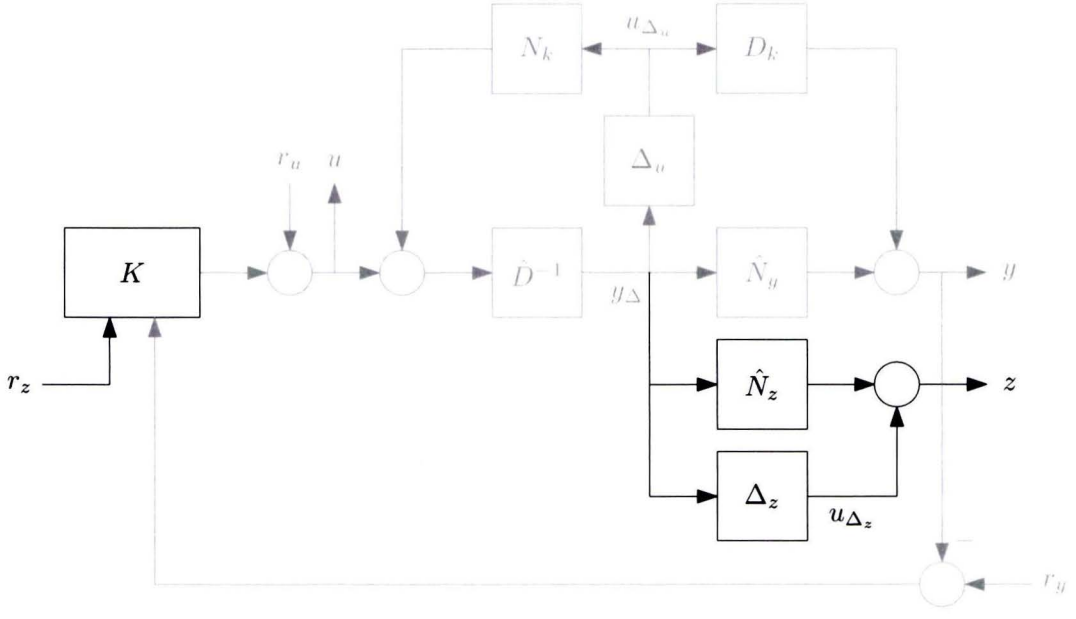

Figure 6.3: Dual-Youla parametrization for the inferential control structure.

difference between the open-loop and closed-loop case will be discussed more thoroughly in Subsection 6.2.3.

The dual-Youla parametrization (6.25) for the inferential control structure has the same properties as the parametrization Figure 6.2 for the standard case, and therefore it can be used for the model validation procedure in similar fashion. In the next section, the model validation procedure and experimental results on the flexible beam will be discussed.

6.2 Model validation procedure

In order to validate a model, the systematic errors, noise and disturbances need to be addressed appropriately. If the dynamics of the model are different than those of the plant, the stabilizing properties of a subsequent controller design are influenced, and this can lead to undesirable closed-loop behavior. Therefore, it is necessary to take these errors in account during controller design, and to model them as a perturbation Δ on the model $\hat{M}$, as in Figure 6.1. In contrast, noise and disturbances do not influence the stability of the system, and therefore they should be contributed to a separate disturbance model.

The first step in the model validation procedure is to obtain a disturbance model. The remaining errors, that are not addressed by the disturbance model, are then contributed to systematic errors. This requires the disturbance model to be deterministic, which is not common in literature, and therefore it is discussed in Subsection 6.2.1. In Subsection 6.2.2 a disturbance model is obtained for the flexible beam experimental setup. Then, the systematic errors can be obtained using the generalized structured singular value problem, as discussed in Subsection 6.2.3.

6.2.1 Estimating a deterministic disturbance model

As explained in the introduction of this chapter, the differences between model and data are caused by disturbances and model errors. It is essential that both are addressed appropri-

ately. Since there is a trade-off between the size of the perturbation and disturbance models, the contribution of the disturbances is not allowed to be too large, because this implies a perturbation model that is too small, and consequently it is not guaranteed that the dynamics of the true system are included in the model set. Conversely, if the disturbance model is too small, the uncertainty model is overly conservative, at the expense of lower performance. Therefore, it is essential that the disturbances are estimated accurately, which is done using the procedure in [33]. This procedure uses a frequency domain approach that is consistent with the control-relevant identification procedure, and is evaluated at a frequency grid ω_i. An advantage of this approach is that the disturbance model can be nonparametric, so no approximation errors occur.

It is not straightforward to estimate a deterministic disturbance model directly, and therefore it will be derived from a stochastic description, which is common since noise and disturbances often are of a stochastic nature. The disturbance is modeled as a stochastic variable $v = H_o e$, where e comes from a distribution with zero mean and unit covariance. Under this assumption the Fourier transform $V_N\left(e^{j\omega_i}\right)$ of v, converges to a circular complex normal distribution for $N \to \infty$ [40, Ch. 14], which is defined as follows.

Definition 6.2 (Circular complex normal distribution [40, Ch. 14])**.** For a complex random vector Z, the circular complex normal distribution $\mathcal{N}_c(m_z, C_z)$ is defined by its mean m_z, covariance matrix $C_z = C_z^* \geq 0$, and the circularity property

$$\mathbb{E}\left\{(Z - m_z)(Z - m_z)^T\right\} = 0. \tag{6.28}$$

Although this stochastic model characterizes the disturbance, it is not suitable for the model validation procedure. Therefore, the disturbance will be modeled as a complex perturbation of which the magnitude is determined by the covariance of the disturbance and a probability level. First it must be assured that the elements of V_N are uncorrelated, this can be achieved using the following transformation,

$$\tilde{V}\left(e^{j\omega_i}\right) = T_v^*(\omega_i) V_N\left(e^{j\omega_i}\right), \tag{6.29}$$

where T_v^* follows from the eigenvalue decomposition of the covariance

$$C_v(\omega_i) = T_v(\omega_i) \Lambda_v(\omega_i) T_v^*(\omega_i). \tag{6.30}$$

The diagonality of $\Lambda_v(\omega_i) = \operatorname{diag}(\lambda_1, \ldots, \lambda_n)$ ensures there is no correlation between the elements. A deterministic disturbance model is obtained in the form of a structured perturbation, of which the magnitude

$$\bar{\tilde{V}}(\omega_i) = \sqrt{\frac{1}{2}\Lambda_v \chi^2_{2,1-\alpha}}, \tag{6.31}$$

is chosen such that it is an "upper bound" for the disturbance, with probability $\alpha \in [0, 1)$. The perturbation has a diagonal structure defined by the set

$$\boldsymbol{\Delta}_v = \{\operatorname{diag}(\delta_1, \ldots, \delta_n) | \delta_q \in \mathbb{C},\ q = 1, \ldots, n\}, \tag{6.32}$$

which has the same size as Λ_v. The deterministic disturbance model is then given by $\boldsymbol{V}(\omega_i) = \left\{T_v(\omega_i) \Delta_v \bar{\tilde{V}}(\omega_i) \middle| \Delta_v \in \mathcal{B}\boldsymbol{\Delta}_v\right\}$, where $\mathcal{B}$ denotes the unit ball, i.e., $\|\Delta_v\|_\infty \leq 1$.

In practice the covariance and mean of V_N are not known a priori, but need to be estimated from measurement data Z_N. The covariance is estimated with

$$\hat{C}_v(\omega_i) = \frac{1}{n_{\text{exp}} - 1} \sum_{r=1}^{n_{\text{exp}}} (Z_r(\omega_i) - \hat{m}_{Z_r}(\omega_i))(Z_r(\omega_i) - \hat{m}_{Z_r}(\omega_i))^*, \tag{6.33}$$

where the mean is given by

$$\hat{m}_{Z_r}(\omega_i) = \frac{1}{n_{\text{exp}}} \sum_{r=1}^{n_{\text{exp}}} Z_r(\omega_i). \tag{6.34}$$

These estimators converge to the true values of C_v and m_Z for $n_{\text{exp}} \to \infty$.

With the deterministic disturbance model, the model validation setup in Figure 6.1, now can be examined in the frequency domain, by taking the Fourier transforms of the input signal w_m, and the output signals z and z_m, as shown in Figure 6.4. In this figure, the residual of the model is given by

$$E = Z_m - \mathcal{F}_u\left(\hat{M}, \Delta_u\right) W_m - T_v \Delta_v \bar{\bar{V}} \mathbf{1}. \tag{6.35}$$

Note that only Δ_u is still unknown in the right hand side of the equation. This equation also clearly shows the trade-off between the sizes of the model perturbation and the disturbance model. When the disturbance model is too large, consequently the perturbation model becomes too optimistic, which is undesirable because then it is not guaranteed that the plant dynamics are encompassed by the model set. This optimism can be reduced by considering the output of the model,

$$Z = \mathcal{F}_u\left(\hat{M}, \Delta_u\right) W_m + T_v \Delta_v \bar{\bar{V}} \mathbf{1}. \tag{6.36}$$

By normalizing (6.36) it becomes

$$\bar{Z} = \frac{\mathcal{F}_u\left(\hat{M}, \Delta_u\right) W_m}{\|W_m\|_2} + \frac{T_v \Delta_v \bar{\bar{V}} \mathbf{1}}{\|W_m\|_2}. \tag{6.37}$$

Then, by increasing the input with a factor α the following result is obtained,

$$\bar{Z} = \frac{\mathcal{F}_u\left(\hat{M}, \Delta_u\right) \alpha W_m}{\|\alpha W_m\|_2} + \frac{T_v \Delta_v \bar{\bar{V}} \mathbf{1}}{\|\alpha W_m\|_2} \tag{6.38}$$

$$= \frac{\mathcal{F}_u\left(\hat{M}, \Delta_u\right) W_m}{\|W_m\|_2} + \frac{T_v \Delta_v \bar{\bar{V}} \mathbf{1}}{\alpha \|W_m\|_2}. \tag{6.39}$$

For $\alpha > 1$ this implies that the first term remains constant but that the second term, which is the disturbance model, decays. Consequently, the perturbation model will become less optimistic. Note that instead of increasing the input with α, it is also possible to average over M periods to obtain $\alpha = \sqrt{M}$, similar as in Subsection 2.2.2.

6.2.2 Experimental results for disturbance modeling

The theory from the previous subsection is confronted with a true system, by performing experiments on the flexible beam setup. In these experiments the system is excited with four input signals.

The first experiment, is the identification experiment from Subsection 4.5.3, that uses a multi-sine input signal with frequency content at multiples of 1 Hz, and random phase. Using random phase, prevents the input signal from having large amplitudes when all sines are at their maximum amplitude at the same time. This input signal is also used, in the second experiment, to verify the results with a second measurement, i.e., with different noise and disturbances. The third experiment uses an input signal with the same frequency content, but the sines have different random phase. In the last experiment the frequency content is

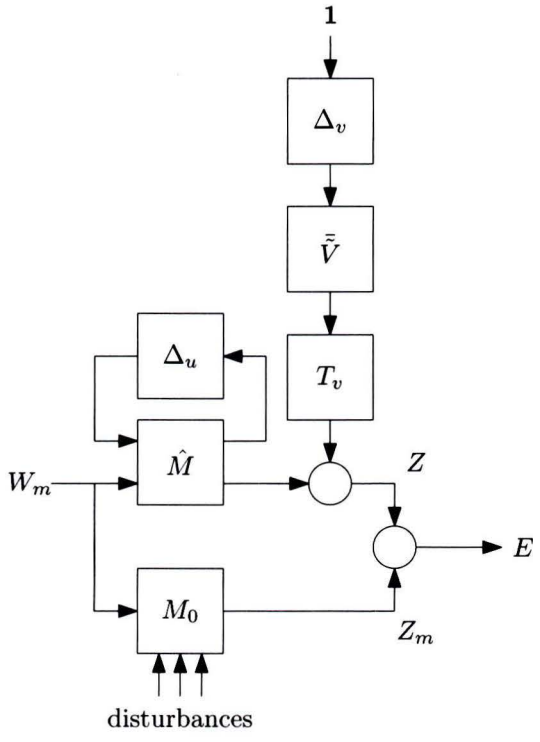

Figure 6.4: Model validation problem in the frequency domain.

spaced 1 Hz apart, starting at 0.5 Hz up to the Nyquist frequency. The input signals used in the third and fourth experiment are not related to the first input signal, and can therefore be used to verify that the identified model does not depend on the input signal.

For the four obtained data sets, the deterministic disturbance model $\boldsymbol{V}(\omega_i)$ is calculated and the results are shown in Figure 6.5. It can be seen that at certain frequencies differences between the disturbance models occur. However, at the locations of resonances they show the same behavior, i.e., the magnitude is larger than at the surrounding frequencies. This can be explained by comparing the magnitude of the disturbance model to the magnitude of the plant, as follows.

In order to get an idea of the magnitude of the disturbances in relation to the nonparametric model of the plant, Figure 6.6 shows the frequency response of the plant (blue $-$) and the 99% probability interval (yellow area) of the disturbance model. It can be concluded that at the frequencies where the magnitude of the frequency response function is large, the disturbances are relatively small, and that the relatively large disturbances occur in the zeros of the plant. This may explain why the largest differences between the disturbance models in Figure 6.5, occur around the the zeros of the plant.

Figure 6.6 also shows the identified model (green $--$). Observe that not all model errors can be contributed to noise and disturbances, since the model is not entirely contained by the 99% probability interval. Note that this figure only shows the results of one experiment for clarity, but in the validation procedure all four experiments are used.

With these disturbance models, a model set can be obtained such that the uncertain model is not invalidated.

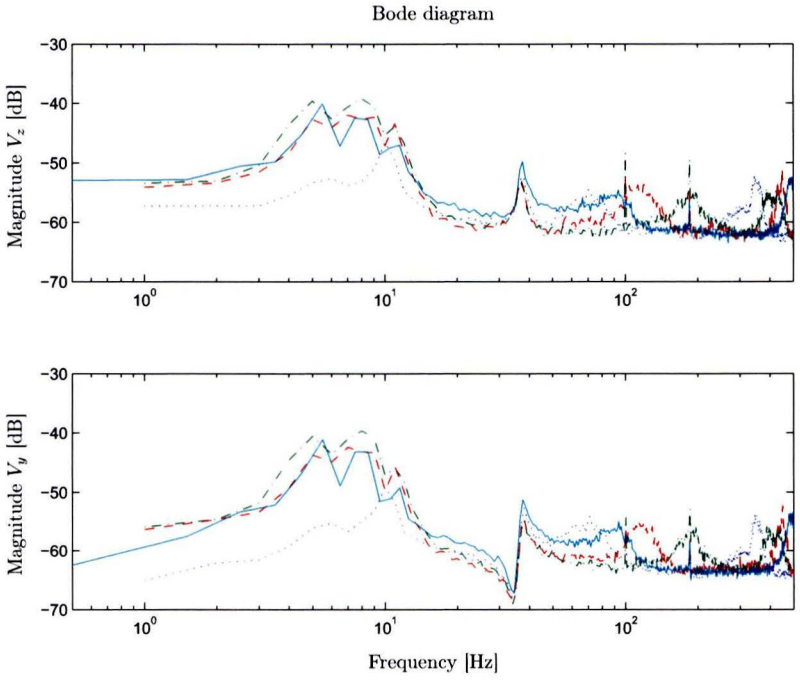

Figure 6.5: Bounds on the disturbances in the data, with a 99% probability level. The four data sets are obtained during identification (blue $\cdots$), with the same input signal as the identification (green $-\cdot$), with different phase (red $--$), and different frequency content (cyan $-$).

6.2.3 Addressing systematic modeling errors

The goal of this step in the model validation procedure, is to obtain the smallest model set that is not invalidated by the experimental data. In this step the systematic modeling error needs to be addressed, such that in conjunction with the disturbance model, at least one model in the obtained model set explains the measurement data. This can be evaluated by rearranging the problem to a form that can be solved using a generalization of the structured singular value μ.

In Subsection 6.1.3 it was claimed that under closed-loop conditions, the perturbations Δ_z and Δ_u could be separated. This is shown by the following proof, which considers the closed-loop transfer function of the nine-block problem, given by

$$T(G,K) = \begin{bmatrix} G_z \\ G_y \\ I \end{bmatrix} (I + K_2 G_y)^{-1} \begin{bmatrix} K_1 & K_2 & I \end{bmatrix}. \tag{6.40}$$

By substituting G_z and G_y with the dual-Youla parametrization for the inferential control structure (6.25) in the right hand side of the equation, this becomes

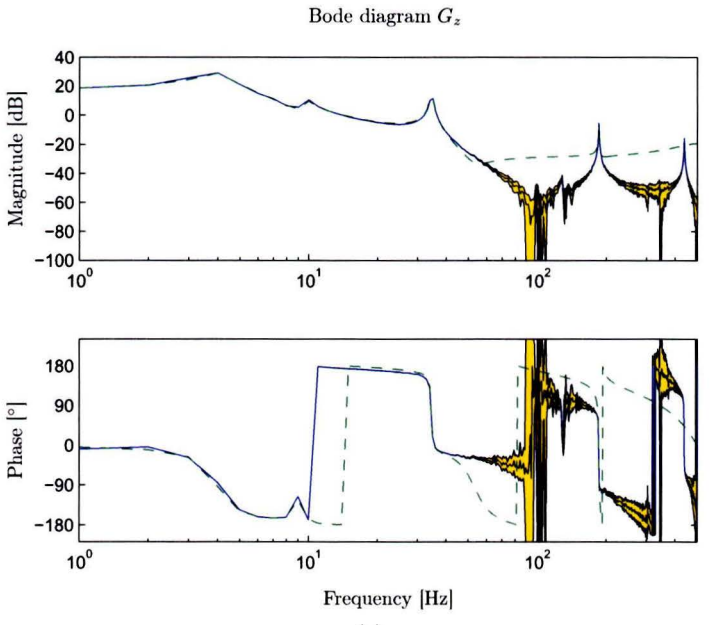

(a)

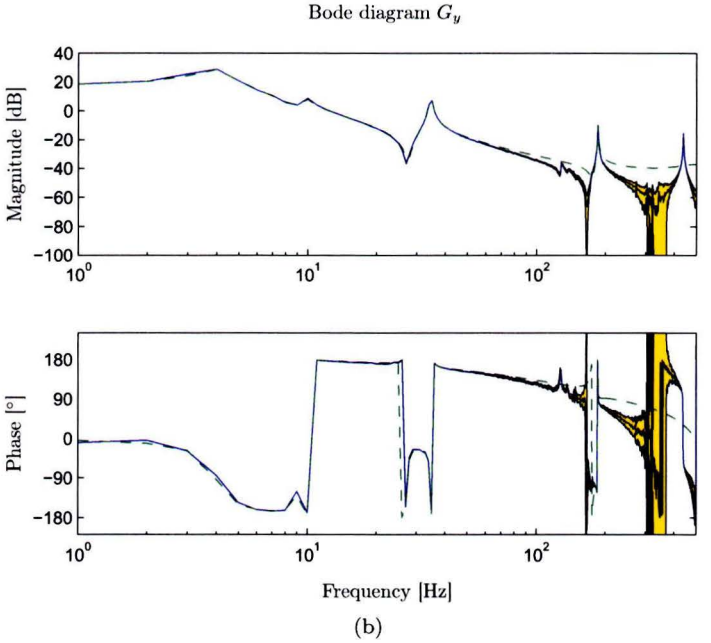

(b)

Figure 6.6: The 99% probability interval of the disturbance model (yellow area) around the frequency response function of the plant (blue $-$), compared to the identified model (green $--$), for G_z (a) and G_y (b).

$$T(G,K) = \begin{bmatrix} \hat{N}_z + \Delta_z \\ \hat{N}_y + D_k\Delta_u \\ \hat{D} - N_k\Delta_u \end{bmatrix} \left(\hat{D} - N_k\Delta_u\right)^{-1} (I + K_2G_y)^{-1} \begin{bmatrix} K_1 & K_2 & I \end{bmatrix} \tag{6.41}$$

$$= \begin{bmatrix} \hat{N}_z + \Delta_z \\ \hat{N}_y + D_k\Delta_u \\ \hat{D} - N_k\Delta_u \end{bmatrix} \left(\hat{D} - N_k\Delta_u + K_2G_y\left(\hat{D} - N_k\Delta_u\right)\right)^{-1} \begin{bmatrix} K_1 & K_2 & (6.42) \end{bmatrix}$$

By substituting the G_y again with the dual-Youla parametrization, and K_2 with its right coprime factorization, the terms containing Δ_u cancel out,

$$T(G,K) = \begin{bmatrix} \hat{N}_z + \Delta_z \\ \hat{N}_y + D_k\Delta_u \\ \hat{D} - N_k\Delta_u \end{bmatrix} \left(\hat{D} - N_k\Delta_u + N_kD_k^{-1}\left(\hat{N}_y + D_k\Delta_u\right)\right)^{-1} \begin{bmatrix} K_1 & K_2 & (6.43) \end{bmatrix}$$

$$= \begin{bmatrix} \hat{N}_z + \Delta_z \\ \hat{N}_y + D_k\Delta_u \\ \hat{D} - N_k\Delta_u \end{bmatrix} \left(\hat{D} - N_k\Delta_u + N_kD_k^{-1}\hat{N}_y + N_k\Delta_u\right)^{-1} \begin{bmatrix} K_1 & K_2 & I & (6.44) \end{bmatrix}$$

$$= \begin{bmatrix} \hat{N}_z + \Delta_z \\ \hat{N}_y + D_k\Delta_u \\ \hat{D} - N_k\Delta_u \end{bmatrix} \left(\hat{D} + K_2\hat{N}_y\right)^{-1} \begin{bmatrix} K_1 & K_2 & I \end{bmatrix}, \tag{6.45}$$

and therefore under closed-loop z does not depend on the uncertainty Δ_u, which means that Δ_u and Δ_z can be separated. Using this result, it is straightforward to derive $\hat{M}$ (6.26) from the block scheme in Figure 6.3.

For the four-block problem (3.2), the model validation setup in Figure 6.4, can be rearranged as in Figure 6.7, which represents the validation problem for the four-block structure,

$$\mathbf{0} = Z_m - \mathcal{F}_u\left(\hat{M}, \Delta_u\right) W_m - T_v\bar{\bar{V}}\Delta_v^{(u)}\mathbf{1}. \tag{6.46}$$

Similarly, for Δ_z the validation problem becomes

$$\mathbf{0} = Z_m - \mathcal{F}_u\left(\hat{M}, \Delta_z\right) W_m - T_v\bar{\bar{V}}\Delta_v^{(z)}\mathbf{1}. \tag{6.47}$$

Note that (6.46) and (6.47) are matrix equations that are evaluated at the frequencies ω_i in the frequency grid. Since these problems are identical, only the four-block problem will be discussed here. In Section 6.3 the results for both problems will be shown.

In the parametrization of the model set (6.25) it is required that $\Delta_u \in \mathcal{RH}_\infty$, such that it is guaranteed that the model is valid. In order to reduce the size of the model set, and thus to reduce potential conservatism, this is replaced with $\|\Delta_u\|_\infty < \gamma_u(\omega_i)$. The minimal model set can then be obtained by searching for the smallest γ_u that does not invalidate the model.

Then the last step that remains in the model validation procedure, is testing the validity of a model set for a given γ_u. Since both Δ_u and Δ_v need to be considered, this is not a straightforward problem. The solution can be found in the generalized structured singular value, which is defined as follows.

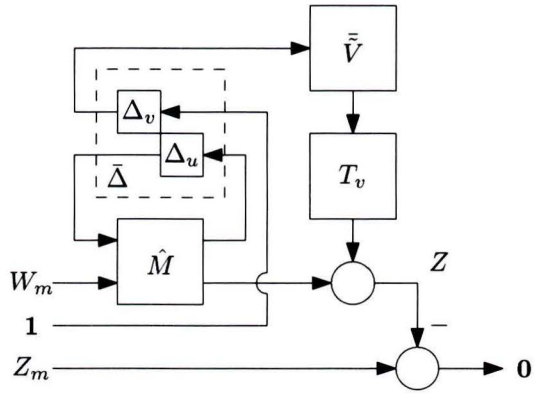

Figure 6.7: Graphical representation of matrix equations (6.46) and (6.47), evaluated at the frequencies ω_i in the frequency grid.

Definition 6.3 (Generalized structured singular value [38])**.** The generalized structured singular value (GSSV) is defined as

$$\bar{\mu}_{\bar{\Delta}}(M,N) = \left(\min_{\bar{\Delta}} \left\{ \bar{\sigma}(\bar{\Delta}) \middle| \bar{\Delta} \in \bar{\mathbf{\Delta}}, \ker \begin{pmatrix} I - \bar{\Delta}M \\ N \end{pmatrix} \neq 0 \right\}\right)^{-1}, \tag{6.48}$$

unless $\ker \begin{pmatrix} I - \bar{\Delta}M \\ N \end{pmatrix} = 0 \ \forall \bar{\Delta} \in \bar{\mathbf{\Delta}}$, in which case $\bar{\mu}_{\bar{\Delta}}(M,N) = 0$.

The GSSV is used to analyze a system with the structure shown in Figure 6.8. Here $\bar{\Delta}$ is a structured perturbation with

$$\bar{\Delta} \in \boldsymbol{\mathcal{B}}\bar{\mathbf{\Delta}}, \ \bar{\mathbf{\Delta}} = \begin{bmatrix} \Delta_v & \\ & \Delta_u \end{bmatrix}. \tag{6.49}$$

The interconnection structure $\bar{M}$ contains the relevant closed-loop transfer functions selected from $\hat{M}$ (6.26), appended with an additional input and output for the disturbance model. For the Δ_u this becomes

$$\bar{M}_y = \left[\begin{array}{cc|c} 0 & 0 & 1 \\ 0 & 0 & \left(\hat{D} + K_2\hat{N}_y\right)^{-1} \begin{bmatrix} K_1 & K_2 & I \end{bmatrix} VW_m \\ \hline -T_v\bar{\bar{V}} & -\gamma_u W_y D_k & Z_m - W\hat{G}_y\left(I + K_2\hat{G}_y\right)^{-1} \begin{bmatrix} K_1 & K_2 & I \end{bmatrix} VW_m \end{array}\right],$$

and in the inferential control configuration (3.13) the structure for Δ_z becomes

$$\bar{M}_z = \left[\begin{array}{cc|c} 0 & 0 & 1 \\ 0 & 0 & \left(\hat{D} + K_2\hat{N}_y\right)^{-1} \begin{bmatrix} K_1 & K_2 & I \end{bmatrix} VW_m \\ \hline -T_v\bar{\bar{V}} & -\gamma_z W_e & Z_m - W\hat{G}_z\left(I + K_2\hat{G}_y\right)^{-1} \begin{bmatrix} K_1 & K_2 & I \end{bmatrix} VW_m \end{array}\right].$$

Note that $T_v\bar{\bar{V}}$ and γ_u, γ_z are absorbed in the structure, and therefore $\bar{\Delta}$ is in the unit ball as in (6.49).

At the frequencies ω_i this problem can be evaluated for any $\alpha \in \mathbb{C}\backslash 0$, and the minimum value of $\gamma_u(\omega_i)$ such that

$$\mathcal{F}_u\left(\bar{M}, \bar{\Delta}\right) = \mathbf{0}, \tag{6.50}$$

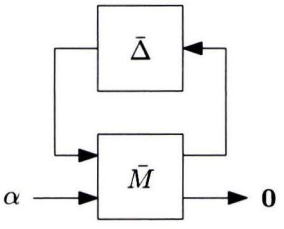

Figure 6.8: Interconnection structured used in the generalized structured singular value.

can be obtained. In [35, Sec. 6.2] it is proved that (6.50) is equivalent to the following proposition:

Proposition 6.1 ([35, Proposition 23]). *The model is not invalidated if and only if*

$$\bar{\mu}_{\bar{\Delta}}\left(\bar{M}_{11} - \bar{M}_{12}\bar{X}_{22}\bar{M}_{21},\ \bar{M}_{21} - \bar{M}_{22}\bar{X}_{22}\bar{M}_{21}\right) > 1, \tag{6.51}$$

where $\bar{X}_{22}$ is a matrix that satisfies $\bar{X}_{22}\bar{M}_{22} = I$.

With the generalized structured singular value, a tool is available that makes a clear distinction between the models that are invalidated and those that are not. The minimum value of $\gamma_u(\omega_i)$ can then be obtained, using a bisection algorithm. The next section discusses the experimental results on the flexible beam setup.

6.3 Obtaining a model set for the flexible beam setup

As mentioned in Subsection 6.2.2, four data sets have been used to derive an equal number of disturbance models. For each of these data sets, the minimum values for $\gamma_u(\omega_i)$ and $\gamma_z(\omega_i)$, such that the model is not invalidated, have been calculated using the dual-Youla parametrization for inferential control, and the generalized structured singular value $\bar{\mu}_{\bar{\Delta}}$, as discussed in Subsection 6.2.3. Since only one uncertain model at a time can be used for controller synthesis, the maximum values of $\gamma_u(\omega_i)$ and $\gamma_z(\omega_i)$ will be used. This assures that the model is not invalidated by all four data sets.

The controller synthesis algorithm also requires that the uncertainty model is parametric, since it needs to be absorbed in the generalized plant structure. Therefore, a parametric upper bound for $\gamma_u(\omega_i)$ and $\gamma_z(\omega_i)$ is designed. In order to avoid conservatism this bound needs to be tight. However, a relatively low order is desirable in the perspective of robust controller design. Therefore, for $\gamma_u(\omega_i)$ an 8^{th} order state-space model is designed, and for $\gamma_z(\omega_i)$ a 15^{th} order. The result is shown in Figure 6.9, where the values of $\gamma_u(\omega_i)$ and $\gamma_z(\omega_i)$ are shown (blue $\cdot$), along with the resulting nonparametric uncertainty model (blue $--$), and the parametric overbound (green $-$).

In the parametrization of the plant (6.25) the right coprime factorization of the nominal model plays an important role. Figure 6.10 shows the uncertainty in the RCFs of this plant,

$$\begin{bmatrix} N_z \\ N_y \\ D \end{bmatrix} = \begin{bmatrix} \hat{N}_z + \Delta_z \\ \hat{N}_y + D_k\Delta_u \\ \hat{D} - N_k\Delta_u \end{bmatrix}. \tag{6.52}$$

At each frequency ω_i, the uncertainty is a circle in the complex plane, of which the magnitude of $\gamma_u(\omega_i)$ or $\gamma_z(\omega_i)$ determines the radius. This means that the minimum and maximum of the magnitude and phase, can be derived using basic geometry. Note that this is possible because Δ_z and Δ_u are independent (1×1) blocks. In Figure 6.10 the magnitude of the

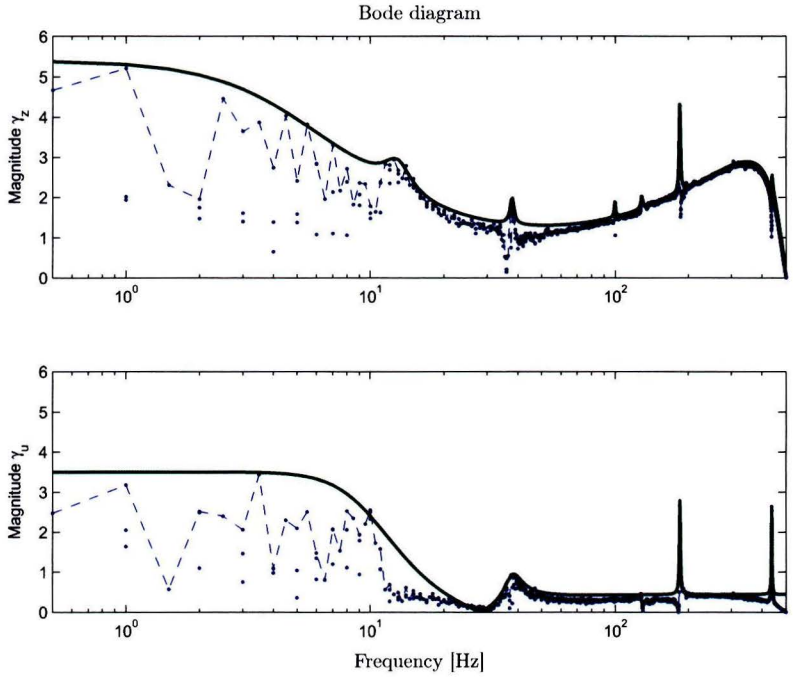

Figure 6.9: Minimum values of γ_u and γ_z over ω_i such that the model is not invalidated by the measurement data (blue $\cdot$), maximum of these values (blue $--$), and the designed parametric overbound (green $-$).

right coprime factorization of $\hat{G}$ is shown (red $--$), along with the perturbations around it (cyan area). In Appendix B, it is discussed how this graphical representations of the model sets are made. It can be seen that the influence of the model uncertainty is the largest in the high frequency range for N_z and N_y, and in less extent in the low frequency range for D. Around the desired bandwidth, as specified in the weighting filter design in Subsection 4.5.2, the perturbations have relatively small magnitude for all three coprime factors. This is a direct consequence from the control-relevant identification procedure, that provides a close approximation of the measurement data in this frequency range. Note that also the magnitude of the perturbation on the resonance at 185 Hz is relatively small. This pole can cause instability of the closed-loop system for high controller gains, and is therefore relevant for control.

The same can also be observed in Figure 6.11, which shows the nominal model (red $--$) and nonparametric perturbations (cyan area) corresponding with these coprime factors, and the data of the four experiments (blue $\cdot$), for G_z (a) and G_y (b). The figure also shows that all data points lie within the bounds on magnitude and phase of the model set, which indicates that the uncertain model is consistent with the measurement data.

The final result is shown in Figure 6.12, which shows the nominal model (red $--$), parametric uncertainty (cyan area), and measurement data (blue $\cdot$), for G_z (a) and G_y (b). It can be seen that the designed overbound resembles the shape of the nonparametric uncertainty closely, and although it is larger than the nonparametric model at all frequencies, the bounds on the perturbations are still tight in the control-relevant frequency ranges, i.e., in the bandwidth of the controller and at the resonance at 185 Hz.

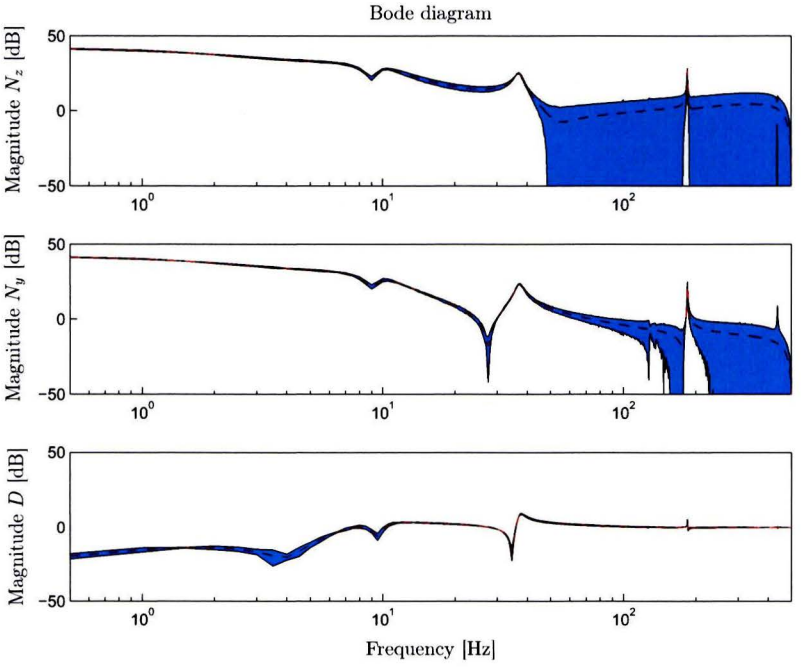

Figure 6.10: The nonparametric perturbations $\gamma(\omega_i)$ from Figure 6.9 (cyan area) on the coprime factorization of the nominal model (red $--$), as in (6.52).

6.4 Conclusions

The modeling errors in the model obtained by the control-relevant identification procedure in Chapter 4, are addressed in an uncertainty model, by means of model validation for robust control. The most important conclusions from this chapter are as follows.

- The dual-Youla parametrization is extended for the inferential control configuration, maintaining its beneficial properties. This guarantees that the dynamics of the true plant are encompassed by the model set, if the plant is stabilized by the experimental controller.
- For the flexible beam experimental setup, the magnitude of the model uncertainty below the desired bandwidth frequency of the closed-loop system, as well as at the resonance at 185 Hz, is tight. Hence, it can be concluded that the identified model is the most accurate in these frequency ranges.
- For the flexible beam, the model uncertainty in the inferential control structure consists of two independent 1×1 blocks. This is an advantageous property, since it implies that the bounds on both uncertainty blocks can be determined separately.
- The uncertainty bounds on the experimental setup, obtained with the model validation procedure, are close to the nominal model and experimental data, resulting in a model set that is not overly large. This will result in small conservatism of the subsequent robust controller designs.

With the validated model set, it is now possible to synthesize controllers that robustly stabilize the plant and optimize the worst-case performance of the model set. This will be discussed in Chapter 7.

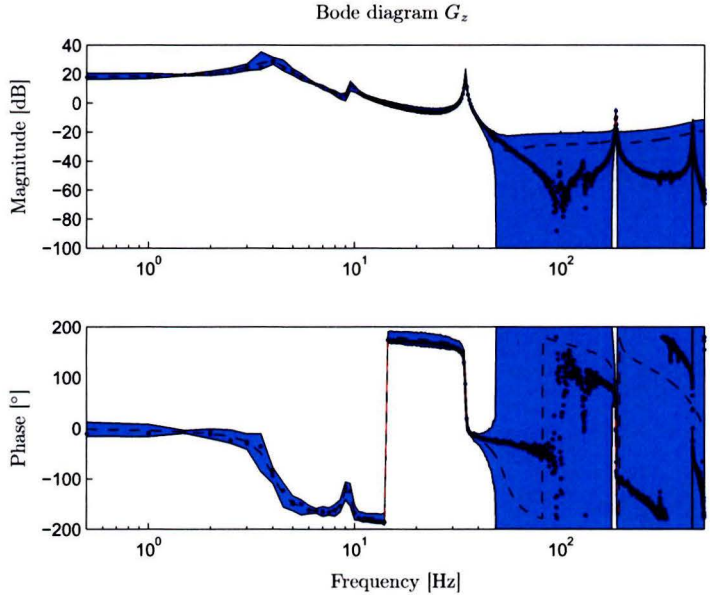

(a)

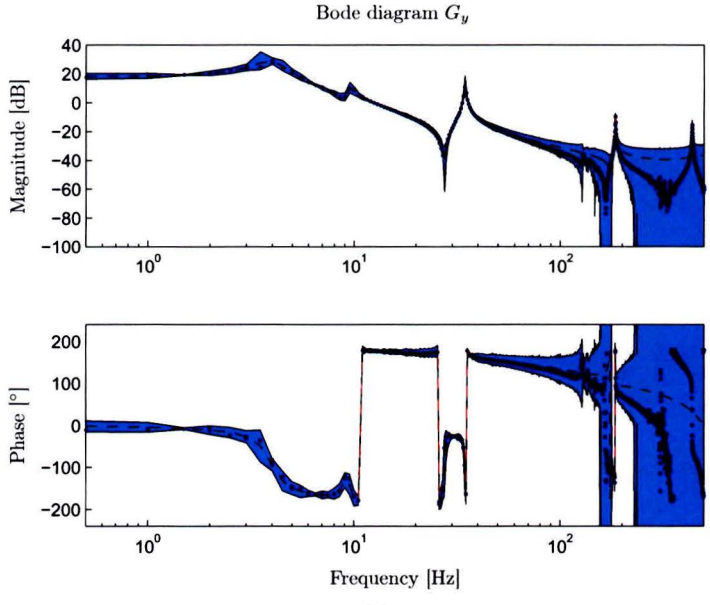

(b)

Figure 6.11: Measurement data (blue ·), and nonparametric perturbations $\gamma(\omega_i)$ from Figure 6.9 (cyan area) on the nominal model (red $--$), for G_z (a) and G_y (b) according to the parametrization in (6.25).

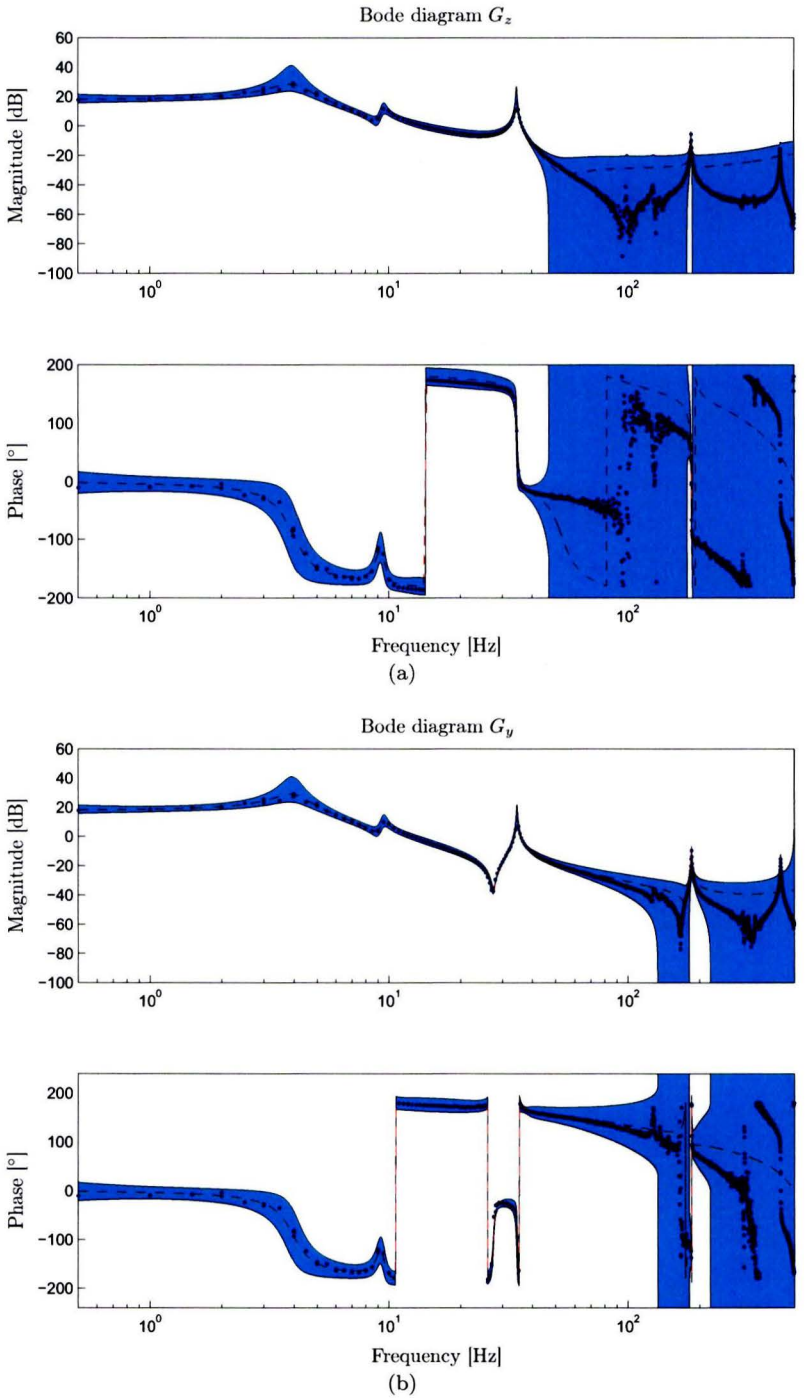

Figure 6.12: Measurement data (blue ·), and overbound of the nonparametric perturbations $\gamma(\omega_i)$ from Figure 6.9 (cyan area) on the nominal model (red $--$), for G_z (a) and G_y (b) according to the parametrization in (6.25).

Chapter 7

Robust controller synthesis

With the model set obtained in Chapter 6, it is possible to synthesize robust controllers that guarantee that the true plant is internally stabilized. A reliable procedure to synthesize optimal robust controllers, is by means of D-K iteration, see for instance [26, 45]. In this procedure the μ-synthesis problem is solved iteratively, by determining a scaling matrix D based on the upper-bound for $\mu_{\Delta}(M)$, and designing an $\mathcal{H}_\infty$-optimal controller K for the scaled problem. Although a globally optimal solution is not guaranteed, many successful applications have been reported.

The standard μ-synthesis problem aims at optimizing both robustness and performance at once. However, in the model validation procedure presented in Chapter 6, the model uncertainty has been determined accurately and the required robustness is known, i.e., there is no need optimize robustness. Therefore, the so-called skewed-μ-synthesis, as in [11], is discussed in Section 7.1. In Section 7.2 controllers are synthesized and the results are discussed. Closed-loop step responses are simulated using these controllers and the identified model, the controllers are also implemented on the experimental setup. The results are presented in Section 7.3. In Section 7.4, some conclusions are drawn.

7.1 Skewed μ-synthesis

Standard μ-analysis expresses robustness and performance in one single number $\mu_{\hat{\Delta}}$. For optimal controller synthesis, this implies that there is only one optimization criterion, in which optimizing performance and robustness are coupled. Therefore, this method cannot deal with uncertainties of which the bounds already have been determined, such as the uncertainty model obtained in Chapter 6. This is explained in the following example.

Example 7.1 (μ-synthesis)**.** Consider the $M\Delta$-structure (see Figure 3.5), for which an optimal controller is computed by means of μ-synthesis, with respect to

$$\hat{\Delta} = \begin{bmatrix} \Delta & 0 \\ 0 & \Delta_P \end{bmatrix}.$$

Additionally, it is given that the model uncertainty is $\|\Delta\|_\infty < 1$. Then, consider the following possible results of the controller synthesis algorithm.

1. $\mu_{\hat{\Delta}}(M) = 2$: The controller is robust against uncertainties $\|\Delta\|_\infty < \frac{1}{2}$, which is insufficient for stabilization of all plants in the model set.

2. $\mu_{\hat{\Delta}}(M) = \frac{1}{2}$: The controller is robust against uncertainties $\|\Delta\|_\infty < 2$, i.e., it is overly robust, at the expense of lower performance.

Both results are undesirable in the given scenario, and therefore another approach is motivated.

The problem in Example 7.1 can be solved by means of skewed μ-synthesis [11], which considers the following two cases, where β bounds the uncertainty, i.e., $\|\Delta\|_\infty < \beta$, and α is the performance level, i.e., $\|\mathcal{F}_u(M,\Delta)\|_\infty < \alpha$:

1. *Given β, determine the smallest α with the property that, for any uncertainty bounded by β, an $\mathcal{H}_\infty$ performance level α is guaranteed.*

2. *Conversely, given α, determine the largest β with the property that, again, for any uncertainty bounded by β, an $\mathcal{H}_\infty$ performance level of α is guaranteed.*

Here we are interested in the first case, since this allows a predetermined value β to quantize the amount of uncertainty in the model, as it was determined in the model validation procedure in Chapter 6, and then optimizes the performance level α. Skewed μ is defined as follows.

Definition 7.1 (Skewed μ [11])**.**

$$\mu_{\tilde{\Delta}}^s = \left(\min_{\tilde{\Delta} \in \tilde{\mathbf{\Delta}}} \left\{ \bar{\sigma}(\Delta_P) \middle| \det\left(I + \tilde{\Delta}M\right) = 0 \right\} \right)^{-1} \tag{7.1}$$

unless $\det\left(I + \tilde{\Delta}M\right) \neq 0 \forall \tilde{\Delta} \in \tilde{\mathbf{\Delta}}$, then $\mu_{\tilde{\Delta}}^s = 0$. Additionally, $\tilde{\mathbf{\Delta}}$ is given by

$$\tilde{\mathbf{\Delta}} = \left\{ \begin{bmatrix} \Delta_P & 0 \\ 0 & \Delta \end{bmatrix} \middle| \bar{\sigma}(\Delta) < 1 \right\}, \tag{7.2}$$

with Δ and Δ_P in complex spaces of appropriate dimensions.

The optimization problem for robust controller design then becomes

$$K^{\mathrm{RP}} = \arg\min_K \mu_{\tilde{\Delta}}^s(M). \tag{7.3}$$

As said before this can be achieved by using a modification to the D-K iteration algorithm. In the D-K iteration algorithm the optimal controller is found by iteratively solving for

$$\min_{K,D} \left\| DMD^{-1} \right\|_\infty, \tag{7.4}$$

where D is a block diagonal scaling matrix that commutes with $\tilde{\Delta}$, and K and D are modified alternately. By including

$$U = \begin{bmatrix} I_{n_p} & \\ & \frac{1}{\mu^s} I_n \end{bmatrix} \tag{7.5}$$

in the D-K iterations, i.e.,

$$\min_{K,D} \left\| DMD^{-1}U \right\|_\infty, \tag{7.6}$$

and updating U for every iteration, the optimal controller for the skewed μ problem can be obtained.

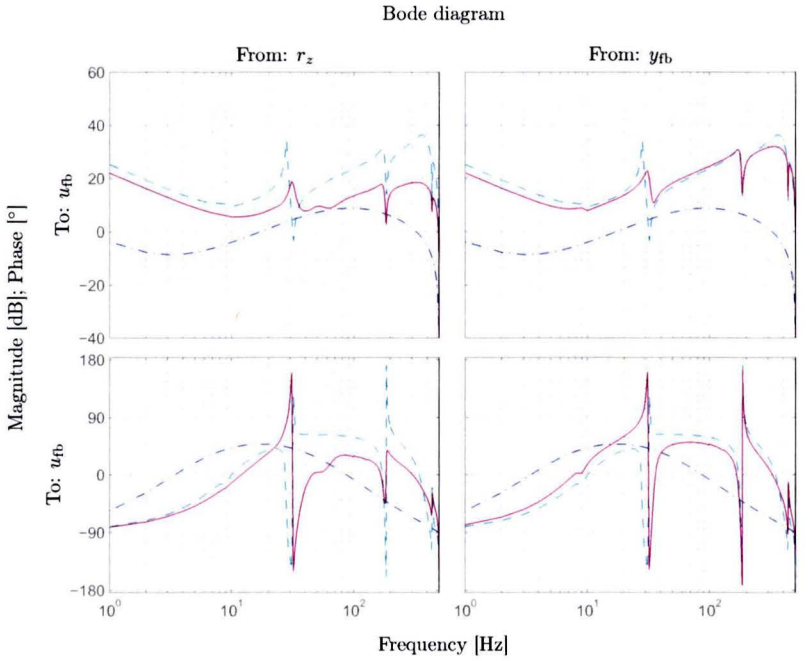

Figure 7.1: Experimental controller K^{exp} (blue $-\cdot$), robust optimal controller K_4^{RP} (cyan $--$) and robust inferential controller K_9^{RP} (magenta $-$).

7.2 Robust optimal controllers

The robust optimal controller K_4^{RP} (cyan $--$) and robust optimal inferential controller K_9^{RP} (magenta $-$), obtained using the skewed μ-synthesis of the previous section are shown in Figure 7.1, together with the experimental controller (blue $-\cdot$). In general, the robust controllers in this figure, are close to the controllers for the nominal model in Figure 5.1. This can be explained by the uncertainty of the control-relevant dynamics, that is relatively small. The gains for the robust controllers are lower over the full frequency range, and for the inferential controller the shape has changed around the anti-resonance and resonance at approximately 25 Hz and 35 Hz, respectively.

In Table 7.1 the obtained values of the (worst case) performance criteria are shown. From these values some conclusions can be drawn.

- For each controller the performance is better on the nominal model, than the worst case performance on over the model set, i.e, $\mathcal{J}\left(P_i^{\text{CR}}, K\right) \leq \mathcal{J}^{\text{WC}}\left(\mathcal{P}_i, K\right)$. This follows directly from the fact that $\mathcal{J}^{\text{WC}}\left(\mathcal{P}_i, K\right)$ is a measure for the worst case performance.

- The nominal performance of the optimal inferential controller, is better than the nominal performance of the standard optimal controller, $\mathcal{J}\left(P_9^{\text{CR}}, K_9^{\text{NP}}\right) < \mathcal{J}\left(P_9^{\text{CR}}, K_4^{\text{NP}}\right)$. In contrast, the worst case performance of the optimal inferential controller, is lower than the worst case performance of the standard optimal controller, $\mathcal{J}^{\text{WC}}\left(\mathcal{P}_9, K_9^{\text{NP}}\right) > \mathcal{J}^{\text{WC}}\left(\mathcal{P}_9, K_4^{\text{NP}}\right)$. Therefore, it can be concluded that the inferential controller is more sensitive to model uncertainties.

- For the nine-block problem, the worst case performance of the robust inferential controller, $\mathcal{J}^{\text{WC}}\left(\mathcal{P}_9, K_9^{\text{RP}}\right) = 10.88$, which is a factor 6.48 improvement relative to the performance of the optimal inferential controller for the nominal model, $\mathcal{J}^{\text{WC}}\left(\mathcal{P}_9, K_9^{\text{NP}}\right) =$

$\mathcal{J}(P,K)$	P_4^{CR}	P_9^{CR}	$\mathcal{P}_4^{\mathrm{WC}}$	$\mathcal{P}_9^{\mathrm{WC}}$
K^{exp}	123.01	196.82	125.50	201.38
K_4^{NP}	3.12	32.44	5.37	39.30
K_9^{NP}	-	7.80	-	70.54
K_4^{RP}	4.09	41.18	4.10	49.45
K_9^{RP}	-	9.34	-	10.88

Table 7.1: Obtained values of the performance criteria for the controllers shown in Figure 7.1, evaluated for the control-relevant four-block P_4^{CR} and inferential block structure P_9^{CR}, and the worst case performance for the model sets of the standard $\mathcal{P}_4$ and inferential $\mathcal{P}_9$ problem.

70.54. This indicates a large improvement in the robust performance for the inferential controller. In contrast, the nominal performance has decreased.

- The worst case performance of the robust inferential controller, $\mathcal{J}\left(\mathcal{P}_9^{\mathrm{WC}}, K_9^{\mathrm{RP}}\right) = 10.88$, which is a factor 4.55 improvement compared to the performance of the standard robust controller, $\mathcal{J}\left(\mathcal{P}_9^{\mathrm{WC}}, K_4^{\mathrm{RP}}\right) = 49.45$, i.e., inferential control has a positive influence on the achieved worst case performance.

- The performance of the robust controllers on the nominal model, is close to the worst case performance. This is indicates that the model uncertainties are relatively small, in the context of controller synthesis.

Figure 7.2 shows the closed-loop transfer functions from reference signal r_z to outputs y and z, for the controllers in Figure 7.1. It can be observed that in the high frequency range, the magnitudes of the closed-loop transfer functions for the robust controllers have decreased, relative to the magnitude of the nominal performance controllers in Figure 5.2. This is a consequence of the lower gain of the robust controllers, and reduces the high frequency noise transmission of the system.

Furthermore, the figure shows that for the inferential controller (magenta $-$), the magnitude has decreased even more around 40 Hz, as a result of the changed shape of the robust controller. Consequently, the "bandwidth" for output z has decreased, and slightly less performance is expected on the nominal model. This is in accordance with Table 7.1, which shows that the performance criterion $\mathcal{J}\left(P_9^{\mathrm{CR}}, K_9^{\mathrm{RP}}\right)$ is larger than $\mathcal{J}\left(P_9^{\mathrm{CR}}, K_9^{\mathrm{NP}}\right)$. Note that this does *not* imply, that the performance on the experimental setup decreases, since the performance of the experimental setup is only bounded by the worst case performance, i.e., $\mathcal{J}(P_0, K) \leq \mathcal{J}^{\mathrm{WC}}(\mathcal{P}, K)$.

7.3 Confirming theory by experiments

Figure 7.3 shows the simulated closed-loop step responses for the designed controllers on the nominal model. It can be observed that the responses of the robust standard optimal controller (cyan $--$) and robust inferential controller (magenta $-$), are close to controllers that are optimized for nominal performance in Figure 5.4. This is a result of the model validation procedure, that assures a tight bound for the perturbations on the nominal model.

This last conclusion is also confirmed by the experimental results, shown in Figure 7.4, which shows very similar results as Figure 7.3 for the simulations.

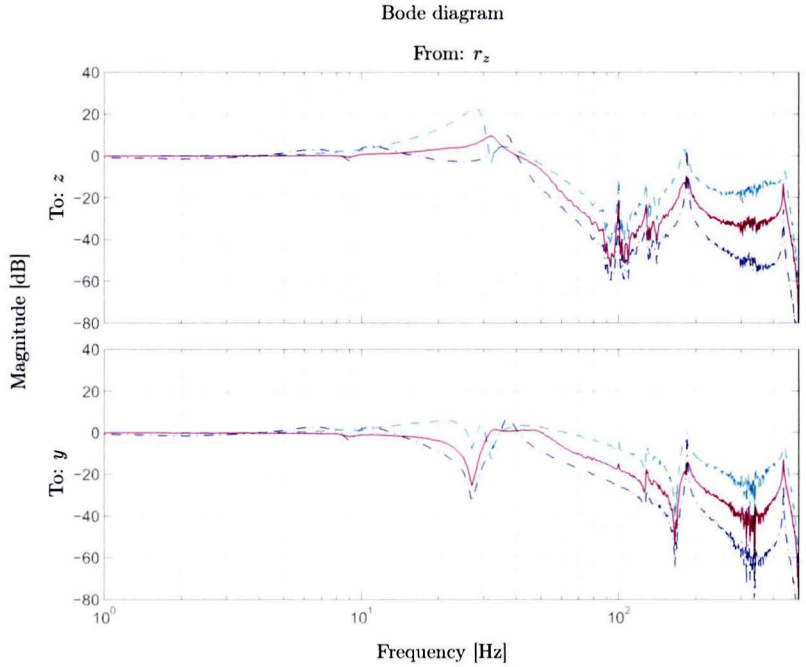

Figure 7.2: closed-loop transfer functions, corresponding to the controllers in Figure 7.1, experimental controller K^{exp} (blue $-\cdot$), robust optimal controller K_4^{RP} (cyan $--$) and robust inferential controller K_9^{RP} (magenta $-$).

7.4 Conclusions

In this chapter it has been discussed how controllers can be synthesized for models that are validated for robust control. The following conclusions are drawn.

- Skewed μ-synthesis is able to deal with uncertain models of which the magnitude of the perturbations has been determined prior to controller synthesis, such as models that have been validated with the model validation procedure from Chapter 6. Therefore, controllers designed using the skewed μ-synthesis, guarantee stabilization of the true system without being overly conservative.
- For the flexible beam, the increased robustness of the controller slightly decreases the performance, compared to the controllers optimized for nominal performance. However, the difference in performance between the inferential controller and standard robust controller, is still present. Hence, robust inferential control can be safely applied to structures with flexible dynamics, and substantially improve the performance.

With robust controller synthesis for the validated model, the proof of principle for the new inferential control technique is complete. Safe implementation on structures with flexible dynamics is possible, and all steps leading to this result have been confirmed by experiments on a prototype light-weight positioning system. In Chapter 8, the final conclusions of this thesis are presented along with recommendations for future research on this promising technique.

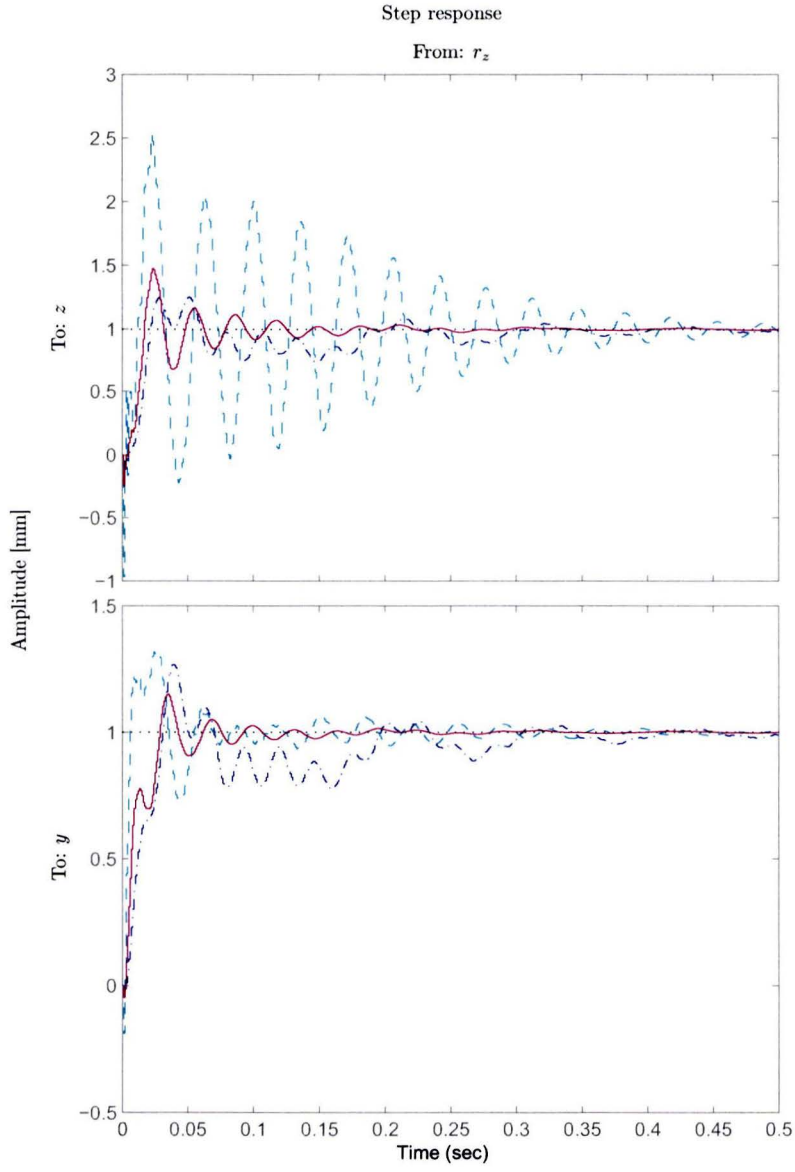

Figure 7.3: Simulated closed-loop step responses, corresponding to the controllers in Figure 7.1, the experimental controller K^{exp} (blue $-\cdot$), robust optimal controller K_4^{RP} (cyan $--$) and robust inferential controller K_9^{RP} (magenta $-$).

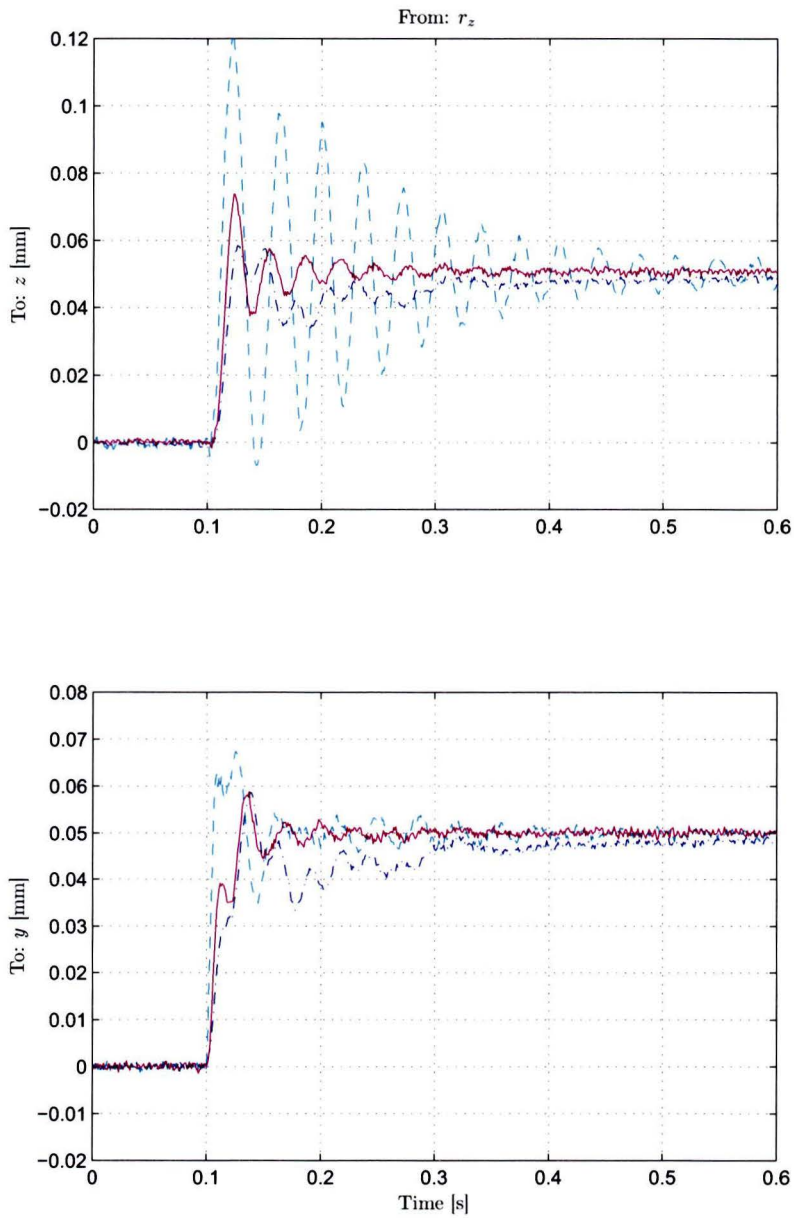

Figure 7.4: closed-loop step responses, obtained by implementing the controllers in Figure 7.1, the experimental controller K^{exp} (blue $-\cdot$), robust optimal controller K_4^{RP} (cyan $--$) and robust inferential controller K_9^{RP} (magenta $-$).

Chapter 8

Conclusions and recommendations

8.1 Conclusions

Control of high-precision positioning systems, requires advanced motion control techniques, to satisfy the demands on speed and accuracy. The trend in design of these systems is towards lightweight structures, capable of high accelerations. The mass is reduced at the expense of stiffness of the structure, and consequently flexible dynamics become more prominent in the system behavior. This rises the question how this influences the performance of the system, and how control is able to deal with it. This question is answered, by studying a representative scenario on a flexible beam. In Section 1.4, the research questions for this theses are presented, and the conclusions will be discussed in the same order.

1. Structures with flexible dynamics have internal degrees of freedom, and rigid body dynamics are not sufficient to describe the behavior of such structures. Optimal control of the measured variables is possible, but excitation of the flexible dynamics causes vibrations in the structure and deteriorates the performance outside the sensor locations.

2. The inferential control configuration is able to deal with flexible systems in which the performance variables are not measured.

   (a) The performance problem that is caused by excitation of the flexible dynamics of the system, is not part of the standard optimal control problem formulation, which is based on rigid body behavior of the plant and considers the measured variables to be the performance variables. Consequently, the resulting controller designs have low performance on systems with internal dynamics.

   (b) The inferential control configuration includes the performance variables in the control problem, and thereby is able to deal with systems with flexible dynamics. It is possible to synthesize $\mathcal{H}_\infty$ optimal controllers for the inferential control configuration, using well-known reliable algorithms.

   (c) In the inferential control configuration, the performance variables are inferred from the measured output of the system. This requires accurate knowledge of the system dynamics, and thus relies on the availability of high quality models.

3. An accurate model, suitable for the inferential control problem, can be obtained by using the control-relevant identification procedure. This has been confirmed by experiments on the flexible beam setup.

(a) A control-relevant identification criterion for the inferential control structure is obtained. Minimization of the identification criterion requires data from the measured variables, as well as the performance variables. Therefore, in the identification experiment both need to be measured.

(b) A numerically reliable well-conditioned algorithm, that minimizes the control-relevant identification criterion, is available in [34].

(c) During the identification experiments it is sufficient to use a controller that is designed by the rules of thumb commonly used by control engineers and it is not necessary to design an initial inferential controller for the experiment.

(d) The plant dynamics that are the most relevant for control, are closely approximated by the identified model. This is confirmed by experiments, which show very similar closed-loop responses compared to the simulations with the fitted model, indicating that the same dynamics dominate the response.

(e) The finite element model of the flexible beam gives a good indication of the performance that can be achieved with optimal control. The identification procedure and controller synthesis algorithm use the same weighting filters, and therefore the finite element model is useful for the selection of weighting filters for the identification procedure.

4. The model validation procedure for robust control, can be used to address systematic modeling errors, and to obtain a model set that is suitable for robust controller design. This is confirmed by experiments on the flexible beam setup.

   (a) The favorable properties of the dual-Youla parametrization are extended to the inferential control structure. It is guaranteed that all plants that are internally stabilized by the experimental controller, are included in the model set, i.e., the dynamics of the true system are included in the model set.

   (b) For the flexible beam, the model uncertainty in the inferential control structure consists of two independent 1×1 blocks. This is advantageous, since it implies that the bounds on both uncertainty blocks can be determined separately.

   (c) The uncertainty bounds on the experimental setup, obtained with the model validation procedure, are close to the nominal model and experimental data, and result in a model set that is not overly large.

5. Optimal controllers have been designed and implemented on the flexible beam, with a significant increased performance as a result.

   (a) The nominal performance of the optimal inferential controller has improved by a factor 4.16, compared to the standard optimal controller. This is a large improvement, that is confirmed by experiments on the experimental setup.

   (b) There is a factor 4.55 improvement in the worst case performance for the robust inferential controller, compared to the standard robust controller. Experiments on the flexible beam setup indicate a similar improvement in performance.

   (c) The controller that is optimized for performance on the nominal model, will not result in optimal performance for the true system. This is confirmed by the worst case performance criterion for this controller, which is a factor 9.04 larger than for the nominal model.

   (d) The worst case performance of the robust inferential controller is 6.48 times improved, compared to the nominal controller. Therefore, the robust inferential controller has the best guaranteed performance level for implementation on the plant.

With the answer to all research questions, the main question of this thesis, "*What is the influence of flexible dynamics in next-generation lightweight positioning systems, when the measured variables are not the performance variables, and how can motion control be used to deal with flexible dynamics?*", is answered.

> *Inferential control can significantly improve the performance for systems with flexible dynamics. A proof of concept has been delivered, by validating the approach on a prototype high performance positioning system with flexible dynamics.*

8.2 Recommendations

From the conclusions in the previous section, a few recommendations for future research are formulated.

- Apply inferential control to flexible structures with more complex geometries.

A proof of concept has been given for a flexible beam. This is a simplified form of a high-performance positioning device, of which the dynamics have been studied extensively in literature. This makes it relatively straightforward for a mechanical engineer, to interpret the behavior of the system and the obtained results. There are no limitations in the used theory that restrict application to flexible structures for which analytical modeling is cumbersome, and it is valuable to confirm this with experiments.

- Verify the obtained results on a MIMO system with flexible dynamics.

The theory has been applied to a SISO system, which has one measured variable, and one performance variable. There are no restrictions on the number of inputs and outputs for the used methods, and it would be interesting to investigate the results on a system with multiple feedback-loops, or multiple performance variables.

- Investigate the relations between inferential control and over-actuation, see e.g. [43].

In the inferential controller design as shown in this thesis, flexible dynamics play a prominent role. Over-actuation is another subject that is concerned with the internal dynamics of motion systems, and it is to be expected that these fields of research are related. It would be interesting to study these relations, and explore the possibilities of inferential control on over-actuated systems.

- Design an algorithm that computes a tight parametric overbound on the model uncertainty.

Currently, no algorithm is available and a overbound has to be designed manually. This design is cumbersome and time-consuming, so an algorithm with low computational cost, is a desirable improvement.

- Investigate the influence of external disturbances on inferential control.

In standard feedback control, all external disturbances enter the feedback loop directly, and can therefore be attenuated by the controller. For systems with flexible dynamics, it is also possible that a disturbance enters the system at a location that is noncollocated with the measured output. It would be interesting to study the consequences of such disturbances. See [12, 22] for initial results in this direction.

Appendix A

Suboptimal $\mathcal{H}_\infty$ controller synthesis

The suboptimal $\mathcal{H}_\infty$ problem is to find a stabilizing controller K for generalized plant P, such that

$$\|\mathcal{F}_l(P,K)\|_\infty \leq \gamma, \tag{A.1}$$

where $\gamma > \gamma_{\min}$, i.e. γ is larger than the optimal value $\gamma_{\min}$. In order to solve this problem, the approach in [29, Ch. 3] is followed. First, it gives some definitions and assumptions. Then, a set of controllers satisfying (A.1) is parametrized, according to Theorem A.1. Finally, a close to optimal controller is obtained using a bisection algorithm. The method in [29, Ch. 3] is as follows.

Consider the standard plant $P \in \mathbb{R}$ with dimensions $(p_1 + p_2) \times (m_1 + m_2)$, given by

$$P = \left[\begin{array}{c|cc} P_{11} & P_{12} \\ \hline P_{21} & P_{22} \end{array}\right] \stackrel{s}{=} \left[\begin{array}{c|cc} A & B_1 & B_2 \\ \hline C_1 & D_{11} & D_{12} \\ C_2 & D_{21} & D_{22} \end{array}\right], \tag{A.2}$$

that satisfies the following assumptions.

Assumptions

1. (A, B_2, C_2) is stabilizable and detectable,
2. $\operatorname{rank}(D_{12}) = m_2$ and $\operatorname{rank}(D_{21}) = p_2$,
3. $D_{12} = \begin{bmatrix} 0 \\ I_{m_2} \end{bmatrix}$, $D_{21} = \begin{bmatrix} 0 & I_{p_2} \end{bmatrix}$, and $D_{11} = \begin{bmatrix} D_{1111} & D_{1112} \\ D_{1121} & D_{1122} \end{bmatrix}$ is dimensioned accordingly,
4. $D_{22} = 0$,
5. $\operatorname{rank}\begin{bmatrix} A - j\omega I & B_2 \\ C_1 & D_{12} \end{bmatrix} = n + m_2$ for all $\omega \in \mathbb{R}$,
6. $\operatorname{rank}\begin{bmatrix} A - j\omega I & B_1 \\ C_2 & D_{21} \end{bmatrix} = n + p_2$ for all $\omega \in \mathbb{R}$.

Then define

$$R = D_{1\bullet}^* D_{1\bullet} - \begin{bmatrix} \gamma^2 I_{m_1} & 0 \\ 0 & 0 \end{bmatrix} \text{ where } D_{1\bullet} = \begin{bmatrix} D_{11} & D_{12} \end{bmatrix}, \tag{A.3}$$

$$\tilde{R} = D_{\bullet 1} D_{\bullet 1}^1 - \begin{bmatrix} \gamma^2 I_{p_1} & 0 \\ 0 & 0 \end{bmatrix} \text{ where } D_{\bullet 1} = \begin{bmatrix} D_{11} \\ D_{21} \end{bmatrix}. \tag{A.4}$$

The stabilizing solution to an algebraic Riccati equation (ARE) is denoted via its associated Hamiltonian matrix as

$$X = \mathrm{Ric} \begin{Bmatrix} A & -P \\ -Q & -A^* \end{Bmatrix}, \; P = P^*, \; Q = Q*, \tag{A.5}$$

where this implies $X = X^*$ and

$$XA + A^*X - XPX + Q = 0, \quad \mathrm{Re}\left[\lambda_i \left(A - PX\right)\right] < 0. \tag{A.6}$$

Then, define X_∞, Y_∞ as ARE solutions (assuming they exist) by

$$X_\infty = \mathrm{Ric}\left\{ \begin{bmatrix} A & 0 \\ -C_1^* C_1 & -A^* \end{bmatrix} - \begin{bmatrix} B \\ -C_1^* D_{1\bullet} \end{bmatrix} R^{-1} \begin{bmatrix} D_{1\bullet}^* C_1 & B^* \end{bmatrix} \right\}, \tag{A.7}$$

$$Y_\infty = \mathrm{Ric}\left\{ \begin{bmatrix} A^* & 0 \\ -B_1 B_1^* & -A \end{bmatrix} - \begin{bmatrix} C^* \\ -B_1 D_{\bullet 1}^* \end{bmatrix} \tilde{R}^{-1} \begin{bmatrix} D_{\bullet 1} B_1^* & C \end{bmatrix} \right\}, \tag{A.8}$$

and define

$$F_I = \begin{bmatrix} F_{11} \\ F_{12} \\ F_2 \end{bmatrix} \tag{A.9}$$

$$= -R^{-1}\left[D_{1\bullet}^* C_1 + B^* X_\infty\right], \tag{A.10}$$

$$H_I = \begin{bmatrix} H_{11} & H_{12} & H_2 \end{bmatrix} \tag{A.11}$$

$$= -\left[B_1 D_{\bullet 1}^* + Y_\infty C^*\right] \tilde{R}^{-1}. \tag{A.12}$$

All stabilizing controllers achieving (A.1) are given by the following theorem.

Theorem A.1 (Stabilizing controllers [29, Thm. 3.14]). *For the standard plant* (A.2)*, that satisfies the assumptions 1-6,*

1. *there exists an internally stabilizing controller K such that* (A.1)*, if and only if:*
   (a) $\gamma > \gamma_l$, $\gamma_l = \max\left(\bar{\sigma}\begin{bmatrix} D_{1111} & D_{1112} \end{bmatrix}, \bar{\sigma}\begin{bmatrix} D_{1111}^* & D_{1121}^* \end{bmatrix}\right)$, *and*
   (b) *there exist $X_\infty \geq 0$ and $Y_\infty \geq 0$, such that $\rho\left(X_\infty Y_\infty\right) < \gamma^2$.*
2. *If above conditions are satisfied, all rational and internal stabilizing controllers such that* (A.1) *is satisfied, are given by $K = \mathcal{F}_l\left(K_a, \Phi\right)$ for any $\Phi \in \mathcal{RH}_\infty^{m_2 \times p_2}$ with $\|\Phi\|_\infty \leq \gamma$, where*

$$K_a = \left[\begin{array}{c|c} K_{11} & K_{12} \\ \hline K_{21} & K_{22} \end{array}\right] \stackrel{s}{=} \left[\begin{array}{c|cc} \hat{A} & \hat{B}_1 & \hat{B}_2 \\ \hline \hat{C}_1 & \hat{D}_{11} & \hat{D}_{12} \\ \hat{C}_2 & \hat{D}_{21} & 0 \end{array}\right], \tag{A.13}$$

$$\hat{D}_{11} = -D_{1121} D_{1111}^* \left(\gamma^2 I - D_{1111} D_{1111}^*\right)^{-1} D_{1112} - D_{1122} \tag{A.14}$$

and $\hat{D}_{12} \in \mathbb{R}^{m_2 \times m_2}$ *and* $\hat{D}_{21} \in \mathbb{R}^{p_2 \times p_2}$ *satisfy*

$$\hat{D}_{12}\hat{D}_{12}^* = I - D_{1121}\left(\gamma^2 I - D_{1111}D_{1111}^*\right)^{-1} D_{1121}^*, \tag{A.15}$$

$$\hat{D}_{21}^*\hat{D}_{21} = I - D_{1112}^*\left(\gamma^2 I - D_{1111}D_{1111}^*\right)^{-1} D_{1112}, \tag{A.16}$$

and

$$\hat{B}_2 = (B_2 + H_{12})\,\hat{D}_{12}, \tag{A.17}$$

$$\hat{C}_2 = -\hat{D}_{21}\,(C_2 + F_{12}Z), \tag{A.18}$$

$$\hat{B}_1 = -H_2 + \hat{B}_2\hat{D}_{12}^{-1}\hat{D}_{11}, \tag{A.19}$$

$$\hat{C}_1 = F_2 Z + \hat{D}_{11}\hat{D}_{21}^{-1}\hat{C}_2, \tag{A.20}$$

$$\hat{A} = A + H_I C + \hat{B}_2\hat{D}_{12}^{-1}\hat{C}_1, \tag{A.21}$$

where

$$Z = \left(I - \gamma^{-2}Y_\infty X_\infty\right)^{-1}. \tag{A.22}$$

A suboptimal controller close to the optimal controller can then be found using the following bisection algorithm.

1. Select $\gamma > \gamma_l$, see item 1.a in Theorem A.1, and a tolerance μ.
2. Check whether the condition in item 1.b of Theorem A.1 is satisfied:

   Yes: Let $\gamma_u := \gamma$ and $\gamma := \frac{\gamma_l + \gamma_u}{2}$. Repeat step 2 if $\gamma_u - \gamma > \mu$.

   No: Let $\gamma_l := \gamma$ and $\gamma := \frac{\gamma_l + \gamma_u}{2}$. Repeat step 2.
3. When the bisection algorithm has reached the tolerance μ, use γ_u to compute K_a. Then, a suboptimal controller is given by $K = \mathcal{F}_l(K_a, \Phi)$.

Remarks

1. An exact solution exists if P_{12} and P_{21} are square.
2. An exact solution also exists for the coprime factor robust stabilization problem, as in [29, Ch. 4]. For a plant set G_Δ with $\left\{\tilde{\hat{N}}, \tilde{\hat{D}}\right\}$ the normalized LCF of nominal plant $\hat{G}$, given by

$$G_\Delta = \left(\tilde{\hat{D}} + \Delta_D\right)^{-1}\left(\tilde{\hat{N}} + \Delta_N\right), \tag{A.23}$$

the optimal controller is obtained by computing $K = \mathcal{F}_l(K_a, 0)$ using

$$\gamma_{\min} = \inf_{K \text{ stabilizing}} \left\| \begin{bmatrix} K \\ I \end{bmatrix} (I - GK)^{-1}\tilde{\hat{M}}^{-1} \right\|_\infty = \left\{1 - \left\| \begin{bmatrix} \tilde{\hat{N}} & \tilde{\hat{D}} \end{bmatrix} \right\|_H^2 \right\}^{-1/2}. \tag{A.24}$$

Appendix B

Graphical representation model sets

This appendix discusses the graphical representation of model sets in Bode diagrams. In Section B.1 is discussed how bounds for magnitude and phase of a SISO model set are derived. In Section B.2 is discussed how bounds on the magnitude and phase can be determined when two sets are multiplied. Finally, in Section B.3 is discussed how a model set can be inverted.

B.1 Representation of the model set

Consider a model set

$$N_\Delta = \hat{N}(\omega) + \Delta_N(\omega), \tag{B.1}$$

with $\hat{N}(\omega)$ the nominal model and $\Delta_N(\omega)$ the model uncertainty, such that

$$\|\Delta_N(\omega)\|_\infty \leq \gamma_N(\omega). \tag{B.2}$$

At any given frequency this model set forms a disc in the complex plane, with center $\hat{N}$ and radius γ_N, as shown in Figure B.1.

Using the exponential form of complex numbers,

$$N = r_N e^{j\phi_N}, \tag{B.3}$$

where r_N and ϕ_N are the magnitude and phase of any point N on the disc, respectively. Observe from Figure B.2a that the minimum and maximum magnitude in the model set are given by

$$r_{N_\Delta}^{\max} = r_{\hat{N}} + \gamma_N \tag{B.4}$$

$$r_{N_\Delta}^{\min} = r_{\hat{N}} - \gamma_N. \tag{B.5}$$

Derivation of the minimum and maximum phase of the model set requires some trigonometry as shown in Figure B.2b. In this figure the two tangents of the disc that go through the origin of the complex plane, are drawn. The points where the tangents touch the disc, are the points with minimum and maximum phase. Using the two right triangles, created by connecting these points with the origin and the center of the disc, the minimum and maximum phase are given by

$$\phi_{N_\Delta}^{\max} = \phi_{\hat{N}} + \arcsin(\gamma_N / r_{\hat{N}}) \tag{B.6}$$

$$\phi_{N_\Delta}^{\min} = \phi_{\hat{N}} - \arcsin(\gamma_N / r_{\hat{N}}). \tag{B.7}$$

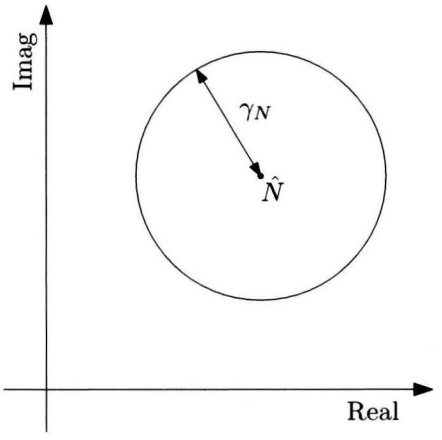

Figure B.1: Model set as a circle in the complex plane.

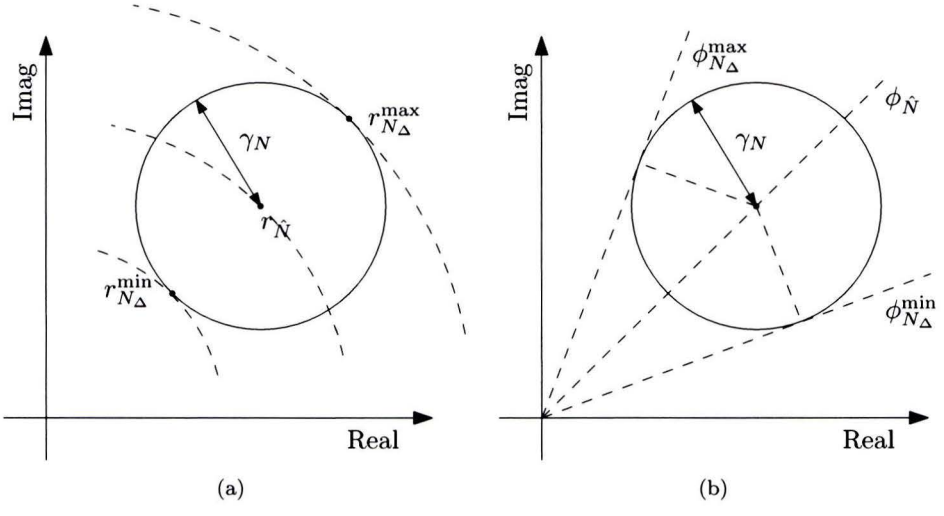

Figure B.2: Minimum and maximum magnitude (a) and phase (b) of the circle.

Note that if the disc covers the origin, the minimum magnitude is $r_{N_\Delta}^{\min} = 0$, and there are no bounds on the phase.

B.2 Multiplication of model sets

Consider two model sets L_Δ and M_Δ of the same form as in (B.1), that form the set N_Δ upon multiplication,

$$N_\Delta = L_\Delta M_\Delta. \tag{B.8}$$

Using the exponential form (B.3) for L and M, a point N in the model set is given by

$$\begin{aligned} N &= LM && \text{(B.9)} \\ &\quad r_L e^{j\phi_L} r_M e^{j\phi_M} && \text{(B.10)} \\ &= r_L r_M e^{j(\phi_L+\phi_M)}. && \text{(B.11)} \end{aligned}$$

By taking

$$r_N = r_L r_M, \tag{B.12}$$
$$\phi_N = \phi_L + \phi_M, \tag{B.13}$$

N also is in the exponential form, i.e.,

$$N = r_N e^{j\phi_N}. \tag{B.14}$$

Then, the minimum and maximum magnitude of N_Δ are determined as follows. The domains r_{L_Δ} and r_{M_Δ} are given by

$$r_L \in r_{L_\Delta} = \left[r_{L_\Delta}^{\min}, r_{L_\Delta}^{\max}\right], \tag{B.15}$$
$$r_M \in r_{M_\Delta} = \left[r_{M_\Delta}^{\min}, r_{M_\Delta}^{\max}\right], \tag{B.16}$$

and a function f that maps $r_{L_\Delta} \times r_{M_\Delta}$ to r_{N_Δ}, i.e., $f : r_{L_\Delta} \times r_{M_\Delta} \rightarrow r_{N_\Delta}$, is defined as

$$f(r_L, r_M) = r_L r_M, \tag{B.17}$$

i.e., $r_N = f(r_L, r_M)$, see (B.12). The range of f is then given by

$$\left[r_{L_\Delta}^{\min} r_{M_\Delta}^{\min}, r_{L_\Delta}^{\max} r_{M_\Delta}^{\max}\right], \tag{B.18}$$

and therefore the minimum magnitude of N_Δ is given by

$$r_{N_\Delta}^{\min} = r_{L_\Delta}^{\min} r_{M_\Delta}^{\min}, \tag{B.19}$$

and the maximum magnitude is

$$r_{N_\Delta}^{\max} = r_{L_\Delta}^{\max} r_{M_\Delta}^{\max}. \tag{B.20}$$

In similar fashion the range of the phase is determined. The domains ϕ_{L_Δ} and ϕ_{M_Δ} are given by

$$\phi_L \in \phi_{L_\Delta} = \left[\phi_{L_\Delta}^{\min}, \phi_{L_\Delta}^{\max}\right], \tag{B.21}$$
$$\phi_M \in \phi_{M_\Delta} = \left[\phi_{M_\Delta}^{\min}, \phi_{M_\Delta}^{\max}\right], \tag{B.22}$$

and a function $g : \phi_{L_\Delta} \times \phi_{M_\Delta} \rightarrow \phi_{N_\Delta}$, is defined as

$$g(\phi_{L_\Delta}, \phi_{M_\Delta}) = \phi_{L_\Delta} + \phi_{M_\Delta}. \tag{B.23}$$

The range of g is

$$\phi_{N_\Delta} = \left[\phi_{L_\Delta}^{\min} + \phi_{M_\Delta}^{\min}, \phi_{L_\Delta}^{\max} + \phi_{M_\Delta}^{\max}\right], \tag{B.24}$$

and consequently the minimum and maximum phase of N_Δ are

$$\phi_{N_\Delta}^{\min} = \phi_{L_\Delta}^{\min} + \phi_{M_\Delta}^{\min}, \tag{B.25}$$
$$\phi_{N_\Delta}^{\max} = \phi_{L_\Delta}^{\max} + \phi_{M_\Delta}^{\max}. \tag{B.26}$$

B.3 Inversion of a model set

Consider the model set D_Δ of the same form as (B.1), in the exponential form (B.3). Then,

$$N = \frac{1}{D} \tag{B.27}$$
$$= \frac{1}{r_D e^{j\phi_D}} \tag{B.28}$$
$$= \frac{1}{r_D} e^{-j\phi_D}. \tag{B.29}$$

By defining

$$r_N = \frac{1}{r_D}, \tag{B.30}$$

$$\phi_N = -\phi_D, \tag{B.31}$$

N is again in exponential form. The minimum and maximum magnitude and phase of N_Δ are then determined again in similar fashion. The domains for the magnitude and phase of D_Δ are given by

$$r_D \in r_{D_\Delta} = \left[r_{D_\Delta}^{\min}, r_{D_\Delta}^{\max}\right], \tag{B.32}$$

$$\phi_D \in \phi_{D_\Delta} = \left[\phi_{D_\Delta}^{\min}, \phi_{D_\Delta}^{\max}\right], \tag{B.33}$$

and functions $f : r_{D_\Delta} \to r_{N_\Delta}$, $g : \phi_{D_\Delta} \to \phi_{N_\Delta}$ are defined by

$$f(r_D) = \frac{1}{r_D}, \tag{B.34}$$

$$g(\phi_D) = -\phi_D, \tag{B.35}$$

i.e., $r_N = f(r_D)$ and $\phi_N = g(\phi_D)$. The ranges of f and g are

$$\mathrm{ran}f = \left[1/r_{D_\Delta}^{\max}, 1/r_{D_\Delta}^{\min}\right], \tag{B.36}$$

$$\mathrm{ran}g = \left[-\phi_{D_\Delta}^{\max}, -\phi_{D_\Delta}^{\min}\right], \tag{B.37}$$

and consequently the bounds on the magnitude of N_Δ are known. Note that in case D_Δ covers the origin, $r_{D_\Delta}^{\min} = 0$ and the range of f is $\left[1/r_{D_\Delta}^{\max}, \infty\right)$, i.e., the magnitude only has a lower bound. This is explained in the following example.

Example B.1. Given is a model set $D_\Delta = \hat{D} + \Delta_D$, with $\hat{D} = -1 + j$ and $\|\Delta_D\|_\infty \leq \gamma_D$, and $N_\Delta = 1/D_\Delta$. First, consider the case that $\gamma_D = 1$ such that the model set does not cover the origin. This is shown in Figure B.3. Observe that the edge of the disc remains a circle when it is inverted, although the interior of the disc is deformed and $\hat{N}$ is not the center of this circle.

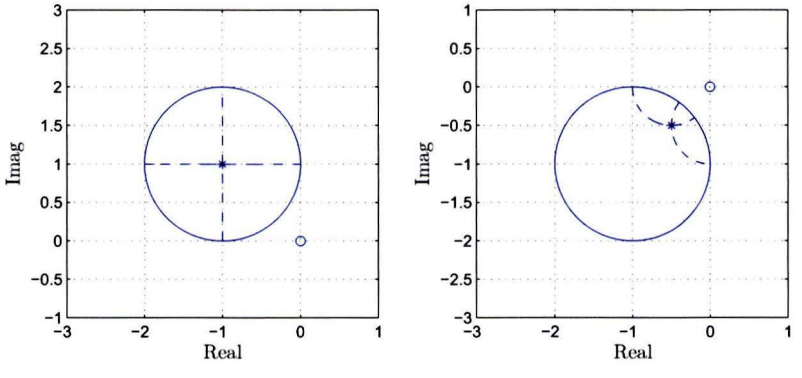

Figure B.3: On the left, the edge of the model set D_Δ $(-)$ is shown, with nominal model $\hat{D}$ $(*)$, other interior points of the model set $(--)$, and the origin $(\circ)$. On the right, the same is shown for $N_\Delta = 1/D_\Delta$.

Now, consider the case that $\gamma_D = 2$ such that the origin is covered by the disc formed by model set D_Δ, as shown in Figure B.4. Observe that the edge of the disc remains a circle when it is inverted, but now the interior of the disc is mapped to the exterior, and hence a minimum for the magnitude can be found.

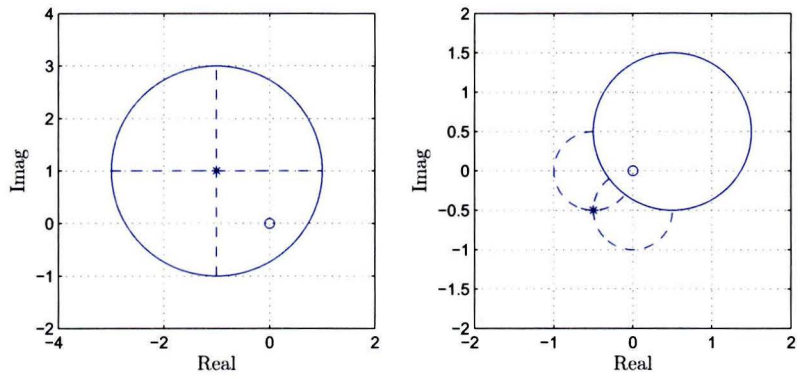

Figure B.4: On the left, the edge of the model set D_Δ $(-)$ is shown, with nominal model $\hat{D}$ $(*)$, other interior points of the model set $(--)$, and the origin $(\circ)$. On the right, the same is shown for $N_\Delta = 1/D_\Delta$.

Remark

Bounds on the magnitude can also be derived as in [20], where a Möbius transformation is used. The Möbius transformation is a more general method, that maps one complex space to another, which is frequently encountered in complex analysis. The method in [20] confirms the results that have been found for the bounds on the magnitude, the uncertainty bounds on the phase are not considered.

Bibliography

[1] Gary J. Balas and John C. Doyle. Control of lightly damped, flexible modes in the controller crossover region. *Journal of Guidance, Control and Dynamics*, 17:370–377, 1994.

[2] Gary J. Balas and John C. Doyle. Robustness and performance trade-offs in control design for flexible structures. *IEEE Transactions on Control Systems Technology*, 2:352–361, 1994.

[3] P.M.T. Broersen. A comparison of transfer function estimators. *IEEE Transactions Intrumentation and Measurement*, 44(3):657–661, 1995.

[4] C. Brosilow and M. Tong. The structure and dynamics of inferential control systems. *AIChE Journal*, 24:492, 1978.

[5] R.A. de Callafon and P.M.J. van den Hof. Suboptimal feedback control by a scheme of iterative identification and control design. *Mathematical Modelling of Systems*, 3(1):77–101, 1997.

[6] Robert D. Cook, David S. Malkus, and Michael E. Plesha. *Concepts and applications of finite element analysis.* John Wiley, New York, NY, USA, third edition, 1989.

[7] James F. Doyle. *Wave propagation in structures.* Mechanical engineering series. Springer, New York, NY, USA, 1997.

[8] J.C. Doyle. Synthesis of robust controllers and filters. In *IEEE Conference on Decision and Control*, pages 109–114, San Antonio, TX, USA, 1983.

[9] J.C. Doyle, Bruce Francis, and Allen Tannenbaum. *Feedback control theory.* Macmillan Publishing Company, New York, NY, USA, 1992.

[10] John C. Doyle, Keith Glover, Pramod P. Khargonekar, and Bruce A. Francis. State-space solutions to standard $\mathcal{H}_2$ and $\mathcal{H}_\infty$ control problems. *IEEE Transactions on Automatic Control*, 34:831–847, 1989.

[11] M.K.H. Fan and A.L. Tits. A measure of worst-case $\mathcal{H}_\infty$ performance and of largest acceptable uncertainty. *Systems and Control letters*, 18(6):409–412, 1992.

[12] Jim S. Freudenberg, C.V. Hollot, Richard H. Middleton, and Toochinda Varodom. Fundamental desing limitations of the general control configuration. *IEEE Transactions on Automatic Control*, 48(8):1355–1370, August 2003.

[13] W. Gawronski. A balanced LQG compensator for flexible structures. *Automatica*, 30:1555–1564, 1994.

[14] Wodek K. Gawronski. *Advanced structural dynamics and active control of structures.* Mechanical engineering series. Springer, New York, NY, USA, 2004.

[15] M. Gevers. *Essays on control: Perspectives in the theory and its applications*, chapter 5 "Towards a joint design of identification and control?", pages 111–151. Birkhäuser, Boston, MA, USA, 1993.

[16] K. Glover and J.C. Doyle. State-space formulae for all stabilizing controllers that satisfy an $\mathcal{H}_\infty$-norm bound and relations to risk sensitivity. *Systems and Control Letters*, 11:167–172, 1988.

[17] E. Grassens. Literatuurverslag. Literature study, TU/e, 2009.

[18] P. Guillaume, I Kollár, and R. Pintelon. Statistical analysis of nonparametric transfer function estimates. *IEEE Transactions on Intrumentation and Measurement*, IM-45(2):594–600, 1996.

[19] F.B.J.W.M Hendriks. Achieving beyond flexible dynamics control of a prototype lightweight positioning system: A theory-driven experimental approach. Master's thesis, Eindhoven University of Technology, Eindhoven, Netherlands, 2009.

[20] Robbert van Herpen. Experimental modeling and validation for robust motion control of next-generation wafer stages. Master's thesis, Eindhoven University of Technology, Eindhoven, Netherlands, 2009.

[21] P.M.J. van den Hof and A.J. den Dekker. *Signal Analysis and Estimation.* Delft Center for Systems and Control, Delft, Netherlands, 2001.

[22] Jeongho Hong and Dennis S. Bernstein. Bode integral constraints, colocation, and spillover in active noise and vibration control. *IEEE Transactions on Control Systems Technology*, 6:111–120, 1998.

[23] D.J. Hoyle, R.A. Hyde, and D.J.N. Limebeer. An $\mathcal{H}_\infty$ approach to two degree of freedom design. In *Proceedings of the 30th Conference on Decisions and Control*, pages 1581–1585, Brighton, UK, 1991.

[24] V. Kariwala and S. Skogestad. Limits of disturbance rejection for indirect control. In *Proceedings of the 44th Conference on Decision and Control*, pages 3620–3625, Seville, Spain, 2005.

[25] F.M. Klomp. Implementing a hard real-time data aquisition and control system on Linux RTAI-LXRT. Traineeship report DCT 2005.72, Eindhoven Technical University, Eindhoven, Netherlands, 2005.

[26] R. Lind, G. Balas, and A. Packard. Evaluating *d-k* iteration for control design. In *Proceedings of the American Control Conference*, pages 2792–2797, Baltimore, MD, USA, 1994.

[27] Lennart Ljung. *System identification: Theory for the user.* System Sciences Series. Prentice Hall, Upper Saddle River, NJ, USA, second edition, 1999.

[28] T. Marlin. *Process Control.* McGraw-Hill chemical engineering series. McGraw-Hill, London, UK, 1995.

[29] D.C. McFarlane and K. Glover. *Robust controller design using normalized coprime factor plant descriptions.* Number 138 in Lecture notes in control and information sciences. Springer-Verlag, Berlin, Germany, 1990.

[30] Leonard Meirovitch. *Analytical methods in vibrations.* The MacMillan Company, New York, New York, NY, USA, 1967.

[31] D.K. Miu. Physical interpretation of transfer function zeros for simple control systems with mechanical flexibilites. *Journal of dynamic systems, measurement, and control*, 113:419–424, 1991.

[32] P.M. Mäkilä, J.R. Partington, and T.K. Gustafsson. Worst-case control-relevant identification. *Automatica*, 31(12):1799–1819, 1995.

[33] Tom Oomen and Okko Bosgra. Estimating disturbances and model uncertainty in model validation for robust control. In *Proceedings of the 47th Conference on Decision and Control*, pages 5513–5518, Cancún, Mexico, 2008.

[34] Tom Oomen and Okko Bosgra. Robust-control-relevant coprime factor identification: a numerically reliable frequency domain approach. In *Proceedings of the 2008 American control conference*, pages 625–631, Seattle, WA, USA, June 2008.

[35] Tom Oomen and Okko Bosgra. Well-posed model quality estimation by design of validation experiments. In *Proceedings of the 15th IFAC Symposium on System Identification*, pages 1199–1204, Saint-Malo, France, 2009.

[36] Tom Oomen, Okko Bosgra, and Marc van de Wal. Identification for robust inferential control. In *Proceedings of the 48th Conference on Decision and Control*, pages 2581–2586, Shanghai, China, 2009.

[37] A. Packard and J. Doyle. The complex structured singular value. *Automatica*, 29:71–109, 1993.

[38] F. Paganini and J. Doyle. Analysis of implicitly defined systems. In *Proceedings of the 33rd conference on decision and control*, pages 3673–3678, Lake Buena Vista, FL, USA, 1994.

[39] J.R. Parrish and C.B. Brosilow. Inferential control applications. *Automatica*, 21(5):527–538, 1985.

[40] R. Pintelon and J. Schoukens. *System identification: a frequency domain approach.* IEEE Press, New York, NY, USA, 2001.

[41] K. Poolla, P. Khargonekar, A. Tikku, J. Krause, and K. Nagpal. A time-domain approach to model validation. *IEEE Transactions on Automatic Control*, 39(5):951–959, 1992.

[42] C.K. Sanathanan and J. Koerner. Transfer function synthesis as a ratio of two complex polynomials. *IEEE Transactions on Automatic Control*, 8:56–58, 1963.

[43] M.G.E. Schneiders, M.J.G. van de Molengraft, and M. Steinbuch. Benefits of over-actuation in motion systems. In *American Control Conference*, pages 505–510, Boston, MA, USA, 2004.

[44] R.J.P. Schrama. Accurate identification for control: The necessity of an iterative scheme. *IEEE Transactions on Automatic Control*, 37(7):991–994, 1992.

[45] Sigurd Skogestad and Ian Postlethwaite. *Multivariable feedback control.* Wiley, West Susex, UK, second edition, 2005.

[46] R.S. Smith and J.C. Doyle. Model validation: A connection between robust control and identification. *IEEE Transactions on Automatic Control*, 37(7):942–952, 1992.

[47] G. Stephanopoulos. *Chemical process control.* Prentice-Hall international series in the physical and chemical engineering sciences. Prentice-Hall, Englewood Cliffs, NJ, USA, 1984.

[48] T. Tay, I. Mareels, and J. B. Moore. *High performance control.* Birkhäuser, Cambridge, MA, USA, 1998.

[49] J.W. van Wingerden. Control of flexible motion systems using piezoelectric over-actuation. CTB 534-04-1610, Delft University of Technology, Delft, The Netherlands, December 2004.

[50] Kemin Zhou, John C. Doyle, and Keith Glover. *Robust and optimal control.* Prentice Hall, Englewood cliffs, NJ, USA, 1996.